

Long-lived Light Mediators in a Higgs Portal Model at the FCC-ee

Biplob Bhattacharjee¹, Camellia Bose¹, Herbi K. Dreiner², Nivedita Ghosh³, Shigeki Matsumoto³, Rhitaja Sengupta²

¹ *Centre for High Energy Physics, Indian Institute of Science, Bengaluru 560012, India*

² *Bethe Center for Theoretical Physics and Physikalisches Institut der Universität Bonn, Nußallee 12, Bonn 53115, Germany*

³ *Kavli IPMU (WPI), UTIAS, University of Tokyo, Kashiwa, Chiba, 277-8583, Japan*

E-mail: biplob@iisc.ac.in, camelliabose@iisc.ac.in,
dreiner@uni-bonn.de, nivedita.ghosh@ipmu.jp,
shigeki.matsumoto@ipmu.jp, rsengupt@uni-bonn.de

ABSTRACT: In the search for beyond the Standard Model (SM) physics, long-lived particles (LLPs) have emerged as potential candidates and are being explored in various ongoing experiments. Future lepton colliders, such as the FCC-ee, shall provide an excellent opportunity to probe LLPs, owing to their clean environment and improved particle identification. This study investigates the potential of the proposed **I**nnovative **D**etector for an **E**lectron-**P**ositron **A**ccelerator (IDEA) detector at FCC-ee in the detection of LLPs produced from B -meson and Higgs boson decays. We explore benchmark scenarios for different final states resulting from LLP decays, including a detailed analysis of the SM long-lived hadronic background. Additionally, we propose dedicated LLP detectors with different configurations, dimensions, and locations with respect to the IDEA detector. DELIGHT B, originally proposed as a dedicated LLP detector for the FCC-hh, stands out as the detector with the maximum efficiency for detecting LLPs produced at FCC-ee. We find that cylindrical detector configurations, if feasible to construct around the IDEA detector, would also enhance sensitivity for LLPs mostly decaying outside it.

Contents

1	Introduction	1
2	Scalar LLPs in the Higgs portal	4
3	Current status and benchmark choice	7
4	Role of e^+e^- Colliders in exploring the Benchmarks	12
4.1	The IDEA Detector	13
4.2	Backgrounds	16
4.3	Analysis Strategy	17
4.4	LLPs with Negligible Trilinear Coupling	20
4.4.1	Analysis in the Di-muon Final State	20
4.4.2	Analysis in the Di-pion and Di-kaon Final States	24
4.4.3	Analysis in the $c\bar{c}$ Final State	30
4.4.4	Production via $Z \rightarrow Z^*\phi$	32
4.5	LLPs with large Trilinear Coupling	33
4.5.1	Analysis in the Di-pion and Di-kaon Final States	33
4.5.2	Analysis in the $c\bar{c}$ and $b\bar{b}$ Final States	36
5	Dedicated Detectors at e^-e^+ Colliders	40
6	Summary and Conclusions	47
A	Efficiency Maps of Model-independent Analyses	50
B	Configurations of dedicated detectors	52
C	Efficiency maps of dedicated detectors in the case of $B \rightarrow K\phi$	57
D	Efficiency maps of dedicated detectors in the case of $h \rightarrow \phi\phi$	65

1 Introduction

Our quest to find any hint of physics beyond the Standard model of particle physics (SM) is fueled by open questions, like what is a feasible candidate for dark matter, how to generate the observed small neutrino masses, and why is there a baryon asymmetry in the Universe? A decade after the Higgs boson discovery at the LHC,

we are at a juncture where the lack of significant observation of Beyond the Standard Model (BSM) physics is now demanding a much-needed paradigm shift in our search strategies. A growing interest is to expand the parameter space of BSM physics searches beyond the conventional regime by letting go of some of our fundamental assumptions. One such assumption is the prompt decay of a hypothetical newly produced particle in a collider experiment. Even within SM, we have a wide spectrum of particle lifetime, including also some quite long lifetimes. For similar reasons, we can naturally have long-lived particles (LLP) in many well-motivated BSM models, like supersymmetry (SUSY) [1–25], dark matter models [26–44], models with heavy neutral leptons [45–65], gauge and Higgs portal models [66–74]. The unique nature of long-lived particle signatures may explain why they have been elusive until now.

Several phenomenological studies have explored a plethora of LLP signatures arising in a wide variety of models [75–94]. The ATLAS, CMS and LHCb [95–121] experimental collaborations at the LHC have searched for different LLP signatures in various sub-detectors for a range of benchmark models, and set limits in the mass and lifetime plane. Apart from these collider detectors, several beam dump experiments also contribute to LLP searches [122–129]. Additionally, there are several proposals for dedicated detectors for LLPs, like FASER-2 [130], FACET [131], MAPP-MoEDAL [132], MATHUSLA [133–135], CODEX-b [136], ANUBIS [137], which are proposed to be placed around different collider interaction points (IP) at the High Luminosity LHC (HL-LHC) in the forward or transverse directions. These detectors are placed far enough from the IP to ensure that we shield most of the SM backgrounds, providing a cleaner environment where with the observation of a few events (3-4), one can claim discovery. The FASER detector placed along the ATLAS beam line has already started collecting data and has constrained some regions of the displaced dark photon parameter space [138]. These dedicated detector proposals make use of existing empty shafts or caverns around the IP in the present collider complex. However, this might not be optimal for LLPs motivated by BSM models. For future colliders, we have the opportunity to optimize the LLP dedicated detector designs to maximize sensitivity for various LLP models. There are few studies which explore the idea of dedicated detectors for future colliders [139–144]. We propose the DELIGHT and FOREHUNT dedicated detectors for the Future Circular Hadronic Collider (FCC-hh) [82, 88].

Given the rich program to look for hints of long-lived particles, we have bounds and projections on the lifetime frontier of various BSM models from present and future collider searches, beam dump experiments, and dedicated LLP detectors. At this stage, it is important to study the unique role that future colliders will play in this search program. This would be instrumental in aiding the physics case of these colliders. The next collider would most likely be a lepton collider, given the crucial role of precision measurements in particle physics, which can even be sensitive to new physics at very high energy scales. It is very common in particle physics that preci-

sion measurements precede and hint towards major discoveries, like the discovery of weak gauge bosons, the top quark, and the Higgs boson. Electron-positron colliders provide a cleaner environment for performing precision studies. There are a number of proposals for electron-positron colliders – the International Linear Collider (ILC) [145, 146], the Circular Electron Positron Collider (CEPC) [147–149], the Compact Linear Collider (CLIC) [150–152] and the Future Circular e^+e^- Collider (FCC-ee) [153, 154]. FCC is a proposal for next-generation collider experiments at CERN after the completion of the Large Hadron Collider (LHC) and High Luminosity LHC (HL-LHC) runs. It is proposed to have two stages – an electron-positron collider (FCC-ee) followed by a proton-proton collider (FCC-hh) [155]. FCC-ee plans to operate at center of mass energies corresponding to the Z pole (91.2 GeV), W^+W^- threshold (161 GeV), HZ production peak (240 GeV), and the $t\bar{t}$ threshold (350/365 GeV), while FCC-hh is aiming for a center of mass energy of 100 TeV.

Owing to a cleaner environment and better particle identification capabilities, the FCC-ee could play a multifaceted role in exploring long-lived particles. To illustrate the unique power of lepton colliders, we investigate the minimal extension of the SM with a light scalar particle, which couples to the SM particles only through the Higgs boson. This is a well-motivated model in the context of dark matter [156], and the light scalar, which mediates interactions with the dark matter, can be long-lived. It is also phenomenologically attractive since the LLP has a wide range of production and decay modes, depending on its mass and couplings with the 125 GeV Higgs boson. There is some uncertainty in the computation of the decay modes of the LLP in a mass range where there is transition between the use of chiral perturbation theory, dispersive relations, and the perturbative spectator model [157]. Experimental collaborations have extensively studied their sensitivities for this model, covering different regions in the mass and mixing angle plane. However, many of the dedicated detector proposals have yet to be approved, and we don’t know which of them will be realized in the future. In this situation, we identify some important benchmarks and study the role of electron-positron colliders in probing them. For simplicity, we perform the analyses in the context of the FCC-ee. The benchmarks are motivated by one of the following questions:

1. Can the FCC-ee be sensitive to any region in the parameter space that lies outside the coverage of any currently proposed experiment?
2. Can the FCC-ee help distinguish this model from others and measure its parameters if we observe a signal in one or more of the proposed future detectors?
3. Can we use the particle identification capabilities of the FCC-ee to be sensitive to the mediator masses, where the dominant decay mode is to mesons, like pions and kaons, where LHC or other hadron colliders lose sensitivity?

We also discuss the possibility of dedicated LLP detectors around the FCC-ee interaction point and their optimal design and position for probing LLPs.

The rest of the paper is organized as follows: in Sec. 2, we discuss the Higgs portal model that we consider here and the various production and decay processes of the dark Higgs boson it entails. In Sec. 3, we discuss the current and future projected sensitivity of various experiments to the parameter space of the dark Higgs model and choose the benchmark points that can be interesting for the electron-positron colliders. We discuss the detection prospect of these benchmarks at the FCC-ee in Sec. 4. We extensively explore various options of dedicated detectors for the FCC-ee in Sec. 5. Finally, we conclude in Sec. 6.

2 Scalar LLPs in the Higgs portal

One of the minimal extensions of the SM is the addition of a scalar field, which is a singlet under the SM gauge group. It only interacts with the SM fields by mixing with the SM Higgs field. The generic renormalizable Lagrangian for this minimal model is as follows [158]:

$$\mathcal{L} = \mathcal{L}_{\text{SM}} + \mu_1^3 S + \mu^2 S^2 - \mu_3 S^3 - \mu_{12} S |H|^2 - \frac{1}{4} \lambda_S S^4 - \epsilon S^2 |H|^2, \quad (2.1)$$

where S is the new scalar field and H is the SM complex scalar Higgs doublet. Imposing a discrete \mathbb{Z}_2 symmetry on S sets $\mu_1 = \mu_3 = \mu_{12} = 0$. Minimizing the scalar potential and diagonalizing the mass matrix leads to the physical states h and ϕ , where the former denotes the discovered 125 GeV SM-like Higgs boson, and the latter is the dark Higgs boson. Thus, after the spontaneous symmetry breaking of the SM Higgs field, we are left with the following Lagrangian for ϕ [158]:

$$\mathcal{L} = -m_\phi^2 \phi^2 - \sin \theta \frac{m_f}{v} \phi \bar{f} f - \lambda v h \phi \phi + \dots, \quad (2.2)$$

where m_ϕ is the mass of the dark Higgs boson, θ is the mixing angle between h and ϕ , λ is the trilinear coupling between the two scalars, f denotes the SM fermions, and $v \approx 246$ GeV is the vev of the Higgs doublet. We have $\lambda \simeq \epsilon v \cos^3 \theta + \mathcal{O}(\sin^2 \theta \cos \theta)$, where the first term is not suppressed by small $\sin \theta$, while the rest of the terms have a $\sin^2 \theta \cos \theta$ dependence. In Eq. (2.2), we have omitted further cubic and quartic interactions of ϕ and h , irrelevant to the phenomenology of the dark Higgs boson discussed in the present work.

The second term in Eq. (2.2) denotes the Yukawa interactions of the SM fermions with the dark Higgs boson, where the Yukawa couplings have the same structure as those of the SM-like Higgs boson, suppressed by the sine of the mixing angle. The various decay modes of ϕ depending on its mass and the relative branching fractions have been discussed extensively in multiple studies [156, 157, 159–161]. The total

decay width of the new dark Higgs boson, $\Gamma_{\phi,\text{tot}}$, scales as:

$$\Gamma_{\phi,\text{tot}}(m_\phi) = \Gamma_{h,\text{tot}}(m_h = m_\phi) \times \sin^2 \theta \quad (2.3)$$

where $\Gamma_{h,\text{tot}}(m_h = m_\phi)$ denotes the total decay width estimated assuming SM-like Higgs boson couplings with its mass set equal to the dark Higgs boson mass. Eq. (2.3) shows that reducing the mixing angle θ , reduces $\Gamma_{\phi,\text{tot}}$, which increases the decay length of ϕ . Since the mean proper decay length of ϕ , *i.e.*, $c\tau$ ¹, is the inverse of $\Gamma_{\phi,\text{tot}}$, the product $\sin^2 \theta \times c\tau$ depends only on the mass of ϕ , and is proportional to the inverse of the quantity $\Gamma_{h,\text{tot}}(m_h = m_\phi)$. Fig. 1 shows the variation of $\sin^2 \theta \times c\tau$ with m_ϕ . Depending on the mass of ϕ , it can have various decay modes, such as $\mu^+\mu^-$, $\pi^+\pi^-$, K^+K^- , $c\bar{c}$, $\tau^+\tau^-$, and $b\bar{b}$. The branching fraction of the dark Higgs boson to mesons, like pions when $2m_\pi < m_\phi < 2.0 \text{ GeV}$ and kaons when $2m_K < m_\phi < 2.0 \text{ GeV}$, is estimated using dispersive analysis [157]. For $m_\phi > 2.0 \text{ GeV}$, the branching fractions to SM particles are calculated using HDECAY [162, 163]. The *gray* shaded mass range around 2.0 GeV in Fig. 1 denotes the region where the total decay width is uncertain due to QCD non-perturbative effects and the transition from the non-perturbative to perturbative regime [161]. The decay length of ϕ for a particular m_ϕ and $\sin \theta$ in the minimal model can be extracted from Fig. 1. In the present work, we consider the parameter region where ϕ is lighter than half the Higgs boson mass, *i.e.*, from $\sim 0.1 \text{ GeV}$ to 60 GeV .

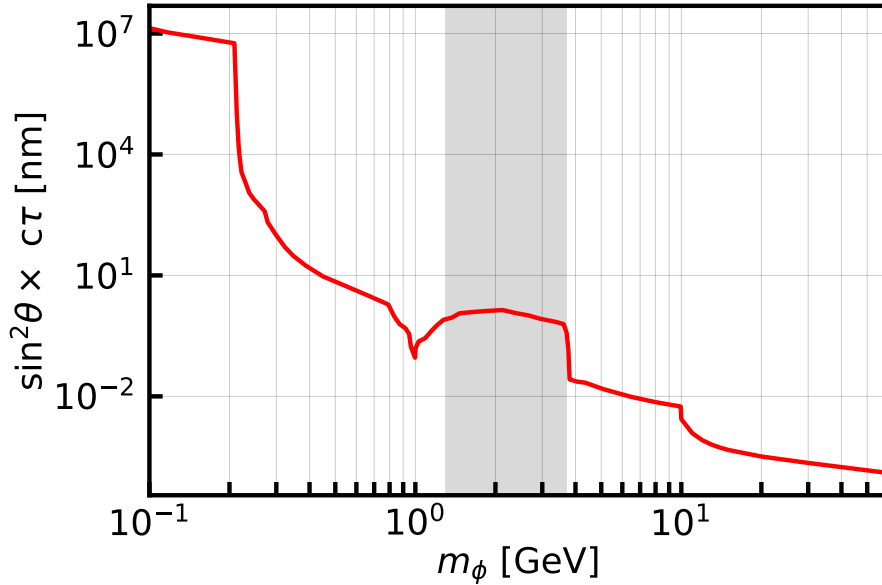


Figure 1: Variation of the $\sin^2 \theta \times c\tau$ as a function of the dark Higgs boson mass in the minimal model.

¹We refer to the mean proper decay length as simply the decay length from hereafter for simplicity, unless stated otherwise.

Depending on the value of the trilinear coupling, we can have different production processes for ϕ at the colliders.

Case A: Negligible Trilinear Coupling

When the trilinear coupling is negligible, $\lambda \approx 0$, ϕ can only be produced via its Yukawa couplings with the SM fermions. These couplings have the same structure as those of the SM-like Higgs boson but are suppressed by the sine of the mixing angle. Therefore, the dominant production is from B meson decays, where the dark Higgs boson is radiated off from the top quark in a $b \rightarrow s$ transition via the $t - W$ loop. The inclusive branching fraction of the B mesons to the scalar LLP is given by [158, 164]:²

$$\text{Br}(B \rightarrow X_S \phi) = 5.7 \sin^2 \theta \left(1 - \frac{m_\phi^2}{m_b^2}\right)^2, \quad \text{for } m_\phi < m_B - m_K. \quad (2.4)$$

where $m_b = 4.75 \text{ GeV}$. The branching ratio is inclusive with respect to both the initial state B -mesons and the final state hadrons with strange quark³. Although the production rate of kaons and light mesons (η , π , etc.) is larger compared to the production rate of B mesons, the branching fraction of kaons to ϕ is much smaller than $\text{Br}(B \rightarrow X_S \phi)$. It is further suppressed for η , η' , and π decays to the dark Higgs boson [158]. Moreover, production from kaons provides sensitivity to a smaller mass range of ϕ , where already strong constraints from beam dump experiments, like E949 [122, 123], are present. Hence, we do not consider these production modes in our study. We consider ϕ masses up to 4.5 GeV in this case, as they can be produced from B meson decays.

Another production mode for ϕ in this case can be from the decay of the Z boson via the process $Z \rightarrow Z^* \phi$, where the off-shell Z boson decays to leptons. This is analogous to Higgs-Strahlung at LEP. This decay mode of the Z boson has a very small partial width proportional to the square of the mixing angle and decreases rapidly with increasing mass of ϕ . However, due to the large luminosity of FCC-ee at the Z pole, we briefly discuss the sensitivity of this production mode of ϕ and the mass range it covers.

Case B: Large Trilinear Coupling

When the trilinear coupling, λ , is large, ϕ can also be pair-produced from an on-shell or off-shell Higgs boson. One possible production process is again via B meson decays, involving an off-shell Higgs boson ($b \rightarrow s \phi \phi$), which has a branching fraction

²We consider the inclusive branching fraction of B mesons decay to any strange meson, X_s , and the dark Higgs boson to reduce the theoretical uncertainties arising from the form factors [158–160, 164].

³The factor 5.7 comes from a combination of the masses of the top quark, bottom quark and W boson, the CKM elements, and the phase space factor in the semi-leptonic B decay, $f_{c/b}$ (Ref. [158]).

around $2.1 \times 10^{-4} \lambda^2$ for an $m_\phi = 1$ GeV dark Higgs boson [158]. Another possibility is Higgs boson production at colliders, where the Higgs boson decays to a pair of ϕ . This process has a much larger branching fraction to the dark Higgs bosons, $\simeq 4700 \lambda^2$ for $m_\phi = 1$ GeV [158]⁴, which is seven orders of magnitude larger than the former. Moreover, the B meson decay process is sensitive to a much smaller range of m_ϕ than the second process, which is sensitive up to $m_\phi \lesssim m_h/2 \sim 60$ GeV. Therefore, in the present work, we only consider the process $h \rightarrow \phi\phi$ for probing the large trilinear coupling scenario.

3 Current status and benchmark choice

In the previous section, we discussed the minimal dark Higgs model and the possible production and decay modes of the new particle. The dominant production mode depends on whether the trilinear coupling can be neglected or not, where for the former, we study the process $B \rightarrow X_s \phi$, and for the latter, we consider the process $h \rightarrow \phi\phi$ at colliders. The production mode also depends on the mass m_ϕ . Since this model has been explored extensively by various experiments, we briefly discuss the current status in this section and select interesting benchmark points for probing this model at the future proposed electron-positron colliders.

Case A: Negligible Trilinear Coupling

This scenario has been extensively studied in various beam dump experiments, neutrino detectors, as well as collider main detectors (see Refs. [161, 166] for an overview). The recently proposed dedicated LLP detectors also have sensitivity to the dark Higgs parameter space. Fig. 2 shows in *gray* the combined bound on the $m_\phi - \sin \theta$ parameter space from the existing experimental results for the mass range $m_\phi \in [0.1, 5]$ GeV. We also show the projected sensitivity of proposed future experiments and phenomenological projections for the HL-LHC to the parameter space in *dashed lines*. We briefly discuss these bounds below.

Beam dump experiments play a major role in searching for new light physics from various meson decays. Experiments like the E949 [122, 123], NA62 [124–126], PS191 [127], CHARM [128], and KOTO [129] have already placed bounds in the parameter space of the mixing angle and mass of the light scalar⁵. The recently approved future experiment SHiP (**S**earch for **H**idden **P**articles) [169, 170] is a proposed fixed target facility at the CERN SPS accelerator. It aims to explore hidden particles with masses less than 10 GeV. For a scalar mass of 1 GeV, SHiP is expected to probe

⁴Note that the current bound of $\text{Br}(h \rightarrow \text{inv}) < 0.11$ from ATLAS [165] implies that $\lambda < 4.8 \times 10^{-3}$ for $m_\phi < m_h/2$, which is the mass range of ϕ considered in this work.

⁵The Big European Bubble Chamber (BEBC) CERN-WA-066 beam dump experiment also places bounds on various light new physics models [167, 168], which can be translated to the dark Higgs boson model as well.

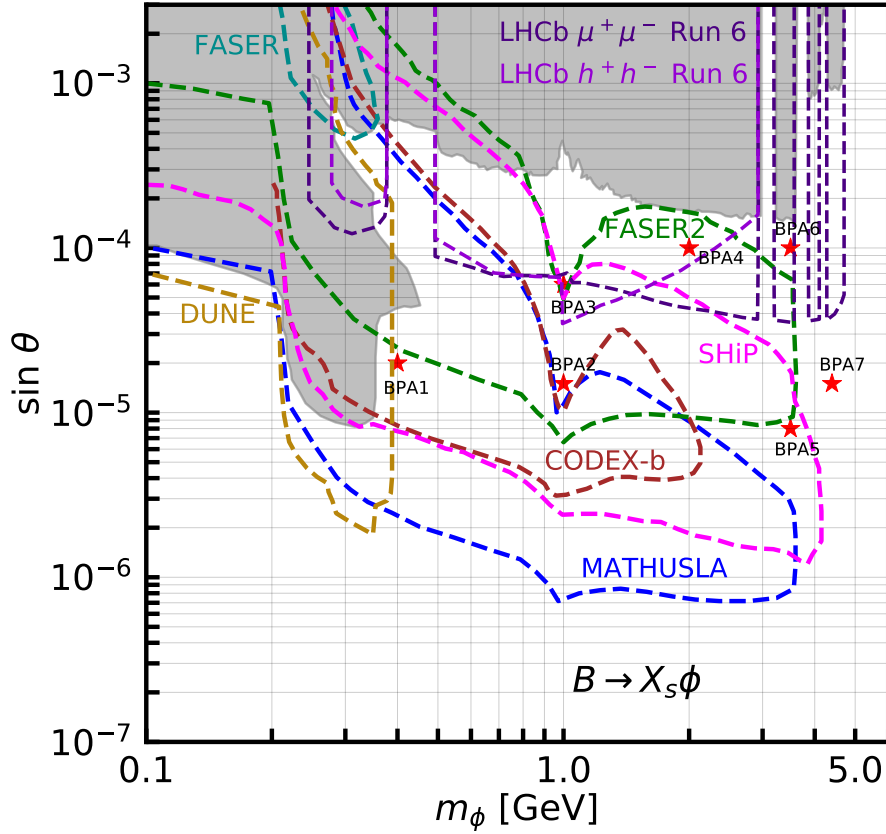


Figure 2: Current status (in *gray*) and future projected sensitivities of proposed experiments (in *dashed lines*) for the dark Higgs boson model when produced from meson decays and the trilinear coupling is negligible. Benchmark points for the present study are marked with *red stars*.

mixing angles between 5×10^{-5} and 2.4×10^{-6} . It is the most sensitive at a mass of 4 GeV, probing a minimum mixing angle of 1.5×10^{-6} .

Neutrino experiments like LSND [171–173] and MicroBOONE [174] also probe regions of the dark Higgs boson parameter space. Excluded regions from these experiments are included in the *gray* region of Fig. 2. The proposed DUNE [175] experiment is expected to improve the sensitivity to lower mixing angles for masses of ϕ below ~ 400 MeV, *i.e.*, where ϕ can be produced from kaon decays.

Searches for new physics via displaced vertices at the various collider experiments, like L3 at LEP [161, 176], LHCb [118, 177] and CMS [178] at the LHC, BaBar [179], and Belle-II [180, 181], can probe ϕ masses up to 4.5 GeV, produced from the process $B \rightarrow X_s \phi$. The bound from LHCb at the LHC has been reinterpreted and projected for the HL-LHC in Refs. [182, 183]. While the projected limit in Ref. [182] assumes a constant scale factor to project the present LHCb limits, Ref. [183] improves the projection by taking into account the strong lifetime depen-

dence of the LHCb limits and including the hadronic decay modes to pions and kaons⁶. Here, we consider the projected limits given for the muon and hadronic final states in the theory paper, Ref. [183]. Being closer to the IP, the collider experiments are sensitive to relatively larger values of mixing angles. For probing smaller values of mixing angles, where ϕ is highly displaced and decays outside the main collider detectors, dedicated LLP detectors, like FASER2 at FPF, MATHUSLA, and CODEX-b, have been proposed. The FASER detector is already collecting data at the ongoing Run-3 of LHC.

With this vast program of searches for dark Higgs boson, we choose seven benchmark points to explore the sensitivity of the future electron-positron colliders. They are described in Table 1 along with the dominant decay modes of the dark scalar and the existing approved or proposed experiments that are sensitive to them. The benchmark points are also marked in Fig. 2 with *red stars*.

Benchmark	m_ϕ (GeV)	$\sin \theta$	$c\tau$ (mm)	Dominant decay modes	Potential experiments to probe			
					FASER2	LHCb (projected)	MATHUSLA	SHIP
BPA1	0.4	2.0×10^{-5}	39666.6	$\pi^+\pi^-$: 76% $\mu^+\mu^-$: 10%	×	×	✓	✓
BPA2	1.0	1.5×10^{-5}	554.3	$\pi^+\pi^-$: 50% K^+K^- : 50%	✓	×	×	✓
BPA3	1.0	6×10^{-5}	34.6	$\pi^+\pi^-$: 50% K^+K^- : 50%	×	×	×	×
BPA4	2.0	10^{-4}	135.2	$\pi^+\pi^-$: 41% K^+K^- : 41% $\mu^+\mu^-$: 12%	✓	✓	×	×
BPA5	3.5	8×10^{-6}	10285.4	$\pi^+\pi^-$: 53% K^+K^- : 21% $\mu^+\mu^-$: 5%	×	×	×	✓
BPA6	3.5	10^{-4}	65.8	$\pi^+\pi^-$: 53% K^+K^- : 21% $\mu^+\mu^-$: 5%	×	✓	×	×
BPA7	4.4	1.5×10^{-5}	95.0	$c\bar{c}$: 65% $\tau^+\tau^-$: 20%	×	×	×	×

Table 1: Choice of benchmark points for negligible trilinear coupling.

These benchmarks are chosen to represent a number of scenarios. For example, SHiP is expected to be sensitive to the benchmarks BPA1, BPA2, and BPA5. On the other hand, benchmarks BPA4 and BPA6 are chosen to have a relatively higher mixing angle, falling within the projected sensitivity of the HL-LHC LHCb analysis. In the scenario where the FASER2 experiment is approved, signals for benchmarks

⁶The reason a constant scale factor for increased luminosity cannot provide a reliable projected sensitivity is due to two key factors: (a) the increase in center-of-mass energy from 8 TeV to 14 TeV, and (b) the relationship between different mixing angles and varying $c\tau$ for different masses of the LLP. These factors result in different detection probabilities at the two energy scales. The projected limit can become stronger or weaker for different masses than that predicted in Ref. [182].

BPA2 and BPA4 are expected to be testable. Similarly, if MATHUSLA is approved, BPA1 can be probed at SHiP and MATHUSLA.

For such benchmark points, where one or more of the existing proposals are sensitive, we want to study whether FCC-ee can provide an additional probe that might be helpful in the identification of the model and an estimate of the model parameters. Some of these benchmarks are chosen just at the sensitivity boundary of specific experiments. For example, BPA3 is just at the boundary of the SHiP, FASER2, and LHCb projected sensitivities. The motivation is that while these experiments might just observe a few signal events, a main collider detector would still be needed to investigate the signals further. Since FCC-ee is possibly the next future collider, we selected these benchmarks for the FCC-ee analysis. Moreover, it is worth studying whether FCC-ee can probe any region of the parameter space beyond the sensitivity of the above-discussed experiments, which motivates the choice of benchmarks BPA3 and BPA7.

Case B: Large Trilinear Coupling

In this case, as discussed in Section 2, the additional trilinear coupling λ opens up the production of the dark Higgs boson ϕ from the decay of the 125 GeV Higgs boson. Since this is here the dominant production mode of ϕ , the most relevant limits come from various searches for LLPs at the main collider detectors, like ATLAS [184] and CMS [185]. Experiments put an upper limit on the $\text{Br}(h \rightarrow \phi\phi)$ for a specific mass and decay length of ϕ , which is related to the parameter λ . In this case, we can extend the mass range of ϕ up to 60 GeV as they are produced from the Higgs boson. Fig. 3 shows the combined excluded $c\tau - \text{Br}(h \rightarrow \phi\phi)$ parameter space for four different values of m_ϕ : 1 GeV, 4.4 GeV, 6 GeV and 40 GeV. The existing limits from the CMS scouting⁷ [186], searches for displaced leptons [114, 187], displaced jets [115, 188], delayed jets [83], and displaced muon spectrometer (CMS MS) clusters [189] are shown in *gray*, while the projected limits from HL-LHC [82], or proposed experiments like MATHUSLA and FASER, are shown in *dashed lines*⁸.

The HL-LHC projected limit denoted $P^S \times D^S$ shows the projected sensitivity estimated in Ref. [82] assuming 50 observed events with a specific set of cuts. These include demanding a prompt object from the Higgs boson production and displaced activity from the dark Higgs boson decay in the muon spectrometer. The *superscript S* is to indicate a relatively softer set of cuts on both the prompt and the displaced object, defined in Ref. [82]. Refs. [81, 83] discuss the reach of dedicated LLP triggers for probing various regions of the dark Higgs model. For example, for a 40 GeV ϕ

⁷Scouting refers to selecting events with lower p_T thresholds to improve sensitivity to light new physics, at the cost of storing less information for offline analyses.

⁸Note that some of the bounds in Fig. 3 end at specific $c\tau$ values since outside this range the particular search loses sensitivity drastically, either since the decay is not displaced enough or it escapes the decay volume.

with $c\tau = 100$ cm, the level-1 trigger in Ref. [83] can select at least 50 signal events even for branching as low as $\text{Br}(h \rightarrow \phi\phi) = 5.4 \times 10^{-6}$. However, these discussions do not consider the acceptance of the high-level trigger system and the offline analyses.

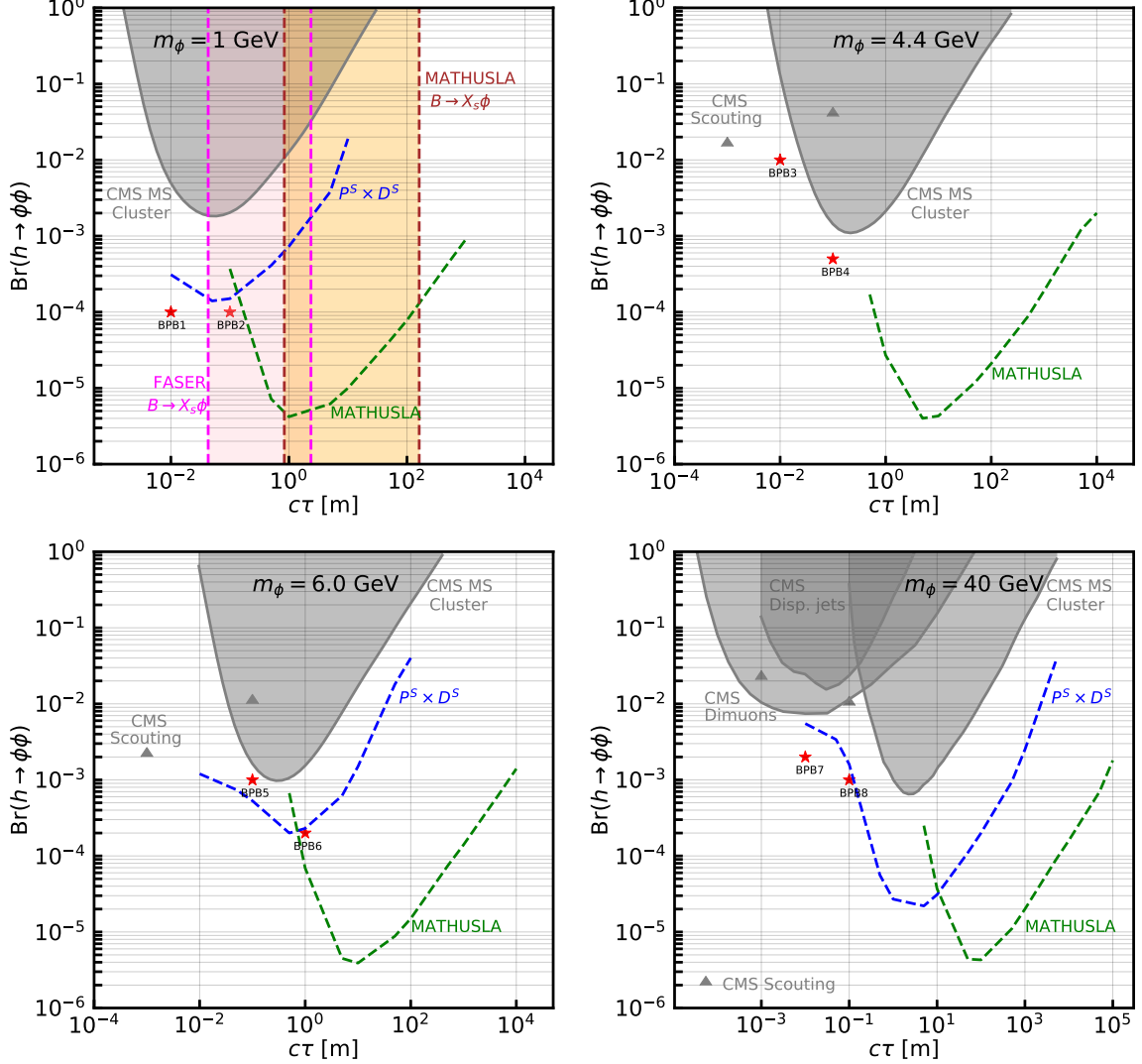


Figure 3: Current status (in *gray*) and future projected sensitivities of proposed experiments (in *dashed lines*) for the dark Higgs boson model when produced from h boson decays in the process, $h \rightarrow \phi\phi$. The *gray triangles* show the upper limit on the $\text{Br}(h \rightarrow \phi\phi)$ for two values of $c\tau$ from the CMS scouting dataset. Benchmark points for the present study are marked as *red stars*.

Based on the above discussion, we select eight benchmark points for the large trilinear coupling scenario where the dark scalar is pair produced from the Higgs boson decay. We describe these benchmarks in Table 2 and mark them in Fig. 3 with *red stars*. Here, we choose benchmarks BPB1, BPB3, BPB4 and BPB7 beyond any present bounds or projections of other proposed experiments, to study the unique

Benchmark	m_ϕ (GeV)	$\sin \theta$	$c\tau$ (mm)	$\text{Br}(h \rightarrow \phi\phi)$	Dominant decay modes	Potential experiments to probe		
						HL-LHC	FASER	MATHUSLA
BPB1	1.0	1.1×10^{-4}	10	10^{-4}	$\pi^+\pi^- : 50\%$ $K^+K^- : 50\%$	×	×	×
BPB2	1.0	3.5×10^{-5}	100	10^{-4}	$\pi^+\pi^- : 50\%$ $K^+K^- : 50\%$	×	✓	×
BPB3	4.4	4.6×10^{-5}	10	10^{-2}	$c\bar{c} : 65\%$ $\tau^+\tau^- : 20\%$	×	×	×
BPB4	4.4	1.5×10^{-5}	100	5×10^{-4}	$c\bar{c} : 65\%$ $\tau^+\tau^- : 20\%$	×	×	×
BPB5	6.0	1.1×10^{-5}	100	10^{-3}	$c\bar{c} : 49\%$ $\tau^+\tau^- : 30\%$	✓	×	×
BPB6	6.0	3.4×10^{-6}	1000	2×10^{-4}	$c\bar{c} : 49\%$ $\tau^+\tau^- : 30\%$	×	×	✓
BPB7	40.0	4.2×10^{-6}	10	2×10^{-3}	$b\bar{b} : 100\%$	×	×	×
BPB8	40.0	1.3×10^{-6}	100	10^{-3}	$b\bar{b} : 100\%$	×	×	×

Table 2: Choice of benchmark points for large trilinear coupling.

prospect of the FCC-ee. Benchmark BPB2 can be probed at FASER2, while BPB5 lies within the projected sensitivity of the HL-LHC muon spectrometer analysis [82]. BPB6 lies just at the edge of the HL-LHC MS search range and MATHUSLA sensitivities, while BPB8 is chosen to be very close to the HL-LHC MS clusters projection for their search reach. For these benchmarks, we intend to explore the complementary role the FCC-ee can play in observing and disentangling the signal in case we find some hints at the HL-LHC and, if approved, the MATHUSLA detector.

4 Role of e^+e^- Colliders in exploring the Benchmarks

In this section, we discuss our analysis strategy at the electron-positron collider to probe the various benchmarks that we selected in the previous section, for both the cases with negligible and large trilinear coupling, respectively. Among the various options for electron-positron colliders, we focus here on the FCC-ee machine, however, our results can be extended to the other options by using the respective detector parameters. As mentioned earlier, the FCC-ee collider is expected to first run at the Z pole with $\sqrt{s} = 91.2 \text{ GeV}$ and later at the peak of the HZ production cross section ($\sqrt{s} = 240 \text{ GeV}$). We use these two options in the present study – the Z factory to examine the sensitivity for the production of ϕ from B meson decays, and the Higgs factory to explore the case where the LLP can be produced from the Higgs boson decay.

For **Case A**, the number of signal events at the FCC-ee is calculated using

$$N = \sigma_{b\bar{b}} \times 2 \times \text{Br}(B \rightarrow X_s \phi) \times \mathcal{L} \times \mathcal{A} \times \epsilon, \quad (4.1)$$

where $\sigma_{b\bar{b}}$ is the production cross-section of b partons at the FCC-ee Z -pole. The factor of 2 arises because either of the two b partons can hadronize into a B meson that decays to ϕ . For the FCC-ee at the Z -pole, $\sigma_{b\bar{b}} = \sigma_Z \times \text{Br}(Z \rightarrow b\bar{b})$, where we use $\sigma_Z = 59.29 \text{ nb}$ and $\text{Br}(Z \rightarrow b\bar{b}) = 0.156$, and the integrated luminosity, $\mathcal{L} = 150 \text{ ab}^{-1}$ [154]. The factor \mathcal{A} takes into account the detector acceptance, which is the probability of the LLP decay within a detector element, and ϵ is the signal efficiency after our analyses, including the detector efficiency of the LLP decay products. We calculate $\text{Br}(B \rightarrow X_s \phi)$ from Eq. (2.4).

For **Case B**, the number of signal events at the FCC-ee becomes

$$N = \sigma_{HZ} \times \text{Br}(h \rightarrow \phi\phi) \times \mathcal{L} \times \mathcal{A} \times \epsilon, \quad (4.2)$$

where σ_{HZ} is the peak of the Higgs boson production cross-section at the FCC-ee (237 fb) and \mathcal{L} is the integrated luminosity (10.8 ab^{-1} [190]). The factor $\text{Br}(h \rightarrow \phi\phi)$ is a free parameter in this case, and we obtain an upper limit on this branching fraction from our analyses at the FCC-ee, which can then be translated to an upper limit on the trilinear coupling, λ . Here, \mathcal{A} and ϵ have the same meaning as in the previous case.

In this section, we first introduce the IDEA detector and its various components. We then show the maximum number of events that we expect to have in each of the detector elements for our chosen benchmarks, using Eqs. (4.1) and (4.2), while assuming a 100% efficiency, *i.e.*, $\epsilon = 1$. Following this, we discuss the realistic efficiencies we consider for the various decay products in different detector components. Additionally, we provide a brief overview of the potential backgrounds and their simulation. Finally, we delve into the details and results of our analyses for the benchmarks in both cases.

4.1 The IDEA Detector

The **I**nnovative **D**etector for an **E**lectron-**P**ositron **A**ccelerator (IDEA) detector [153, 154, 191] is a cylinder designed to be centered at one of the IPs of the FCC-ee collider. It includes a vertex detector (VTX), a drift chamber (DCH), a dual-readout calorimeter (DRC), and a muon system (MS). The VTX is the innermost part of the detector that surrounds the beam pipe and is made of silicon pixels, which have excellent tracking resolution and high efficiency for charged particles. The DCH is designed for good tracking, high-precision momentum measurement, and excellent particle identification. The 2 T solenoid for the IDEA detector is positioned outside the DCH. There is also a preshower detector placed between the magnet and the calorimeter in the barrel region, as well as in front of the end-cap calorimeters in the forward regions to identify charged particles and photons. In addition, it can also tag a π^0 from its decay to two photons. The DRC measures the energy of electrons/photons and hadrons, providing good intrinsic discrimination between muons,

electrons/photons, and hadrons for isolated particles. The muon system, is characterized by a high-resolution momentum measurement for muons, and consists of layers of chambers [192] embedded in the magnet yoke.

Detector component	R_{in} (mm)	R_{out} (mm)	Z_{in}^{half} (mm)	Z_{out}^{half} (mm)
Silicon pixel detector (VTX)	17	340	400	2000
Drift chamber (DCH)	345	2020	2125	2125
Solenoid	2100	2400	2500	2500
Preshower	2400	2500	2500	2600
Dual-readout calorimeter (DRC)	2500	4500	2600	4500
Muon system (MS)	4500	5500	4500	6500

Table 3: The detector dimensions for the IDEA detector used in this work based on Refs. [154, 193, 194].

We show the dimensions of these various detector components in Table 3, and employ these parameters to model the geometry of the IDEA detector. Using the coordinates of the LLP decay products, we reconstruct the position of the LLP decay vertex in both the transverse (d_T) and the z direction (d_z). These (d_T , d_z) coordinates help us identify the specific component of the IDEA detector where the LLP decays or whether the decay occurs outside the main detector.

Benchmark	Number of LLP decays for $\mathcal{L} = 150 \text{ ab}^{-1}$						
	VTX	DCH	Solenoid	Preshower	DRC	MS	Outside
BPA1	5	17	1	1	21	13	6175
BPA2	315	720	31	28	485	228	1348
BPA3	32750	16977	184	134	1014	84	50
BPA4	42924	47166	861	834	8534	1937	1611
BPA5	2	6	0	0	8	5	188
BPA6	22573	10029	32	24	124	4	0
BPA7	42	28	0	0	1	0	0

Table 4: Number of events detected in various components of the IDEA detector assuming 100% efficiency for our chosen benchmark points from **Case A**.

In Tables 4 and 5, we list the number of observed events that are expected in various parts of the IDEA detector assuming 100% efficiency for our chosen benchmark points of the dark scalar model, where the dark Higgs bosons are produced from the decay of B mesons and Higgs bosons, respectively. This suggests for each benchmark the detector elements that will be the most useful for analyzing these benchmarks. For instance, BPA1 and BPA5 mostly decay outside the detectors, whereas BPA3, BPA4, and BPA6 have a significant number of events within the VTX and DCH detector elements. Benchmarks BPA1, BPA2, BPA3, BPA4, and

Benchmark	Number of LLP decays for $\mathcal{L} = 10.8 \text{ ab}^{-1}$						
	VTX	DCH	Solenoid	Preshower	DRC	MS	Outside
BPB1	194	179	2	2	9	1	0
BPB2	38	106	6	5	87	43	155
BPB3	25487	3356	0	0	0	0	0
BPB4	610	961	32	29	281	54	51
BPB5	1487	1932	53	44	345	47	25
BPB6	49	150	9	9	144	79	403
BPB7	5119	0	0	0	0	0	0
BPB8	2555	248	0	0	0	0	0

Table 5: Number of events detected in various components of the IDEA detector assuming 100% efficiency for our chosen benchmark points from **Case B**.

BPA5 also have a considerable number of decays within the MS, in addition to the inner detectors. In **Case B**, BPB3 primarily decays within the VTX component, while BPB6 predominantly decays outside the IDEA detector. This is important since the collider analysis of the benchmarks depends on where the dark Higgs boson decays, in addition to its decay mode.

Detector component	Particles	Energy threshold (GeV)	Efficiency
Vertex detector (VTX)	charged particles	$0.1 < E < 0.3$	0.06
Drift Chamber (DCH)		$0.3 < E < 0.5$	0.65
		$E > 0.5$	0.997
Solenoid	e^\pm, μ^\pm , charged hadrons	$E > 0.5$	0.98
Preshower	γ	$E > 0.10$	
DR calorimeter		$E > 0.5$	0.98
Muon system	μ^\pm	$E > 0.10$	0.98

Table 6: Fixed efficiencies of particle selection in different components of the FCC-ee IDEA detector.

We have assumed 100% detection efficiency of the LLP decay products until now. However, the number of signal events we observe in each detector element will depend on the decay mode, the position of the decay vertex, and the efficiency of observing the particles from the LLP decay in the subsequent detector elements. Based on estimates from Refs. [195], [196], and [197] for the tracker, calorimeter, and muon spectrometer efficiencies, respectively, we present in Table 6 the detection efficiencies we have assumed for various particles within each component of the IDEA detector. For the solenoid and preshower regions, we have employed similar efficiencies. We perform our analyses with these fixed efficiencies. However, the efficiencies will also depend on the position of the decay vertex of the LLP. The farther it decays from the

IP in a particular detector component, the smaller the expected detection efficiency. The parametrization of this effect is still unavailable in fast detector simulations, like `Delphes` [198]. We later comment on the results assuming that the efficiencies drop linearly with increasing displacement, *i.e.*, they depend on the d_T of the LLP decay, and the R_{in} and R_{out} of the detector element. Next, we discuss the possible backgrounds from the SM in the analysis of a light, long-lived particle decaying into muons, pions, kaons, and light jets.

4.2 Backgrounds

The dominant backgrounds for light, long-lived particles are the SM long-lived mesons and baryons. In this section, we enumerate all the possible SM long-lived hadrons with varying masses and decay lengths. Looking at the lab frame decay length distributions of these particles and knowing their possible decay modes are crucial in order to recognize the relevant backgrounds in light LLP searches. Some of these particles might have a smaller decay length than the signal LLP. Despite that, the high production cross-section of these SM particles and the exponential nature of the decay length distribution can lead to a significant long tail, contributing to backgrounds in our analysis. Moreover, some of these particles can come from the decay of another long-lived SM particle, which increases the displacement of the decay.

Mesons	m (GeV)	$c\tau$ (mm)	Baryons	m (GeV)	$c\tau$ (mm)
K_L	0.498	15330	Ξ^0	1.315	87.1
K_S	0.498	26.84	Λ	1.116	78.9
B^\pm	5.279	0.491	Ξ^-	1.322	49.1
B^0	5.279	0.459	Σ^-	1.197	44.34
B_S^0	5.367	0.439	Ω^-	1.672	24.61
D^\pm	1.869	0.312	Σ^+	1.189	24.04
D_S^\pm	1.968	0.150	Λ_b^0	5.619	0.369
D^0	1.865	0.123	Ξ_b^-	5.791	0.364
			Ξ_b^0	5.788	0.364
			Ξ_c^+	2.468	0.132
			Λ_c^+	2.286	0.06
			Ξ_c^0	2.471	0.0336

Table 7: List of SM long-lived mesons and baryons, along with their mass (m) and decay length ($c\tau$) in decreasing order of $c\tau$. The values of mass and $c\tau$ are obtained from `PYTHIA 8`.

In order to obtain a list of these long-lived hadrons, we generate Z bosons at $\sqrt{s} = 91.2 \text{ GeV}$ using `PYTHIA 8` [199, 200], with the Z bosons decaying to quarks. These hadronize to produce a variety of mesons and baryons, which can have dis-

placed decays. We generate 10^9 events,⁹ which is still a factor of ~ 8900 smaller than the expected number of Z bosons produced at the FCC-ee Z -pole. This demonstrates how large these backgrounds from displaced hadron decays can be, with a significant number of events populating even the tails of the d_T distributions. Table 7 lists the mesons and baryons with long decay lengths in decreasing order of their $c\tau$. Although J/Ψ and $\Psi(2S)$ are not shown in Table 7 because they are not long-lived, it is important to note that they still travel a few millimeters before decaying, originating from the displaced decay of a boosted B meson. Many of these particles have the same final states as the decay products of the light dark Higgs bosons. For example, J/ψ can decay to two muons or K_S can decay to two pions. This would make the search difficult for LLPs having masses and lifetimes closer to these SM hadrons. We discuss them individually while discussing the analyses for the different decay modes of ϕ . But before that, we want to obtain a generic d_T threshold that can suppress most SM backgrounds.

We divide the SM long-lived particles into three categories based on their decay lengths and show their d_T distributions at the Z factory ($\sqrt{s} = 91.2$ GeV) in Fig. 4, where the number of events is calculated for an integrated luminosity of 150 ab^{-1} . The *top left*, *top right* and *bottom* panels respectively show the distributions of particles as a function of d_T . There is a significant number of events extending up to ~ 50 mm (*e.g.*, J/ψ), ~ 100 mm (*e.g.*, D^\pm) and going beyond 1 m (K_S). We observe that the bottom and charm mesons belong to the second category and travel a transverse distance up to ~ 100 mm. Among these, the number of D^\pm meson decays extends the farthest in d_T , since the D^\pm itself has a long decay length, and additionally, it can come from the decay of a B^\pm . We fit the number of D^\pm decay events as a function of d_T to estimate the minimum d_T threshold for which the SM D^\pm background becomes zero, or negligible. We obtain a value of d_T close to 130 mm. Taking a conservative approach, we shall use a cut of $d_T > 150$ mm to reduce all the SM backgrounds from the decay of charm and bottom mesons.

Note that this does not eliminate the third category of hadrons, which have much longer tails in d_T . However, fitting won't provide the correct estimate of the maximum value of d_T for these hadrons, as they would populate displacements up to the calorimeters, where they deposit energy. We discuss them in detail in the subsequent sections, depending on the decay modes of the LLP and these hadrons, and highlight the specific challenges and ways to deal with them.

4.3 Analysis Strategy

In this section, we briefly discuss the analysis strategy used in this study. Before doing so, we illustrate in Fig. 5 the signal processes we are examining, which include

⁹FCC-ee shall generate 10^{12} Z bosons; however, due to limited computing resources, we generate 10^9 .

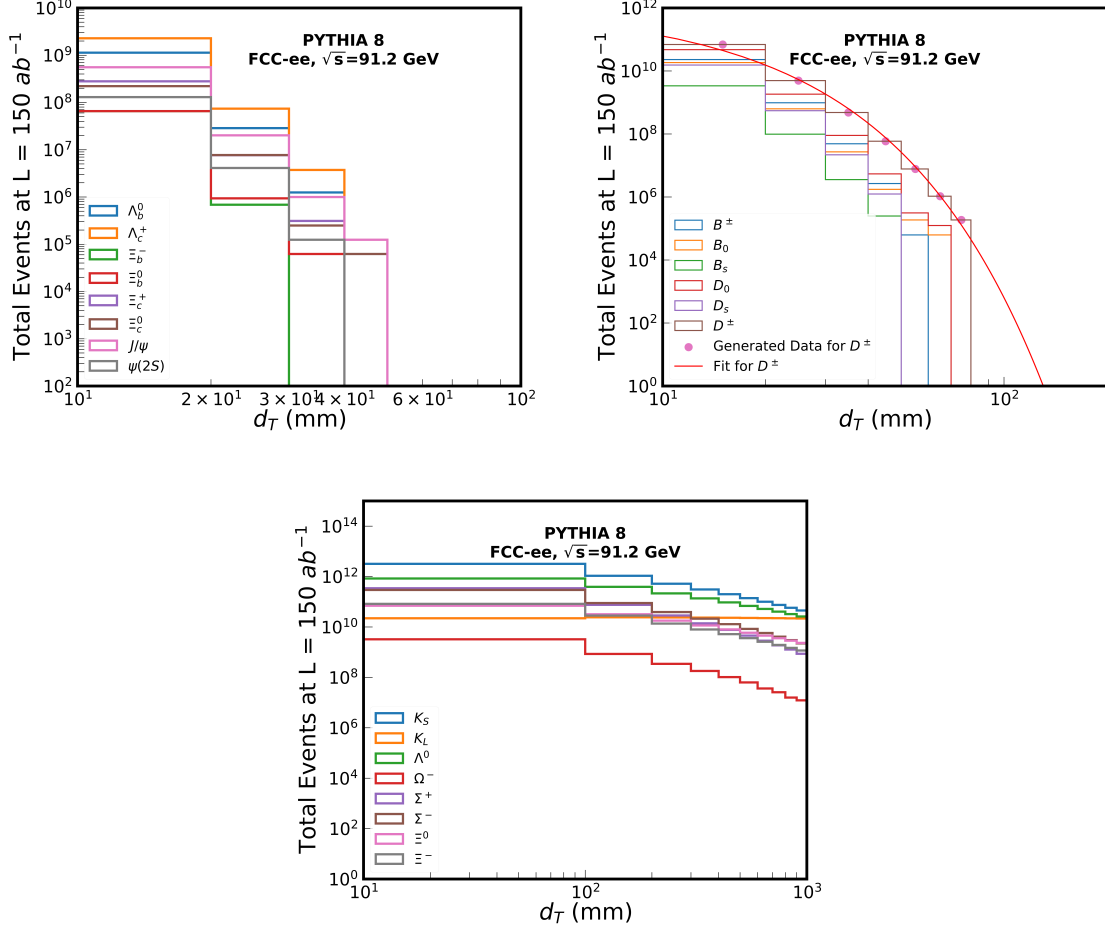


Figure 4: Number of events as a function of the transverse decay length in the lab frame, d_T , for various SM long-lived mesons and baryons.

both the decays of B mesons at the Z factory and the decays of Higgs bosons during the HZ production peak run at FCC-ee. We also highlight some dominant SM backgrounds discussed in the previous section in Fig. 5.

For our analysis, we first identify all the stable particles and the coordinates of the decay vertex where they originate in the IDEA detector. This information helps us to apply the appropriate efficiency factors based on Table 6. Next, the particles that meet the efficiency criteria are clustered into vertices with other detected particles, given their origins are within 1 mm of each other. Finally, we have a list of vertices and store variables describing these vertices as listed below. This strategy is illustrated in Fig. 6.

To analyze the signal and background, we consider the following variables to describe the features of a displaced vertex in an event:

- detector element based on the location of the vertex, D_{vtx} ,

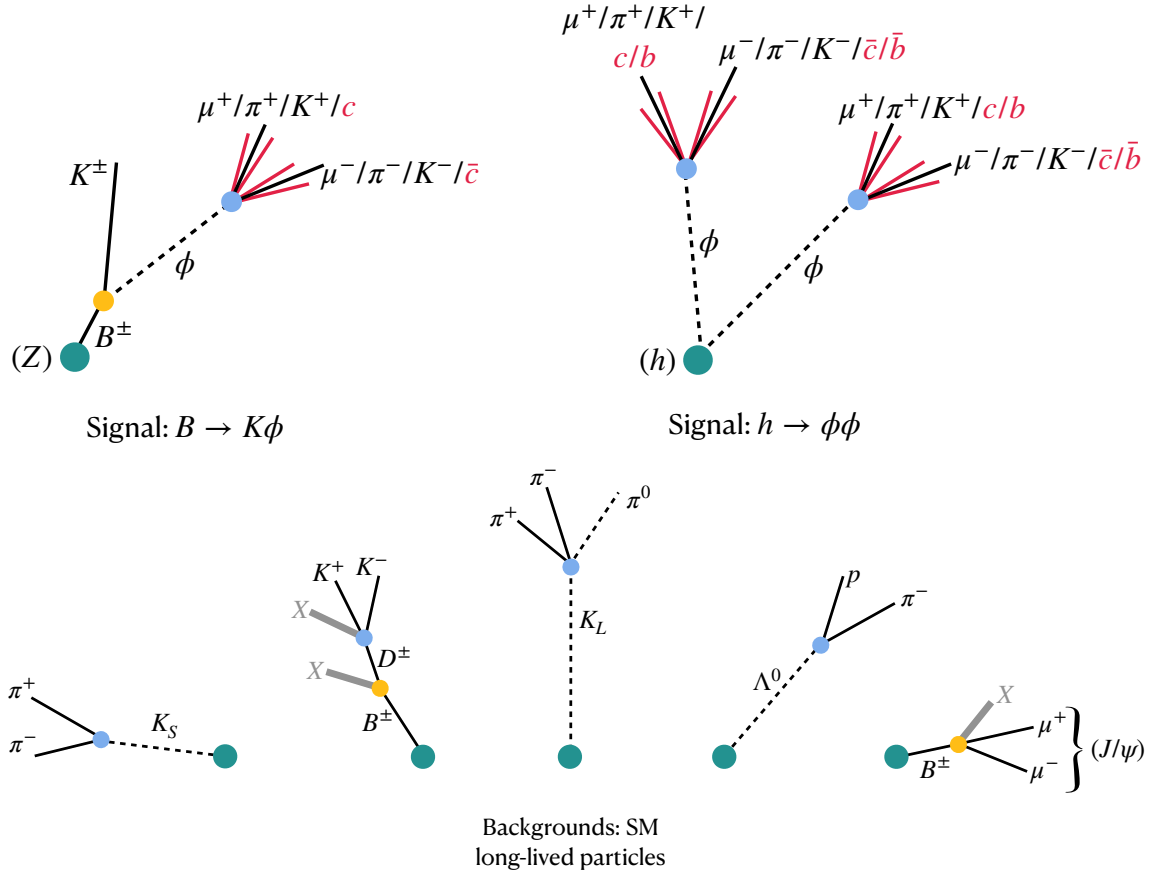


Figure 5: Illustrations of the two signal processes at the FCC-ee (*top panel*) and the SM backgrounds (*bottom panel*).

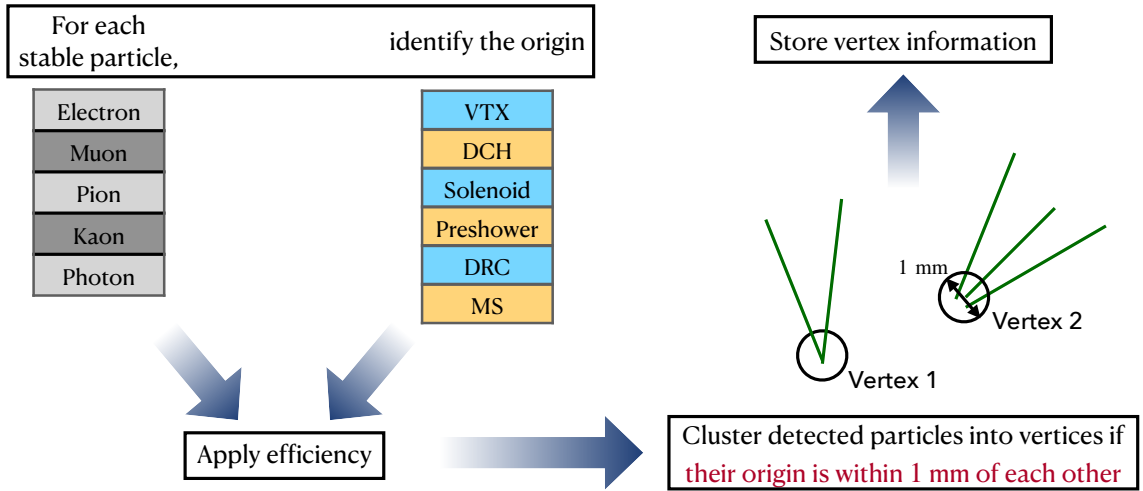


Figure 6: Schematic outline of our analysis strategy.

- number of charged particles created at the vertex, N_{ch} ,
- total energy of the particles produced at the vertex, E ,
- transverse displacement of the vertex from the origin, d_T ,
- number of muons (N_μ), pions (N_π), kaons (N_K), and electrons (N_e) originating at the vertex,
- invariant mass of the final state particles associated with the vertex, m_{vtx} ,
- the impact parameter of the vertex, d_0 .

Based on the final state, we apply different cuts based on these variables to minimize the SM background, as much as possible. In the following sections, we will categorize our benchmarks according to their final states and discuss the specific analyses and results for each of them.

4.4 LLPs with Negligible Trilinear Coupling

In this section, we explore the prospects of LLPs with negligible trilinear coupling at the FCC-ee, *i.e.* **Case A**. The signal benchmarks are listed in Table 1. We generate the signal and the SM background events using **PYTHIA 8** for an e^+e^- beam at a center of mass energy $\sqrt{s} = 91.2 \text{ GeV}$. The background is due to Z bosons produced at $\sqrt{s} = 91.2 \text{ GeV}$, that decay either hadronically to quarks or leptonically. The hadronic branching of the Z boson is 69.2%, out of which the $Z \rightarrow b\bar{b}$ branching is 15.6%. The majority of SM long-lived particles arise from the hadronization of quarks into various mesons and baryons, as discussed in detail in Section 4.2. We generate 10^9 events for the SM background from inclusive Z decays and 10^5 events for each signal benchmark, where we only simulate the process $Z \rightarrow b\bar{b}$ for the signal.

4.4.1 Analysis in the Di-muon Final State

From Table 1, we observe that benchmarks BPA1, BPA4, BPA5, and BPA6 respectively have 10%, 12%, 5%, and 8% branching ratio of the ϕ to $\mu^+\mu^-$. We generate 10^5 events for these LLP signal benchmarks however with a 100% branching ratio for $\phi \rightarrow \mu^+\mu^-$. The SM background $Z \rightarrow \mu^+\mu^-$ is a prompt decay and, therefore, does not contribute at larger values of d_T . Displaced muons can also be produced from the decays of $J/\psi(1S)$ and $\psi(2S)$ into $\mu^+\mu^-$. As discussed in the previous section, long-lived B mesons decay into these particles after a few millimeters. Therefore, even the prompt decays of J/ψ and ψ lead to displaced muons.

To identify the contribution of the SM backgrounds for the dimuon final state, we apply a set of cuts to select events with a reconstructed displaced vertex having exactly two muons in the vertex. We also demand that the vertex location is within the VTX or the DCH detectors since SM hadrons travel further to the calorimeters

and deposit their energy. But the dimuon signal can be observed even when the ϕ travels beyond the DCH all the way to the MS. These cuts are summarized in Table 8. We calculate the invariant mass of the particles produced at the vertex, $m_{\mu^+\mu^-}$. The two-dimensional distribution of the SM background of inclusive Z decays as a function of $m_{\mu^+\mu^-}$ and d_T is shown in Fig. 7. We observe a continuous background populating the low invariant mass and d_T region, coming from displaced muons produced from various B meson decay chains. We also observe two resonances in $m_{\mu^+\mu^-}$ at $m_{J/\psi} \sim 3.1$ GeV and $m_{\psi(2S)} \sim 3.7$ GeV, corresponding to the displaced J/ψ and ψ , coming from B meson decays, with their d_T values extending up to 40 mm.

Selection cuts to study the SM dimuon background
$D_{\text{vtx}} \in \text{VTX or DCH}$
$N_{\text{ch}} = 2$
$N_{\mu} = 2$
$E > 1 \text{ GeV}$
$d_T > 5 \text{ mm}$

Table 8: Selection cuts for the dimuon final state to study the SM background.

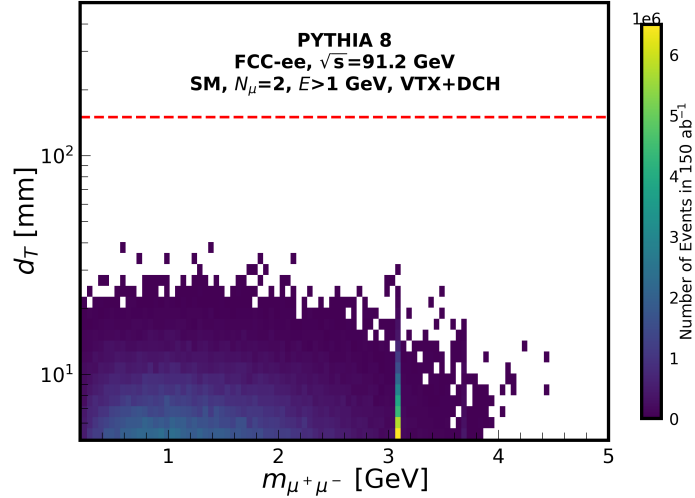


Figure 7: Two-dimensional distribution of the the SM background as a function of the invariant mass of the dimuon vertex and the d_T . The d_T threshold motivated from fitting the SM background is shown as a *red dashed line* at $d_T = 150$ mm.

From Section 4.2, we choose the cut $d_T > 150$ mm for a conservative analysis, which can reduce the background from all the displaced charm and bottom mesons to zero, as can be seen from Fig. 7. Given that the dominant background for the dimuon final state comes from displaced B meson decays, we apply this conservative d_T threshold for all the benchmarks and calculate the resulting number of signal

Final cuts for the dimuon final state
$D_{\text{vtx}} \equiv \text{out to the MS}$
$N_{\text{chg}} = 2$
$N_{\mu} = 2$
$E > 2 \text{ GeV}$
$d_T > 150 \text{ mm}$

Table 9: Final cuts applied for the dimuon final state for the signal benchmarks to reduce the SM backgrounds to zero.

events. Since the final state contains muons, we extend the detection of signal events all the way to the MS detector component. The final cuts applied on the signal benchmarks are listed in Table 9. We apply these cuts on the signal events for benchmarks BPA1, BPA4, BPA5, and BPA6. The number of signal events obtained from the analysis for each benchmark, including the respective branching to muons, is listed in Table 10. We observe that BPA4 and BPA6 can be easily probed in the dimuon channel. BPA1 has a very large decay length, causing most of the decays to lie beyond the MS. Still, three events with zero background can be observed with our analysis. We recommend that the LLP search be carried out in this benchmark with increased luminosity. BPA5 has the weakest prospect, where we expect to observe only a single event. Due to low $\sin \theta$, the ϕ -production rate of BPA5 is very low, and a high $c\tau$ causes most of the LLPs to decay outside the detector. We shall revisit these two benchmarks when we study the prospect of dedicated detectors for FCC-ee in Section 5.

Benchmarks	Dimuon analysis for decays out to the MS		
	m_{ϕ} (GeV)	$c\tau$ (mm)	Number of events
BPA1	0.4	39666.6	3
BPA4	2.0	135.2	9352
BPA5	3.5	10285.4	1
BPA6	3.5	65.8	915

Table 10: Number of signal events in BPA1, BPA4, BPA5, and BPA6 after a cut-based analysis. The number of background events in each case is expected to reduce to zero due to the d_T cut.

We have achieved zero background with the above analysis strategy. However, we study whether there are ways to suppress the background using some other features of the signal process, while relaxing the d_T cut. In the signal process, $B \rightarrow K\phi$, a kaon is produced along with the ϕ from the decay of the B meson. Thereby, in addition to our list of selection cuts in Table 8 for the SM background events, we demand that

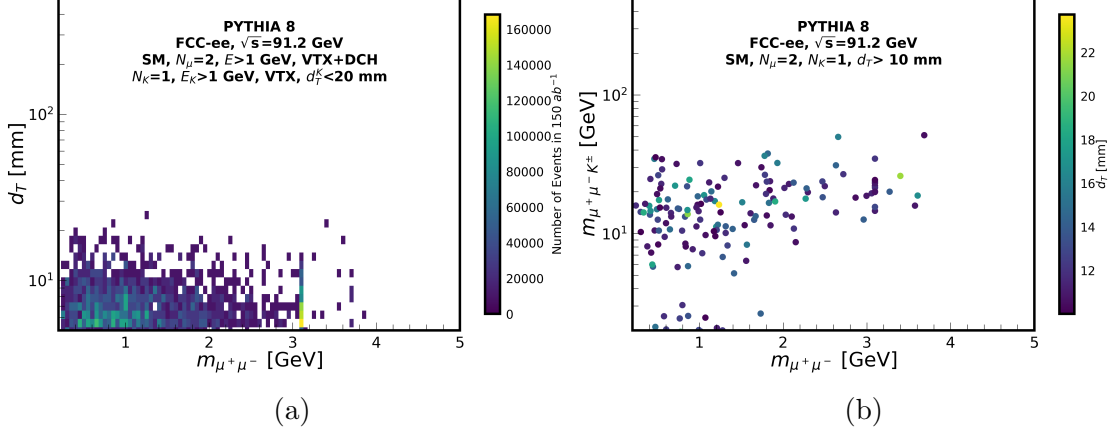


Figure 8: *Left:* Two-dimensional distribution of $m_{\mu^+\mu^-}$ and d_T of the vertex for the SM background after demanding a prompt kaon in the event; *Right:* Two-dimensional distribution of $m_{\mu^+\mu^-}$ and $m_{\mu^+\mu^-K^\pm}$ for the SM background after demanding a prompt kaon in the event and $d_T > 10$ mm for the dimuon vertex.

there must be an isolated prompt kaon in the VTX detector element with $E > 1$ GeV, but $d_T < 20$ mm. The d_T cut ensures that the K^\pm from the B decay in the signal is not displaced very much. The *left* panel of Fig. 8 shows the distributions of the SM background in the $m_{\mu^+\mu^-} - d_T$ plane, with the $N_{K^\pm} = 1$ condition. The *right* panel of Fig. 8 presents the background events that remain after applying the kaon cut, with the dimuon vertex having a transverse distance $d_T > 10$ mm. The panel shows the $(m_{\mu^+\mu^-}, m_{\mu^+\mu^-K^\pm})$ plane. Here $m_{\mu^+\mu^-K^\pm}$ represents the combined invariant mass of the two identified muons and the isolated charged kaon, respectively. The color bar indicates the values of d_T for the dimuon vertex. For signal events, the invariant mass $m_{\mu^+\mu^-K^\pm}$ should be close to the mass of the B meson.

If the additional criteria of a kaon or even a mass window cut on $m_{\mu^+\mu^-K^\pm}$ near the B meson mass is applied, the background can be suppressed even at moderate values of d_T , which can increase the signal efficiency. The reduction in the background can be already seen from comparing the number of SM events shown in the *color bars* of Fig. 7 and the *left* panel of Fig. 8. This provides an alternate strategy to reduce the SM background to the LLPs decaying to two muons. This would only be possible for charged kaons coming from B^\pm decays. For the neutral B^0 decays, the neutral kaon will have displaced decays in various detector elements, which is difficult to identify and associate with the B meson decay. Since we use an inclusive branching ratio of B mesons to the dark Higgs boson, we cannot separate the charged B meson decays from the neutral ones to quote the corresponding signal efficiencies here. This would require estimating the individual branching fractions, which have large uncertainties from form factors.

Beyond the benchmark studies, we generate LLPs decaying to two muons for

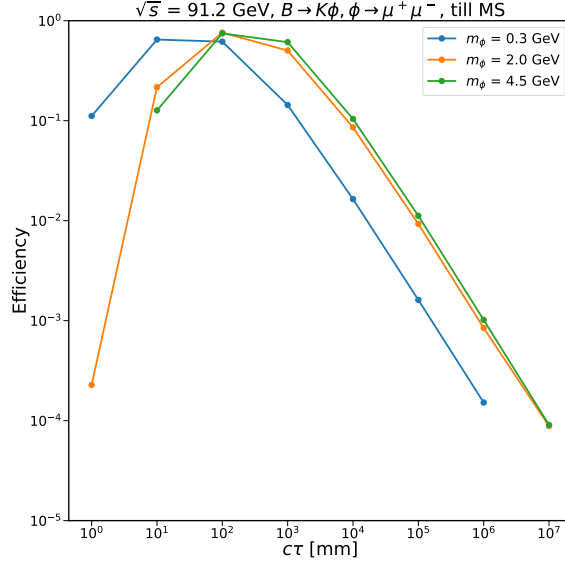


Figure 9: Efficiency for the di-muon decay mode of the LLP ϕ with the variation of $c\tau$ for three masses m_ϕ . The generation of the LLP involved the $Z \rightarrow b\bar{b}$ process where one B meson decays via the BSM process $B \rightarrow K\phi$, and the other B decays to SM particles. The final state muons were detected while requiring the cut: $150 \text{ mm} < d_T < 5500 \text{ mm}$.

various m_ϕ and $c\tau$ values. From the $Z \rightarrow b\bar{b}$ process, we require one of the B mesons to have a non-standard decay to LLP, while the other B decays to SM particles. We follow the selection criteria in Table 9 and calculate the signal efficiency of the analysis. We show the efficiency for this analysis in Fig. 9, which can be useful to translate the results for a range of masses and lifetimes, with arbitrary branching to muons. An efficiency map in the $c\tau$ - m_ϕ plane is shown in Fig. 22 in Appendix A.

4.4.2 Analysis in the Di-pion and Di-kaon Final States

Almost all the benchmarks in Table 1 have a significant branching ratio of the ϕ to the di-pion final state, $\text{Br}(\phi \rightarrow \pi^+\pi^-)$. It ranges from 76% for BPA1, 50% for BPA2 and BPA3, 41% for BPA4, and 53% for BPA5 and BPA6. Benchmarks BPA2, BPA3, BPA4, BPA5, and BP6 have a $\text{Br}(\phi \rightarrow K^+K^-)$ of 50%, 50%, 41%, 21%, and 21%, respectively. Both the di-pion and di-kaon analyses proceed similarly. We first select the appropriate vertices inside the vertex detector and the drift chamber. These selection cuts for the background events are listed in Table 11.

The two-dimensional distribution of the background events in di-pion and di-kaon final states in the di-meson invariant mass - d_T plane after applying the selection cuts is shown in Fig. 10. The mass of the charged pion is 0.139 GeV . Hence, the events start populating from $m_{\pi^+\pi^-} \gtrsim 0.28 \text{ GeV}$. The SM events with pions coming from the decay of a K_S are observed at $m_{\pi^+\pi^-} = m_{K_S} \sim 0.5 \text{ GeV}$, which corresponds to

Selection cuts to study the SM di-pion/di-kaon background
$D_{\text{vtx}} \in \text{VTX or DCH}$
$N_{\text{ch}} = 2$
$N_{\pi/K} = 2$
$E > 1 \text{ GeV}$
$d_T > 5 \text{ mm}$

Table 11: Selection cuts applied to study the SM background events when the final state contains two charged pions or two kaons.

the resonance in the *left* panel of Fig. 10. These di-pion vertices are displaced, as inferred from the d_T reaching up to 2 m.

Furthermore, we can also have displaced di-pion vertices from the decay $K_L^0 \rightarrow \pi^+ \pi^- \pi^0$, where the VTX and DCH detectors reconstruct only the two charged pions and associate them to the same vertex. The reconstructed mass of the K_L decay products depends on the missing energy of the unassociated π^0 . Hence, we observe the band of events with decay vertices clustered within 0.28 GeV ($2m_\pi^\pm$) $\lesssim m_{\pi^+ \pi^-} \lesssim 0.36 \text{ GeV}$ ($m_{K_L^0} - m_{\pi^0}$) in the *left* panel of Fig. 10. These extend to large values of d_T due to the large decay length of the K_L . The SM process $K_S^0 \rightarrow \pi^+ \pi^- e^+ e^-$ also contributes to the production of events observed as di-pion vertices, when the low energy electrons miss detection, albeit with a small decay branching ratio for the K_S^0 (5×10^{-5}). This populates the region $0.36 \text{ GeV} \lesssim m_{\pi^+ \pi^-} \lesssim 0.5 \text{ GeV}$, extending again to large values of d_T .

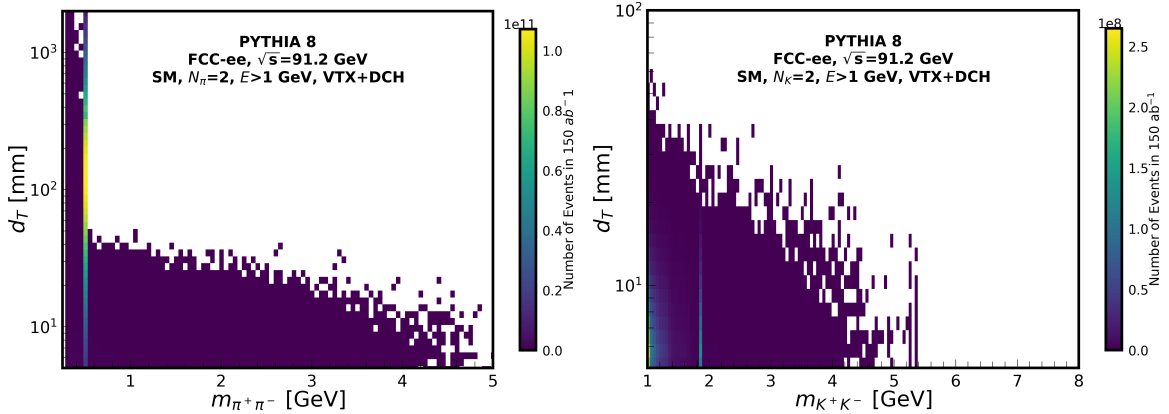


Figure 10: *Left:* Invariant mass of the di-pion decay with respect to the d_T of the vertex for the SM background. *Right:* Invariant mass of the di-kaon decay with respect to the d_T of the vertex for the SM background.

From the distribution for the di-pion case, it is clear that benchmarks with masses less than 0.5 GeV decaying to two pions are incredibly difficult to probe, at least with the use of the invariant mass and d_T variables. The long lifetimes of the $K_{L/S}$

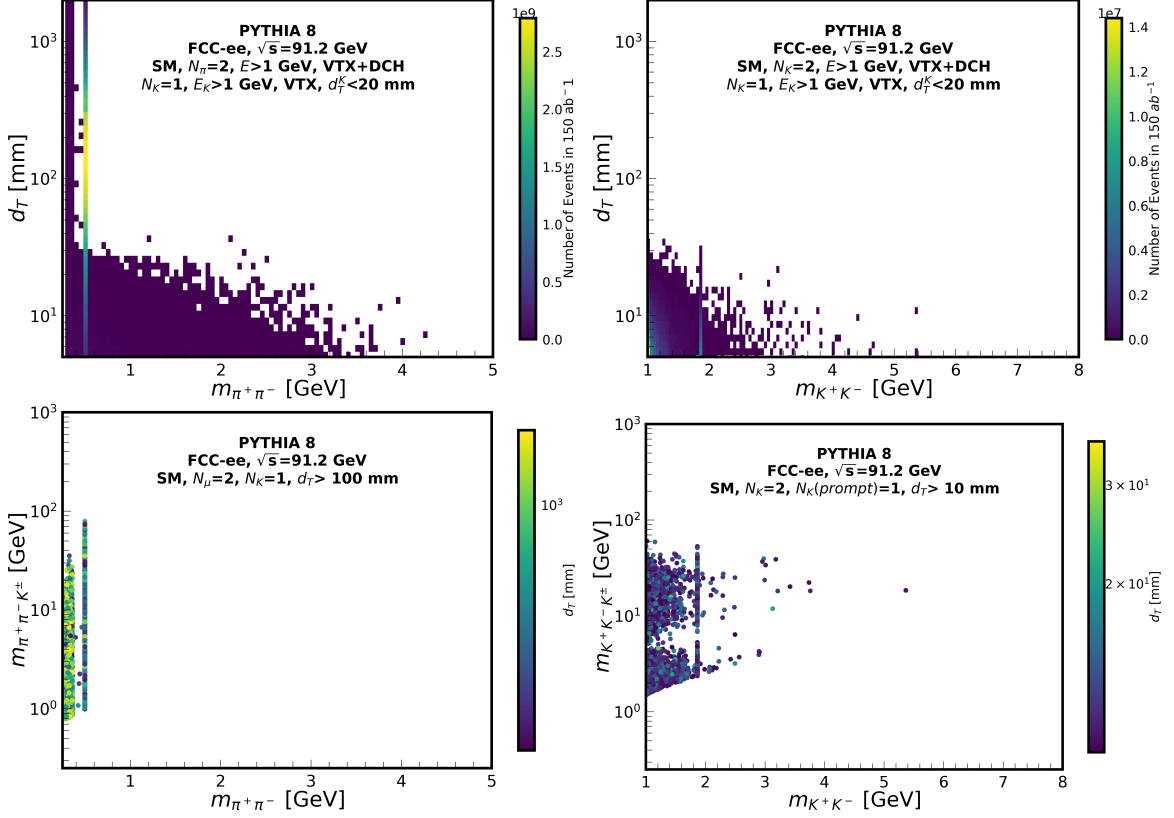


Figure 11: *Top row:* Invariant mass of the di-pion (*left*) and the di-kaon final state (*right*) with respect to the d_T of the vertex for the SM background. *Bottom row:* The left panel shows the invariant mass of the di-pion final state with respect to the invariant mass of the di-pion and kaon system; the right panel shows the invariant mass of the di-kaon final state with respect to the invariant mass of the di-kaon and kaon system.

mesons result in a huge background in the low mass region. Even with an additional prompt kaon, the background still populates the $m_{\pi^+\pi^-K^\pm} \simeq m_{B^\pm} = 5$ GeV region for $m_{\pi^+\pi^-} = 0.4$ GeV. This is highlighted for the di-pion final state in the *bottom left* panel of Fig. 11. Therefore, it is not possible to reduce the SM background for these low-mass benchmarks.

For the di-kaon final state, we observe from the *right* panel of Fig. 10, the mass of the di-kaon final state starts from $m_{K^+K^-} \gtrsim 1$ GeV. The major background events originating here come from D meson decays, populating the distribution below $m_{K^+K^-} \sim 1.87$ GeV. The resonance at 1.87 GeV corresponds to the mass of the D^0 meson. We find that the d_T values of the di-kaon final states are not as large as in the di-pion case, as we had already seen from the d_T distribution of charm mesons in Fig. 4. This implies that a d_T cut of 150 mm might get rid of all the SM backgrounds for the di-kaon final state. Again, the background populates the

$m_{K^+K^-K^\pm} \sim m_{B^\pm} = 5 \text{ GeV}$ region for the 1 GeV benchmark.

Until now, we have only considered the final states containing two pions and/or two kaons as SM backgrounds. However, we have to consider the possibility of a proton to fake as a π^+ or a K^+ . Protons can be produced from the decay of a Λ^0 baryon: $\Lambda^0 \rightarrow p^+\pi^-$. The misidentified protons coming from the Λ^0 decay are an important background since the Λ^0 baryon is long-lived, having d_T values beyond 1 m, similar to $K_{S/L}$ as shown in Fig. 4. It has a mass of 1.1 GeV, making it a major background for benchmarks such as BPA2 and BPA3, which have a mass of 1 GeV. Fig. 12 shows the distribution of the final state invariant mass and d_T , taking into account the events containing a proton too. Even if the excellent charge identification of the DCH achieves a proton rejection efficiency of 99.999%, we still have $\mathcal{O}(10^4)$ background events from the Λ^0 decay. Since this affects both the di-pion and di-kaon final states equally, we cannot simply use a large d_T cut even for the di-kaon signal.

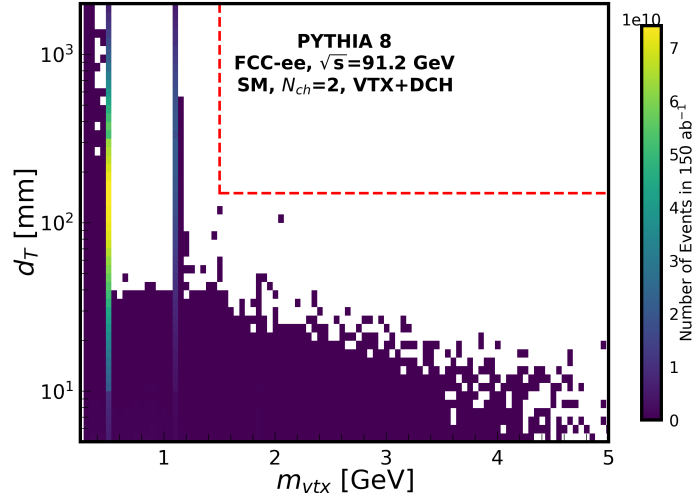


Figure 12: Invariant mass of the final state decay products with two charged particles that include pions, kaons, and protons, with respect to the d_T of the vertex for the SM background. The *red dashed lines* mark the region in the $m_{\text{vtx}} - d_T$ plane which is free from the SM background, motivating the cuts on these variables.

For the benchmarks BPA1, BPA2, and BPA3, if we were to use the variable $m_{\pi^+\pi^-/K^+K^-}$ for selecting the signal events, the analysis would entirely depend on the resolution of the reconstructed invariant mass of the final state decay products. Despite an excellent mass resolution, background statistics play a crucial role because the SM background populates this region even for large d_T . The overlap of the signal with $\mathcal{O}(10^{10})$ background events shall render it impossible to detect such LLPs. The possible strategy to search for these benchmarks is to carry out the analysis in the muon system. For the rest of the benchmarks, we apply a $d_T > 150 \text{ mm}$ cut on the backgrounds to reduce its contribution to zero. We tabulate the final cuts used for the analyses of benchmarks with $m_\phi \gtrsim 1.5 \text{ GeV}$ in the *left* column of Table 12. After

Final cuts for the di-pion/di-kaon final state	
$m_\phi \gtrsim 1.5 \text{ GeV}$	All benchmarks
$D_{\text{vtx}} \in \text{VTX or DCH}$	$D_{\text{vtx}} \in \text{MS}$
$N_{\text{ch}} = 2$	$N_{\text{ch}} = 2$
$N_{\pi/K} = 2$	$N_{\text{ch}} = 2$
$E > 1 \text{ GeV}$	$E > 5 \text{ GeV}$
$d_T > 150 \text{ mm}$	$E > 5 \text{ GeV}$

Table 12: Final selection cuts applied on the signal and SM background events when the final state contains two pions or two kaons.

applying these cuts, we show the number of signal events, both for $\phi \rightarrow \pi^+\pi^-$ and $\phi \rightarrow K^+K^-$ in Table 13.

Benchmarks	VTX + DCH analysis			
	$m_\phi \text{ (GeV)}$	$c\tau \text{ (mm)}$	Number of events	
			$\phi \rightarrow \pi^+\pi^-$	$\phi \rightarrow K^+K^-$
BPA4	2.0	135.2	26202	26970
BPA5	3.5	10385.4	4	2
BPA6	3.5	65.8	9495	3822

Table 13: Number of signal events in BPA4, BPA5, and BPA6 after a cut-based analysis in the vertex detector (VTX) and drift chamber (DCH). The number of background events in each case is null.

The benchmarks with $m_\phi \lesssim 1.5 \text{ GeV}$, like BPA1, BPA2, and BPA3, along with the other benchmarks, are then analyzed in the MS. The MS provides a relatively cleaner environment since all the long-lived hadrons and their decay products, apart from muons, deposit their energy in the calorimeter. We select events that contain one displaced vertex detected within the MS, with two charged particles, and $E > 5 \text{ GeV}$. We tabulate the cuts for the MS analysis in the *right* column of Table 12. Table 14 shows the number of signal events for all the benchmarks for the MS analysis. The di-pion and di-kaon final states are combined because pions and kaons might not be distinguished in the MS.

The background is reduced to zero in this case. We observe 4 events for BPA1 in the MS. Increasing the luminosity can help in observing more events for this benchmark. BPA2 and BPA3 are observed to have a sufficient number of events. BPA5, with a $c\tau$ of $\sim 10 \text{ m}$ is expected to have 4 observed events in the MS in addition to the 4 (2) events in the VTX+DCH analysis with pions (kaons) in the final state. The benchmark BPA6 is expected to have a significant number of events in the VTX+DCH analysis, while BPA4 has a good prospect with both the VTX+DCH and MS analyses.

Benchmarks	Muon Spectrometer analysis		
	m_ϕ (GeV)	$c\tau$ (mm)	Number of events
BPA1	0.4	39666.6	4
BPA2	1.0	554.3	206
BPA3	1.0	34.6	78
BPA4	2.0	135.2	1515
BPA5	3.5	10285.4	4
BPA6	3.5	65.8	3

Table 14: Number of signal events in benchmarks BPA1 to BPA6 after a cut-based analysis in the Muon System (MS). The number of background events in each case is null.

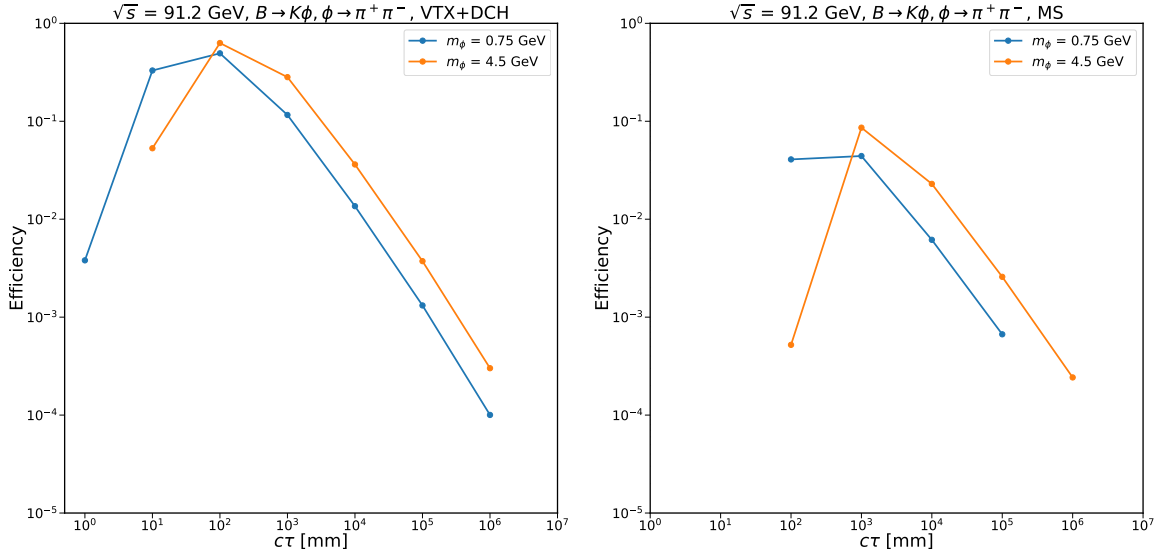


Figure 13: Efficiency for the di-pion decay mode of the LLP ϕ for varying decay lengths and masses. The generation of LLP involved the $Z \rightarrow b\bar{b}$ process where one B meson decays via BSM process $B \rightarrow K\phi$, and the other B decays to SM particles. The final state pions were detected with a cut: $d_T > 150$ mm within VTX and DCH (*left*), and in the muon system (MS) (*right*).

Using the two kinds of search techniques presented above, we perform the analysis beyond our chosen LLP benchmarks, assuming 100% decay to di-pion final states. The muon system analysis combines both di-pion and di-kaon events. The efficiencies of the VTX+DCH analysis and the MS analysis for the di-pion final state are presented in Fig. 13. The efficiencies of the di-kaon final state are similar to the di-pion efficiencies. The corresponding maps of efficiencies in the $c\tau - m_\phi$ plane are shown in Fig. 23 in Appendix A. For the VTX+DCH map, the masses 0.5 GeV and 1 GeV are difficult to search for amid the huge background of long-lived SM resonances in these regions. These can only be probed in the muon system.

4.4.3 Analysis in the $c\bar{c}$ Final State

One of our chosen benchmarks for **Case A**, BPA7, has a significant branching ratio to the $c\bar{c}$ final state. After the decay $\phi \rightarrow c\bar{c}$, the charm quarks hadronize to form mesons, particularly the D mesons: D^0, D^\pm . Because ϕ is long-lived, the D^0, D^\pm and particles formed after the hadronization are detected at a large d_T depending on the $c\tau$ of ϕ . The signature for this LLP benchmark is the presence of multiple displaced vertices and/or a large number of charged particles connected to a displaced vertex. The potential SM background consists of prompt bottom and charm production. The B hadrons lead to displaced vertices because of their long lifetimes. The D mesons produced from the decay of the B are thus displaced. Other long-lived mesons like K_S and K_L can also mimic the signal by decaying into multiple charged particles at large d_T . The SM particles produced from the hadronization of $b\bar{b}$ and $c\bar{c}$ states may also include some baryons, such as the Ξ, Σ , or Λ_c that have longer decay lengths, as discussed in Section 4.2.

Selection cuts to study the SM $c\bar{c}$ background
$D_{\text{vtx}} \in \text{VTX or DCH}$
$N_{\text{ch}} \geq 3$
$E > 5 \text{ GeV}$
$d_T > 5 \text{ mm}$

Table 15: Selection cuts applied to study the SM background for the $c\bar{c}$ final state.

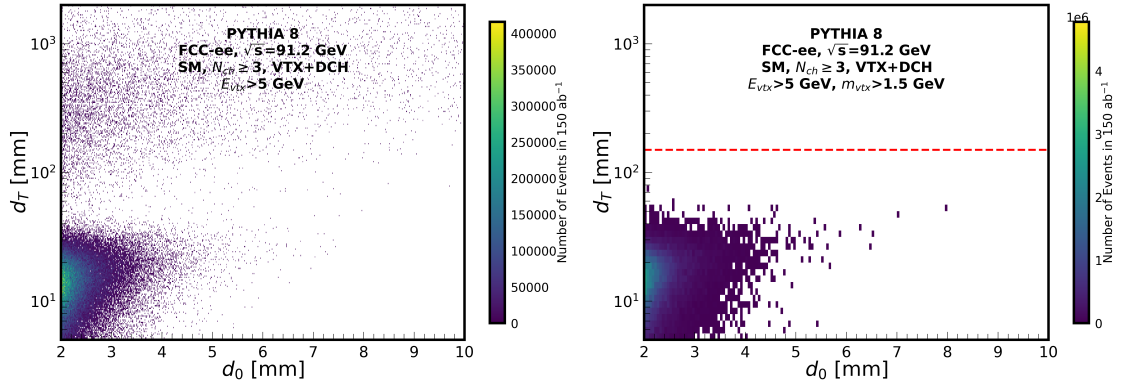


Figure 14: Distribution of the SM background events from Z production in the $d_0 - d_T$ plane before (*left*) and after (*right*) applying a cut on the invariant mass of the final state decay products. The *red dashed line* marks the d_T threshold which reduces the SM backgrounds.

Table 15 lists the selection cuts applied to study the background and design cuts to suppress the backgrounds completely. We require the vertex to have at least 3 outgoing charged particles. The total energy of the decay particles from a vertex

must be greater than 5 GeV, and d_T of the vertex must be at least 5 mm. After applying these selection cuts, we plot the distribution of the SM background events in the plane of d_T and the impact parameter, d_0 , in the *left* panel of Fig. 14. We observe numerous displaced vertices with d_T values as high as a few meters, with impact parameters extending beyond 10 mm.

Benchmark BPA7		m_ϕ (GeV)	$c\tau$ (mm)
		4.4	95.0
Final cuts for the $c\bar{c}$ final state		Number of events	
$D_{\text{vtx}} \in \text{VTX or DCH}$	} +	$d_T > 100 \text{ mm}, d_0 > 10 \text{ mm}$	6
$N_{\text{ch}} \geq 3, E > 5 \text{ GeV}$		$d_T > 150 \text{ mm}, d_0 > 10 \text{ mm}$	6
$m_{\text{vtx}} > 1.5 \text{ GeV}$		$d_T > 250 \text{ mm}, d_0 > 20 \text{ mm}$	3

Table 16: Number of signal events for BPA7, with $c\bar{c}$ final state, with cuts on d_T and d_0 , where the first set of cuts are applied in all three cases. The background is expected to be zero in each case.

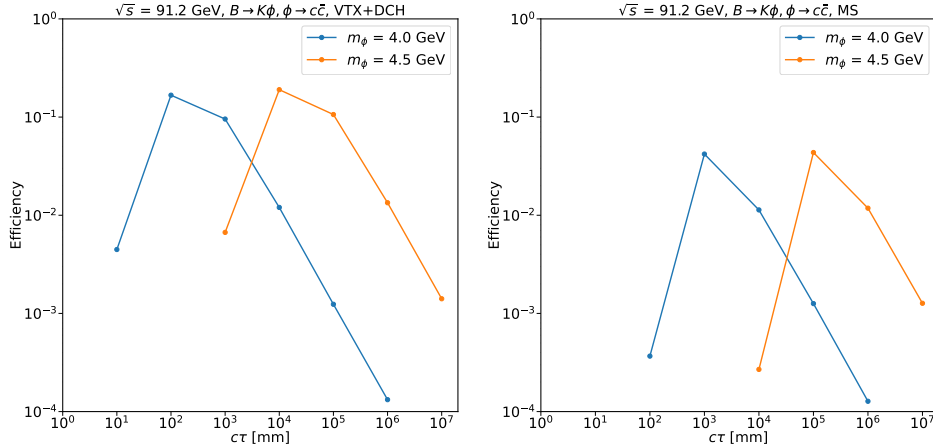


Figure 15: Efficiency for the $c\bar{c}$ decay mode of LLP ϕ for varying decay lengths and masses of ϕ . The generation of LLP involved the $Z \rightarrow b\bar{b}$ process where one B meson decays via BSM process $B \rightarrow K\phi$, and the other B decays to SM particles. The final state pions were detected with a cut: $d_T > 150 \text{ mm}$ within VTX and DCH (*left*), and in the Muon System (MS) (*right*).

If we apply a cut on the invariant mass of 1.5 GeV, the events with large d_0 and d_T are removed, rendering the background to be constrained to $d_T < 100 \text{ mm}$, as shown in the *right* panel of Fig. 14. This is because the cut removes the major source of displaced background, *i.e.*, long-lived baryons with mass $\lesssim 1.5 \text{ GeV}$ (*cf.* Table 7). We then apply several cuts on d_T and d_0 to extract signal events with zero background. The final set of cuts along with the results are presented in Table 16.

Note that we don't perform the MS-only analysis for this benchmark since the events have a negligible probability of reaching the MS, as shown in Table 4.

Similar to the previous analyses, we extend our analysis for LLPs decaying to $c\bar{c}$ for various decay lengths and masses. The efficiencies for two such mass points with varying decay lengths are shown in Fig. 15. The efficiencies for both the VTX+DCH analysis and the MS analysis are calculated over a range of mass and lifetime of ϕ . For the former, the signal events must have a minimum d_0 of 10 mm and a d_T of 150 mm. In the latter case, a sufficient condition is to detect displaced activities in the MS, with $N_{\text{ch}} \geq 3$ and $E > 5$ GeV.

4.4.4 Production via $Z \rightarrow Z^*\phi$

We mentioned the production of ϕ 's from Z boson decays in Section 2. The partial width of the process $Z \rightarrow Z^*\phi$ is suppressed by the square of the mixing angle. However, at the Z factory of FCC-ee, around 10^{12} Z bosons will be produced, and it might be possible to observe such rare decay modes. To study the prospect of this production mode for ϕ , we estimate the partial width of the Z boson for varying masses of ϕ assuming $\sin\theta = 1$ using `MadGraph5_aMC@NLO` [201]. We can then scale this partial decay width accordingly for any value of the mixing angle. From this, we find the branching fraction for $Z \rightarrow Z^*\phi$ and calculate the number of expected $e^+e^- \rightarrow Z^*\phi$ events at the FCC-ee running at the Z pole. In Fig. 16, we show the region of the $m_\phi - c\tau$ parameter space where we expect to have at least 10 or 100 $Z \rightarrow Z^*\phi$ events at the FCC-ee. We observe that most of this region has a prompt decay of ϕ , which requires a different analysis strategy.

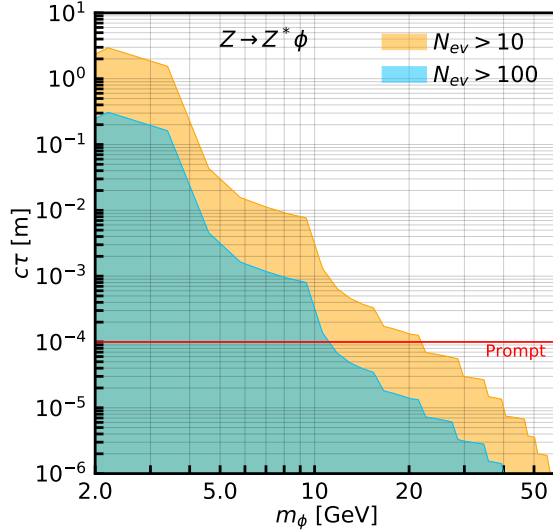


Figure 16: The dark Higgs boson mass versus decay length parameter space having at least 10 (*orange*) and 100 (*cyan*) $Z \rightarrow Z^*\phi$ events at the FCC-ee.

4.5 LLPs with large Trilinear Coupling

In this section, we study the prospects of discovering LLPs at FCC-ee that have a large trilinear coupling with the SM Higgs boson and, hence, are produced via the decay of the SM Higgs. The corresponding signal benchmarks are listed in Table 2. The FCC-ee is expected to operate as a Higgs factory at $\sqrt{s} = 240$ GeV. The planned integrated luminosity achieved during this run is $\mathcal{L} = 10.8 \text{ ab}^{-1}$. We simulate this using PYTHIA 8, and generate the signal via the associated production of the Higgs with a Z : $e^+e^- \rightarrow Zh$, $Z \rightarrow \text{incl.}$, and $h \rightarrow \phi\phi$. Depending on the benchmark properties, ϕ decays to SM particles with the branching ratios listed in Table 2. We observe that the benchmarks in this case have final states consisting of $\pi^+\pi^-$, K^+K^- , $c\bar{c}$, and $b\bar{b}$, depending on the mass of the LLP.

A similar study on LLPs originating from the decay of the SM Higgs was performed in Ref. [202]. The analysis investigated the process $e^+e^- \rightarrow Zh$, followed by $Z \rightarrow \ell^+\ell^-$ and $h \rightarrow ss$, where ℓ^\pm represents a charged lepton and s is a long-lived scalar decaying to $b\bar{b}$. In our study, we do not limit our analysis to the leptonic decay mode of the Z , but we consider its inclusive decay mode, owing to the small $Z \rightarrow \ell^+\ell^-$ branching ratio of $\sim 10\%$.

The backgrounds from the SM that mimic the signal are the processes $e^+e^- \rightarrow f\bar{f}$, $e^+e^- \rightarrow ZZ$, $e^+e^- \rightarrow Zh$, and $e^+e^- \rightarrow WW$ at $\sqrt{s} = 240$ GeV, where $f(\bar{f})$ denotes fermions (anti-fermions). Both hadronic and leptonic decay modes of the vector bosons are considered. Table 17 lists the cross-section of these processes and the total number of such events at $\sqrt{s} = 240$ GeV and $\mathcal{L} = 10.8 \text{ ab}^{-1}$. We generate 10^8 single $Z \rightarrow f\bar{f}$, 2×10^7 ZZ , 10^8 WW , and 2×10^7 Zh events. For the signal benchmarks, we simulate 20,000 events for the process Zh , $h \rightarrow \phi\phi$.

SM Backgrounds	Cross-section (pb)	Expected number of events
$e^+e^- \rightarrow f\bar{f}$	21.43	2.3×10^8
$e^+e^- \rightarrow W^+W^-$	16.84	1.8×10^8
$e^+e^- \rightarrow ZZ$	1.4	1.5×10^7
$e^+e^- \rightarrow Zh$	0.237	2.5×10^6

Table 17: SM backgrounds for **Case B** with their cross-sections and expected number of events at $\sqrt{s} = 240$ GeV, $\mathcal{L} = 10.8 \text{ ab}^{-1}$.

4.5.1 Analysis in the Di-pion and Di-kaon Final States

Among the benchmarks listed in Table 2, both BPB1 and BPB2 decay into $\pi^+\pi^-$ and K^+K^- with equal branching ratios of 50% each. The strategy for selecting signal and rejecting background events involves identifying displaced charged pions and charged kaons within the detector and then reconstructing the LLPs and the Higgs boson.

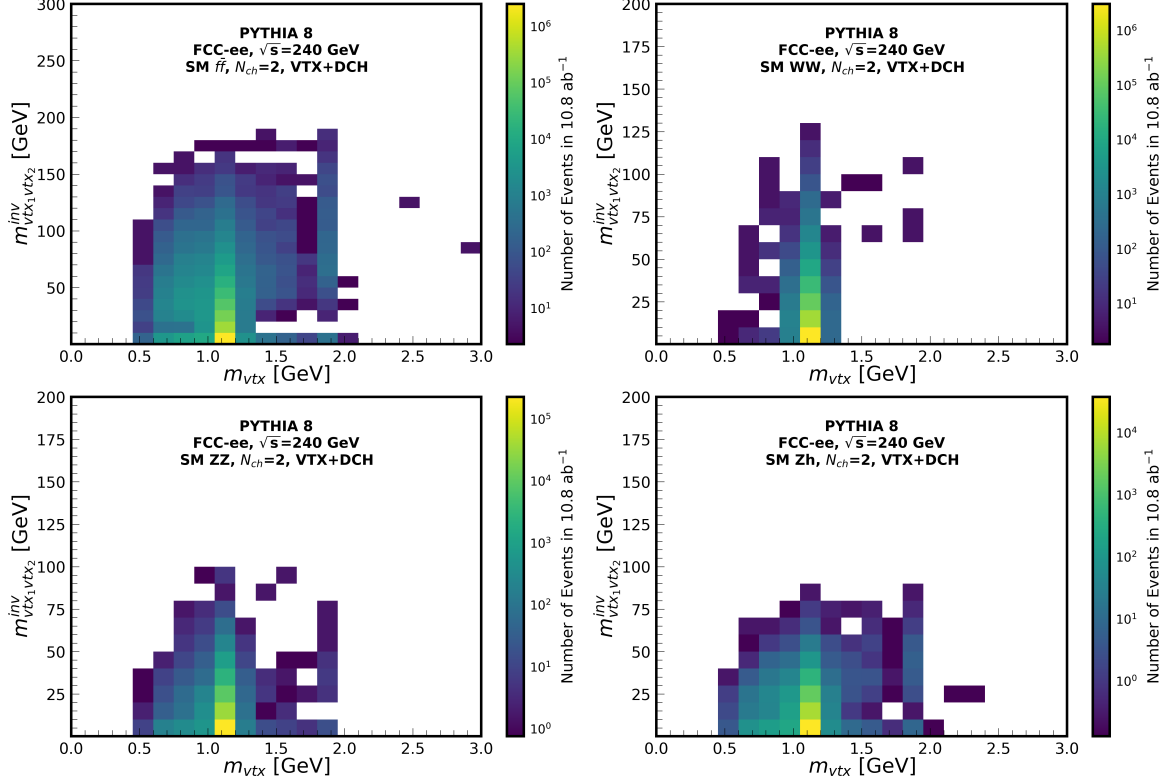


Figure 17: Distribution of the invariant mass of all the final state particles associated with a vertex with respect to the invariant mass of all the particles from two vertices in an event, for the four major backgrounds of the $e^+e^- \rightarrow Zh, h \rightarrow \phi\phi$ channel, namely (*top left to bottom right*) $f\bar{f}$, W^+W^- , ZZ , and Zh production, respectively.

We first define the cuts a vertex and the resulting decay products need to satisfy to be selected. The cuts are similar to those in the previous analyses. A vertex must be detected inside the VTX or DCH. The number of charged particles (N_{ch}) must be exactly equal to 2. The total energy of the decay particles from a vertex must be greater than 1 GeV, and the d_T of the vertex must be greater than 5 mm. If the above conditions are satisfied, we select the vertex. Now, there must be exactly two such vertices in the event. We compute the invariant mass of each of the decays vertices (m_{vtx1} , m_{vtx2}). For the LLP signal, since both the displaced vertices come from the decay of two identical LLPs (ϕ), we select events where the invariant masses of the two decay vertices do not differ by more than 100 MeV. Finally, we reduce the huge background coming from long-lived mesons and K_L/K_S decays by selecting the events with invariant mass above the kaon threshold (m_{vtx1} , m_{vtx2}) > 0.6 GeV. Table 18 summarizes all the selection cuts we apply to the events.

We reconstruct the Higgs boson by summing the four momenta of the final states of the two selected vertices. The invariant mass of the two should lie within a 3 GeV

Cuts on background in the di-pion and di-kaon final state	
$D_{\text{vtx}} \in \text{VTX or DCH}$	
$N_{\text{tot}} = 2, \quad N_{\text{ch}} = 2$	
$E > 1 \text{ GeV}, \quad d_T > 5 \text{ mm}$	
$N_{\text{vtx}} = 2, \quad m_{\text{vtx}_{1/2}} > 0.6 \text{ GeV}$	
$ m_{\text{vtx}_1} - m_{\text{vtx}_2} < 0.1 \text{ GeV}$	

Table 18: Selection cuts applied to the signal $e^+e^- \rightarrow Zh$, where $Z \rightarrow f\bar{f}$, and $h \rightarrow \phi\phi$ and the SM background when analysis is done in the $\pi^+\pi^-$ and K^+K^- final states.

mass window around the Higgs mass, *i.e.*, $122 \text{ GeV} < m_{\text{vtx}_1\text{vtx}_2}^{\text{inv}} < 128 \text{ GeV}$. The number of signal events for BPB1 and BPB2 and background events are listed in Table 19.

Benchmarks	m_ϕ (GeV)		$c\tau$ (mm)			
BPB1	1		10			
BPB2	1		100			
Cuts	Number of events					
	Signal		Backgrounds			
	BPB1	BPB2	$f\bar{f}$	WW	ZZ	Zh
$122 \text{ GeV} < m_{\text{vtx}_1\text{vtx}_2}^{\text{inv}} < 128 \text{ GeV}$	222	21	215	24	0	0
In each vertex, $N_p = 0$	222	21	125	4	0	0
In each vertex, $N_{\pi^\pm} = 2$ or $N_{K^\pm} = 2$	222	21	14	0	0	0
$d_T > 100 \text{ mm}$	143	18	0	0	0	0

Table 19: Number of signal and background events after applying the displayed cuts.

The backgrounds from $e^+e^- \rightarrow f\bar{f}$ and $e^+e^- \rightarrow W^+W^-$ are required to satisfy the Higgs mass criterion as well. The four panels in Fig. 17 show the distributions of the four types of background events in the $m_{\text{vtx}} - m_{\text{vtx}_1\text{vtx}_2}^{\text{inv}}$ plane, respectively. The SM $f\bar{f}$ background (*top left*) populates very high values of the invariant mass compared to the other three backgrounds. This is reflected in the results in Table 19 where the Z events easily satisfy the Higgs boson mass cut. The huge background at $m_{\text{vtx}} = 1 \text{ GeV}$ results from the formation of long-lived Λ baryons, which decay into a proton and a pion. To mitigate this effect, we apply an additional proton veto on the signal and backgrounds, $N_p = 0$. The background after the use of a proton veto reduces drastically.

Until now, we have required that there are exactly two charged particles emanating from the displaced vertex. We now explicitly specify that these two charged particles must be either a pair of pions ($\pi^+\pi^-$) or kaons (K^+K^-). This means that,

at a given vertex, $N_{\pi^\pm} = 2$ or $N_{K^\pm} = 2$. It is important to note that all of the aforementioned criteria heavily depend on the accurate identification of charged particles, particularly in correctly identifying and vetoing protons. As compared to the di-pion and di-kaon final states in **Case A**, the number of background events in this case is significantly smaller. As a result, the proton veto is expected to be efficient in reducing the SM background here. Additionally, the vertex must have a transverse displacement $d_T > 100$ mm. By applying these criteria, it is possible to achieve a zero-background scenario. BPB1 and BPB2 still have respectively 143 and 18 signal events to be observed.

4.5.2 Analysis in the $c\bar{c}$ and $b\bar{b}$ Final States

Benchmarks BPB3, BPB4, BPB5, and BPB6 decay to $c\bar{c}$ with 65%, 65%, 49%, and 49% branching fractions, respectively, while BPB6 and BPB7 decay dominantly to $b\bar{b}$. To select the signal events, we require a decay vertex to be detected in the VTX or the DCH, similar to the previous analyses. The vertex must involve more than two charged particles in the final state. The $c\bar{c}/b\bar{b}$ partons hadronize and therefore, the vertices from ϕ decays have multiple charged particles. Their total energy must be at least 5 GeV at a vertex. The displacement of such a vertex must be greater than 5 mm from the interaction point. Vertices satisfying all the above conditions are selected.

After applying these selection cuts on the vertices, we plot the distribution of the vertices from the background events in the m_{vtx} and d_0 plane. Fig. 18 shows the two-dimensional distribution of the SM backgrounds: $f\bar{f}$, WW , ZZ , and Zh . Since there are two LLPs, we demand that there must be exactly two such vertices in the event. Table 20 summarizes these selection cuts.

Cuts on background in the $c\bar{c}$ and $b\bar{b}$ final states
$D_{\text{vtx}} \in \text{VTX or DCH}$
$N_{\text{ch}} \geq 3$
$E > 5 \text{ GeV}$
$d_T > 5 \text{ mm}$
$N_{\text{vtx}} = 2$

Table 20: Selection cuts applied on the signal $e^+e^- \rightarrow Zh, Z \rightarrow \text{incl.}, h \rightarrow \phi\phi$ and the SM background when analysis is done in the $c\bar{c}$ and $b\bar{b}$ final states.

For events having two displaced vertices, we further suppress the backgrounds using two analysis methods, as described below.

1. *Criterion 1:* Require one of the two vertices in the event to satisfy a strict cut on m_{vtx} and d_0 :

$$m_{\text{vtx}} > 2 \text{ GeV}, d_0 > 5 \text{ mm} \quad (4.3)$$

2. *Criterion 2*: Require both the vertices in the event to satisfy a weaker cut on d_0 :

$$m_{\text{vtx}} > 2 \text{ GeV}, d_0 > 2 \text{ mm} \quad (4.4)$$

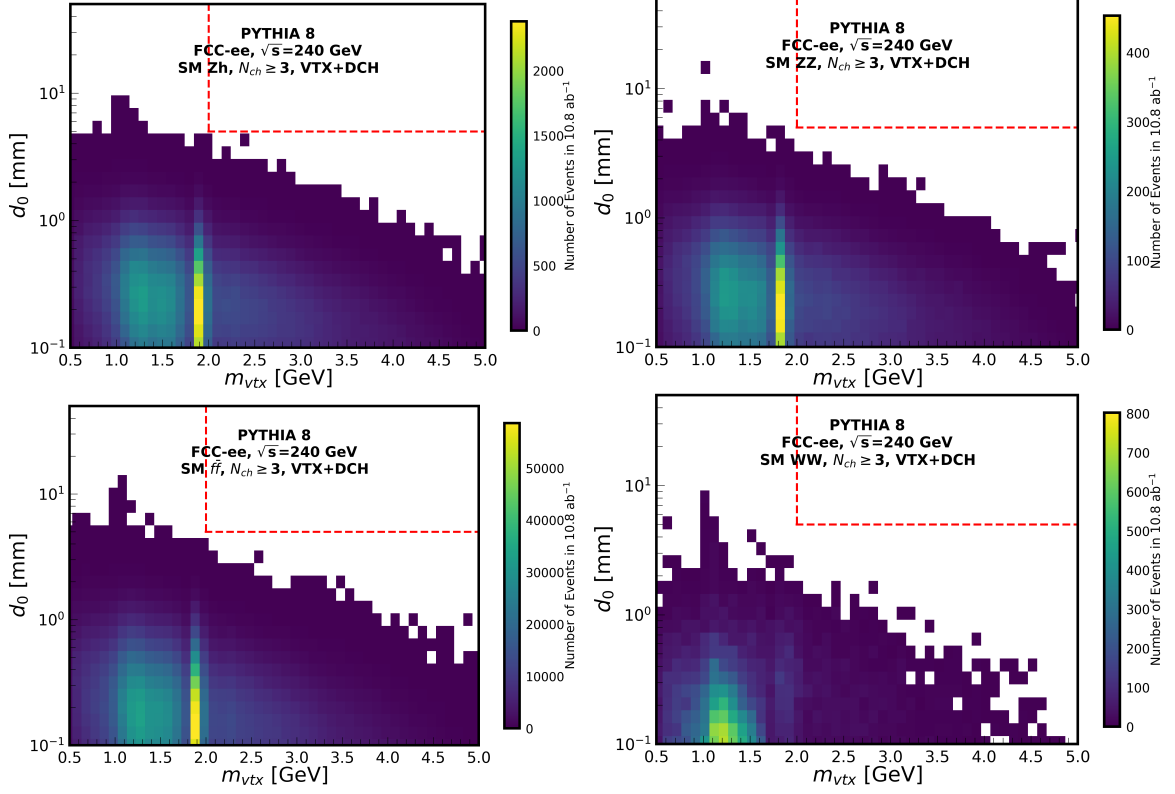


Figure 18: Distribution of the invariant mass of the particles associated with a decay vertex with respect to the impact parameter of the vertex, d_0 , for the four major backgrounds of the $e^+e^- \rightarrow Zh, h \rightarrow \phi\phi$ channel. The *red dashed lines* mark the region in the $m_{\text{vtx}} - d_0$ plane which is free from the SM background, motivating the cuts on these variables.

Both criteria result in a null background. This can be seen in Fig. 18. In the case of the background events, the final state particles from the vertices do not have an invariant mass above the $c\bar{c}$ threshold, and the d_0 of the vertices do not exceed 5 mm. There are events whose vertex has d_0 greater than 2 mm; however, no event has two such vertices. The number of signal events vary depending on the criteria. They are listed for each benchmark in Table 21. For BPB7 and BPB8, where the mass of the LLP is 40 GeV, the momentum boost for such a particle is less. Therefore, we observe that the number of displaced events increases for higher $c\tau$, as it helps the LLP satisfy the displacement criteria.

We note that for a lighter mass of the LLP, the higher $c\tau$ results in the loss of events because the search is in the VTX and/or DCH, so with a higher boost

Benchmarks	m_ϕ (GeV)	$c\tau$ (mm)	Number of signal events	
			<i>Criterion 1</i>	<i>Criterion 2</i>
BPB3	4.4	10	32	3
BPB4	4.4	100	8	1
BPB5	6.0	100	71	18
BPB6	6.0	1000	<1	~ 0
BPB7	40	10	562	320
BPB8	40	100	1747	887

Table 21: The number of signal events for each benchmark after applying the selection cuts of Table 20 and the cuts in *Criterion 1* and *Criterion 2*. The number of background events is zero in both cases.

and longer lifetime, the particles decay after passing the VTX/DCH and thus escape detection. BPB6, especially, has less than 1 remaining signal event. In that case, it shall be critical to search for events from such benchmarks in the muon spectrometer. An MS analysis would entail selection cuts similar to those listed in Table 20, except for the fact that the decay vertex is detected in the muon spectrometer ($D_{\text{vtx}} \in \text{MS}$) and $N_{\text{vtx}} \geq 1$. The last condition indicates that an event is selected even if only one of the two $c\bar{c}$ clusters is detected in the MS. With this analysis, we find that BPB6 results in 9 events, while the background remains zero. It is also important to note that the absence of any events in the VTX+DCH analysis for BPB6 is a direct consequence of the $N_{\text{vtx}} = 2$ condition. To demand that both of the light LLPs with decay lengths of 1 m decay within the VTX and DCH components is excessively restrictive. We weaken the N_{vtx} cut and instead impose stricter cuts on d_T and d_0 : $N_{\text{vtx}} \geq 1$, $d_T > 150$ mm, $d_0 > 10$ mm, $m_{\text{vtx}} > 2$ GeV. With these cuts, the VTX+DCH analysis yields 7 events for BPB6.

Figure 19 shows the signal efficiency for the two analyses: the VTX+DCH analysis and the MS analysis. Both use the same cuts on E and N_{ch} . We observe that the MS analysis can probe LLPs with much higher d_T .

Use of variable efficiencies

Our analyses involved the use of fixed efficiencies of the detector components. We now modify the efficiencies as a function of the radial distance from the IP of the detector component and the displacement d_T of the particles. The fixed values of efficiencies are listed in Table 6. For the VTX detector, the same efficiency is maintained throughout due to a large number of hits which improve the reconstruction. For the DCH, DRC, and MS, the efficiency values from Table 6 are multiplied by the function $(R_{\text{out}} - d_T)/(R_{\text{out}} - R_{\text{in}})$, where R_{in} and R_{out} are the inner and outer radius of the detector element, as listed in Table 3. Thus, when $d_T = R_{\text{in}}$ i.e., the decay

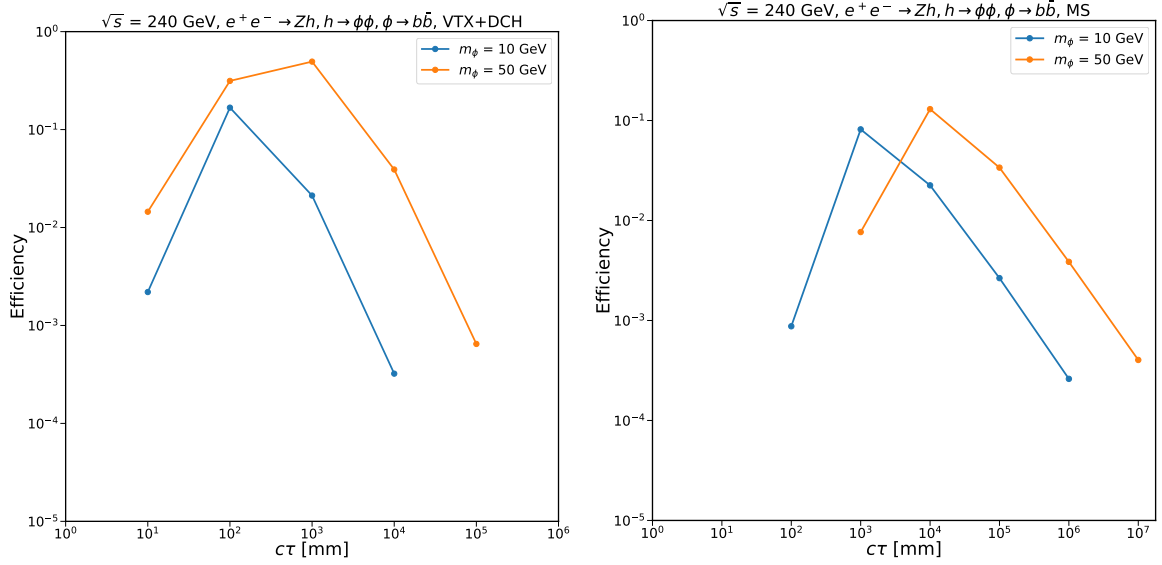


Figure 19: Efficiency plot of the $b\bar{b}$ decay mode of LLP ϕ , in the m_ϕ - $c\tau$ plane. The generation of LLP involved the $h \rightarrow \phi\phi$ process, where ϕ decays to $b\bar{b}$. The final state charged particles were detected within VTX and DCH (*left*), and in the Muon System (MS) (*right*).

particle is produced at the inner edge of the detector, the probability of the particle being detected is the maximum, and the probability falls as the particle traverses the length of the detector component, and becomes completely zero at the outer edge of the detector when $d_T = R_{out}$.

With this setup, the di-pion analysis of the BPA1 benchmark results in 2 events in the muon system. The signal efficiency for BPA2 in the MS analysis of di-pion and di-kaon final states drops from 6.4% to 4.1%. There is a 25% reduction in the signal efficiency for BPA3 in the MS analysis and a 20% reduction for BPA6 in the VTX+DCH analysis of the di-pion final state. For BPB1, we observed 143 events after the cut-based analysis. With the modified detector efficiencies, we now observe 80 events.

Our analyses for the displaced decays of the dark Higgs boson in the IDEA detector for both **Case A** and **Case B** show promising results for most benchmarks. However, there are still a few benchmarks, such as BPA1, BPA5, and BPB6, for which we expect very few events to be detected in the IDEA detector after applying cuts to reduce backgrounds. Additionally, if the detector efficiency of various components of the IDEA detector decreases linearly with increasing displacement of the decay, the expected signal yield will be affected, as discussed above. In such scenarios, dedicated LLP detectors surrounding the FCC-ee collider complex provide a complementary approach. In the next section, we propose various dedicated detector geometries and examine their sensitivity to the dark Higgs boson.

5 Dedicated Detectors at e^-e^+ Colliders

We have discussed the detection prospects of the LLPs coming from both B -mesons and Higgs boson decays at various parts of the proposed IDEA detector. However, for some of the benchmarks in both cases, most of the LLP decays escape the IDEA detector as seen from Tables 4 and 5. This happens mostly for lighter LLPs due to a higher Lorentz boost factor and/or LLPs having larger decay lengths. We find that benchmarks BPA1 and BPA5 from **Case A**, and BPB6 from **Case B** are expected to have less than 5 observable events after the analyses in the VTX+DCH or the MS of the IDEA detector. An additional approach for these benchmarks would be to employ dedicated LLP detectors positioned outside the main IDEA detector. There are already proposals of different dedicated detectors for lepton colliders, like the HERmetic Cavern TrackEr (HECATE) [140], near and far detectors [139, 141], and the LAYered CAvern Surface Tracker (LAYCAST) [144] for FCC-ee, ILC and CEPC, specifically designed to search for LLPs.

The authors of HECATE have proposed locating the detector along the inside of the cavern walls, forming a 4π detector. Using the example of heavy neutral leptons (HNL), they showed that such a detector would enhance the sensitivity to the squared mixing parameter by almost half an order of magnitude compared to the FCC-ee main detector. The far detectors proposed in Ref. [139] should study Higgs decays into a pair of long-lived light scalars at 240 GeV, as well as Z -boson decays into either a long-lived HNL and an active neutrino or a pair of long-lived neutralinos at the Z -pole. The sensitivity of this detector results in a modest improvement for LLPs with high decay lengths if its dimensions are as large as the MATHUSLA detector. The LAYCAST detector is proposed to be installed on the ceiling and the wall of the cavern of future electron-positron colliders such as CEPC and FCC-ee. This detector has a cuboid shape with a size of $40\text{ m} \times 20\text{ m} \times 30\text{ m}$, where three physics models are tested: $h \rightarrow \phi\phi$, HNLs, and neutralinos. Compared to the far detectors, LAYCAST is observed to have a better sensitivity for lighter LLPs with smaller $c\tau$ values, and larger LLP masses in the long-lifetime regime, being closer to the IP. For the HNL case, its sensitivity is similar to that of HECATE.

For the future colliders, the biggest advantage is the possibility of optimizing the position and configuration of the dedicated LLP detectors for maximizing the sensitivity to a particular model. We performed such an optimization for light long-lived dark Higgs bosons at the FCC-hh in order to propose transverse detectors, called DELIGHT [82], and forward detectors, FOREHUNT [88]. While optimizing the position of the transverse and forward detectors, we respectively considered the processes $h \rightarrow \phi\phi$ and $B \rightarrow X_s\phi$. In this section, we study various dedicated detector configurations for the FCC-ee to determine which configuration is feasible in size and optimized for detecting LLPs. These detectors should be capable of capturing LLPs originating from both B -meson decays and Higgs boson decays.

The geometry and placement of these detectors are chosen based on the production direction of the LLP being considered. Before going into detail about the geometry of the detector design, we first investigate the optimal placement of the detector. To get an idea of the directionality of the LLP, we plot the normalized θ (angle between the direction of the LLP with the z -axis, which is the beam axis) distribution for the LLP in Fig. 20. The *left* panel of Fig. 20 presents the θ distribution for LLPs with masses of 0.5 GeV and 4.0 GeV produced from B -meson decays. We observe that the LLPs can move in any direction from $[0, \pi]$ range, having a peak at $\frac{\pi}{4}$ and $\frac{3\pi}{4}$. The situation is different for the LLPs coming from the Higgs boson decay, as depicted in the *right* panel of Fig. 20, where most of the LLPs move centrally and peak at $\frac{\pi}{2}$ ¹⁰. This indicates that LLPs from Higgs decays are predominantly emitted perpendicular to the beam axis. By comparing the direction of the LLPs, we should keep in mind that our placement of the detector should maximize its coverage for both decay scenarios. We deduce that a detector covering the central η region between 0.5 and 2.5 would be optimal for both cases.

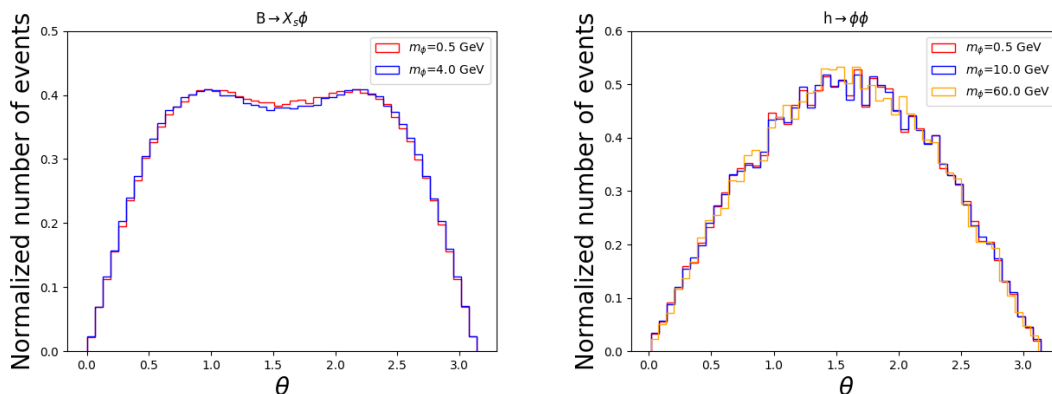


Figure 20: Normalized distributions of the polar angle (θ) of the LLPs coming from the decays of B -mesons (*left*) and the Higgs boson (*right*).

The final key consideration for the placement of the dedicated detectors is the design of the collider complex. The FCC-ee collider is planned to be designed as a quasi-circular tunnel with a circumference of 97.75 km and an internal diameter of 5.5 m [154]. The proposed tunnel layout includes approximately 8 km of bypass tunnels, 18 shafts, 12 large caverns, and 12 new surface sites. The colliding electron and positron beams of the FCC-ee cross at two IPs and large caverns are required to accommodate the experiments. Although the exact construction sequence for these caverns is yet to be confirmed, large-span caverns with dimensions of 66 m \times 35 m \times 35 m are proposed. A service cavern with a span of 25 m is required at each of the 12 access points around the ring. A service cavern at the machine level with dimensions

¹⁰Since the Higgs boson is produced primarily at rest and the decays are spherically isotropic, the distribution in the θ direction is proportional to $\sin \theta$.

of $100\text{ m} \times 25\text{ m} \times 15\text{ m}$ is needed near the experiment caverns. Shorter service caverns are planned at the remaining 10 access points, depending on the infrastructure equipment that needs to be housed underground. These caverns will be connected to the surface via shafts with diameters ranging from 10 m to 18 m. Each IP requires one shaft with a diameter of 15 m and one with a diameter of 10 m. Additionally, two shafts are proposed to be located near the existing CERN accelerators. The IDEA detector is designed to extend up to a half-length of approximately 6.5 m in the $\pm z$ -direction and 5.5 m in the radial direction inside the large experimental cavern.

Based on this discussion, we propose several detector designs optimized to capture LLPs originating from both B -meson and Higgs decays, as discussed below. The configurations of the dedicated detectors have been planned keeping in mind the sketch of the structure of the FCC-ee experimental cavern as shown in Fig. 7.5 of Ref. [154]. The detailed illustrations of these detectors are presented in Appendix B.

1. **A-TYPE:** This category of detectors consists of full- and half-cylindrical shells around the IDEA detector in the FCC-ee tunnel. There are six detectors in this category with varying inner radius, outer radius, and lengths. A1 is a full cylinder surrounding the IDEA detector, covering the 4π solid angle, and A2, A3, A4, A5, and A6 are half cylinders that surround the $0 < \theta < \pi$ region, where θ is the angle between the radius vector and the X -axis. The half-cylinders are proposed to accommodate the constraints in the experimental cavern in the case that the bottom half of the IDEA detector is inaccessible for a fully cylindrical structure. Fig. 25 shows the different configurations of detectors in this series. Table 23 shows the values of the parameters R_1 , R_2 , and L .
2. **B-TYPE:** This category consists of half-cylindrical shells like the A-type detectors; however, this time, the cylindrical shells are tilted at an angle of 45° in the $X-Y$ plane. We choose this configuration for the possibility that the IDEA detector is positioned in the FCC-ee experiment cavern such that the left wall and the floor are obstructed. There are five detectors in this category- B1, B2, B3, B4, and B5. B5 is a detector with similar coverage but of a different configuration. B5 is a combination of two box-shaped detectors of length L placed at right angles. The detectors are illustrated in Fig. 26, and the parameters of B1-B5 are listed in Table 24.
3. **C-TYPE:** At the time of the FCC-ee run, the space in the cavern for FCC-hh could be utilized to place dedicated detectors for LLPs. In such a scenario, we propose the C-type detectors, which are to be placed in the FCC-hh tunnel at 10 m from the IDEA detector. In this category, C1, C2, C3 are solid half-cylinders with $-\pi/2 < \theta < \pi/2$ and varying L . C4, C5, and C6 are box-shaped detectors of different dimensions parallel to the IDEA detector. C7 and C8 consist of

multiple boxes along the Z -axis, parallel to the IDEA detector, and in the FCC-hh tunnel. Fig. 27 and the parameters in Tables 25 and 26 highlight the different types of detectors in the C-series.

4. **D-TYPE:** The service cavern is 50 m away from the FCC-ee experiment cavern. LLPs with large decay lengths can traverse these distances, making the service cavern a suitable location to place dedicated LLP detectors. The service cavern is 100 to 150 m long, 15 m high, 25 m wide. The D-type detectors are to be placed in this location, at 80 m away from the IDEA detector. Six detectors are considered in this series, two of which are cylinders, and four are box-shaped detectors, as shown in Fig. 28. Table 27 lists the various parameters used to design the D-type detectors.
5. **E-TYPE:** We propose forward detectors for FCC-ee in this category. The E-type detectors are cylindrical shells placed along the Z -axis in the forward direction of the IDEA detector. There are ten detectors of this type, with varying radii, lengths, and distances from the IDEA detector. Out of these, E5 and E6 consist of forward detectors placed on both sides of the IDEA detector. Fig. 29 shows the configuration of six E-type detectors. Table 28 consists of the values of the radii and position for the six different types.
6. **F-TYPE:** FORward Experiment for HUNdred TeV (FOREHUNT) [88] was proposed as a forward detector for FCC-hh for the detection of light LLPs produced from the decay of B mesons and Higgs bosons at FCC-hh. They can also be utilized as detectors for LLPs produced in the FCC-ee. If a dedicated detector were to serve the purpose of both the experiments at FCC-ee and FCC-hh, it would be a cost-effective solution, too. They comprise the F-type detectors in our study. The radius and position of the detectors are varied, as illustrated in Fig. 30 and in Table 29.
7. **G-TYPE:** Similar to FOREHUNT, another category of dedicated detectors, DELIGHT, specific to the FCC-hh experiment, was proposed in [82]. However, in contrast to FOREHUNT, these are to be placed in the transverse direction to FCC-hh, as shown in Fig. 31. In our study, we consider the DELIGHT detectors, rotated azimuthally, to be the G-type detectors to see if they are sensitive to LLPs produced at FCC-ee. As mentioned, we aim for an optimum design that is equally sensitive to the two experiments so that the dedicated detector can be reused for the FCC-hh run. Three configurations of DELIGHT were explored in Ref. [82] – DELIGHT (A), DELIGHT (B), and DELIGHT (C). Here, we rename them G1, G2, and G3. We also consider some additional dimensions and placement positions. In total, there are nine configurations of G-type detectors, as listed in Table 30.

8. **H-TYPE:** A combination of near and far detectors shall capture LLPs of both smaller and larger decay lengths. Considering this, we design two cylindrical arcs (a quarter of a cylinder), one near the IDEA detector and one far from the IDEA detector. These have radii R_1 , R_2 and R'_1 , R'_2 . They possess the same length. We consider two configurations of this type. They are described in Fig. 32 and Table 31.
9. **I-TYPE:** The simplest detector design is that of a box. Until now, we have considered many box-shaped detectors placed in various locations away from the IDEA detector. We propose placing such box-shaped detectors directly above the IDEA detector as shown in Fig. 33. There are six I-type detectors with different elevations along the Y -axis, according to the dimensions parametrized by the values in Table 32.

For each dedicated detector, we scan over the $m_{c\tau} - m_\phi$ plane of LLPs coming from the $B \rightarrow K\phi$ process (**Case A**) and the $h \rightarrow \phi\phi$ process (**Case B**). We calculate the signal efficiencies for each point in the parameter space. The results are shown in terms of efficiency maps in Appendices C and D. We present the observations in each category of dedicated detectors for **Case A** and **Case B**.

In **Case A**, among the A-type detectors, A1 is the most sensitive, even for $c\tau = 10^9$ mm and $m_\phi \geq 2$ GeV. However, the configuration for A1 is that of a cylindrical shell that completely surrounds the IDEA detector. If it is unfeasible to construct such a detector due to space constraints, we also consider half-cylinders. The tilted designs of the B-type are more likely to fit the space. B4 shows the best performance among the B-type detectors. The ratio of the decay volumes of A1 and B4 is exactly 0.5, and so is the ratio of the efficiencies of the two.

The C and the D-type detectors are placed in the FCC-hh tunnel and the service cavern, respectively. LLPs from $B \rightarrow K\phi$ do not possess enough boost to reach these detectors, especially the D-type detectors; hence, they are less efficient. Even the LLPs with large $c\tau$ are not detected in these because of the lack of coverage in solid angle. Moreover, the branching fraction of $B \rightarrow K\phi$ is inversely proportional to the mixing angle. Therefore, for larger decay lengths, the production rate of ϕ decreases, reducing the sensitivity of dedicated detectors. While for smaller decay lengths, even when the branching fraction of B -mesons decaying to ϕ increases, the LLPs do not reach the dedicated detectors. Although C2 is a half-cylinder and C5 is a box, they have similar decay volumes (3140 and 3000 m³, respectively), and they are comparable in terms of efficiencies.

Among the E-type detectors, E5, which is symmetrically placed on either side of the IDEA detector in the forward direction, has the highest sensitivity. The FORE-HUNT detectors, named F-type detectors here, again lose much of the sensitivity for LLPs from $B \rightarrow K\phi$. The DELIGHT B configuration we proposed for FCC-hh, denoted as the G2 detector here, is the most sensitive to LLPs with high decay

lengths out of all the detector types considered here. We re-emphasize that the most optimum detector choice would be the one sensitive to LLPs from both FCC-ee and a future FCC-hh run. Among the I-type detectors, I4 is the most sensitive for **Case A**.

In **Case B**, the LLPs receive a boost from the decay of the SM Higgs and can traverse up to large distances before decaying. Additionally, the $\text{Br}(h \rightarrow \phi\phi)$ is independent of the mixing angle. Therefore, even for larger decay lengths, the production rate of ϕ doesn't decrease. This makes the dedicated detectors sensitive to LLPs with large $c\tau$'s in this scenario, which was not obtained in **Case A**. For instance, the C, D, and F-type detectors, which were not very efficient for LLPs produced in **Case A**, gain sensitivity for **Case B**.

We have observed that out of all the dedicated detectors, A1, B4, and G2 are the most sensitive to LLPs with high decay lengths. A1 is advantageous because of its excellent coverage, while G2 benefits from a high decay volume of $100 \times 100 \times 100 \text{ m}^3$. If the A1 detector cannot be constructed due to space constraints, the B4 configuration should be considered for a cylindrical geometry but with half the coverage of A1. For the benchmarks with high values of $c\tau$, we calculate the number of LLPs detected in A1, B4, and G2. The results are shown in Table 22. For BPA1, 38 events can be observed at A1, 21 events can be observed at B4, and 87 events can be observed at G2. We recall from Table 4 that with a 100% detector acceptance, only 22 events were detected in VTX and DCH combined, while 13 events were detected in the MS. The G2 detector provides significant improvement in this situation. Similarly, in BPA5, the number of events detected within the IDEA detector was low (5 in MS, 8 in VTX+DCH), while the dedicated detector G2 can detect 15 events. BPB6, having a decay length of 1 m, is observed best at A1. Of the 403 events decaying outside the detector (see Table 5), 153 events can be observed at A1. Detectors B4 and G2 can also improve the sensitivity to this benchmark as compared to the analyses performed for decays within the IDEA detector.

Benchmarks	Dedicated detector analysis				
	m_ϕ (GeV)	$c\tau$ (mm)	A1	B4	G2
BPA1	0.4	39666.6	38	21	87
BPA5	3.5	10285.4	11	6	15
BPB6	6.0	1000	153	83	14

Table 22: Number of events detected in A1, B4, and G2 detectors assuming 100% efficiency for our chosen benchmark points from **Case A** and **Case B**.

To study the sensitivity of the dedicated detectors across low to high lifetimes, we vary the decay length of two LLPs of masses 0.3 GeV and 4.0 GeV generated via $B \rightarrow K\phi$, and two LLPs of masses 1.0 GeV and 40 GeV generated via $Zh, h \rightarrow \phi\phi$ process. Figure 21 shows the efficiencies of these detectors for two different masses of

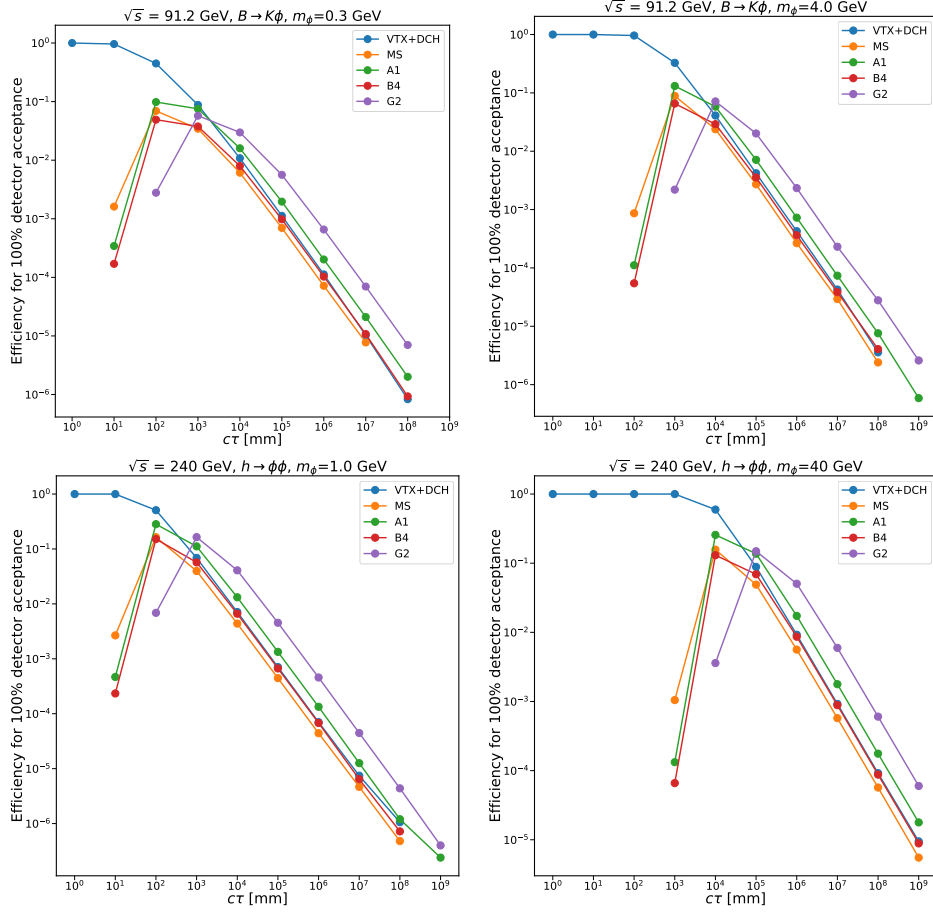


Figure 21: Efficiencies of the VTX+DCH systems, the Muon System (MS) and dedicated detectors A1, B4, and G2 plotted as a function of $c\tau$ for different masses of LLP in **Case A** scenario (*top panel*) and in **Case B** scenario (*bottom panel*).

LLPs as a function of $c\tau$ for $B \rightarrow K\phi$ and $h \rightarrow \phi\phi$ events, respectively. Also shown are the efficiencies obtained in VTX+DCH and Muon Systems of the IDEA detector. In **Case A**, the detectors A1 and G2 show higher efficiency than the VTX+DCH and MS components when the decay length is $\sim 10^4$ mm. The efficiency of B4 is comparable to that of VTX and DCH combined. For a 0.4 (4.4) GeV LLP, the efficiency of the A1 detector is 3 (2.5) times greater than that of the MS at a $c\tau$ of 10^6 mm, while the G2 detector reaches up to an efficiency 10 times that of MS for $c\tau$ of 10^8 mm. Improvement in the efficiency by a factor of 10 is also obtained for the G2 detector in the $h \rightarrow \phi\phi$ scenario.

As discussed, the DELIGHT B configuration (G2 detector) benefits from its high decay volume. Compared with all the other box-shaped detectors used in this study, it is the only one that achieves a tenfold improvement in efficiency over the IDEA detector. The substantial enhancement points us towards the need for a large detector volume to capture LLPs. Therefore, if a dedicated detector is to be

constructed for LLP detection at FCC-ee, its advantage would be maximized only if it is designed with a sufficiently large size, similar to DELIGHT B.

6 Summary and Conclusions

In the diverse landscape of current experiments and future proposals aimed at searching for light new physics, understanding the role of next-generation colliders is crucial. The most likely candidate is an electron-positron machine. Among the many options available, we focus here on the FCC-ee. However, the characteristics of these colliders are similar, so our discussion applies to all of them. To assess the potential of the FCC-ee for detecting light, long-lived BSM particles, the first question to address is: *Will ongoing experiments, along with existing proposals for beam dump or dedicated LLP detectors, leave any regions that can still be probed by the FCC-ee?* The answer to this question will also depend on how many of the proposed experiments receive approval. Even if one or more of the beam dump, collider, or dedicated LLP detectors observes a signal in the near future, *can the FCC-ee contribute to model identification and the determination of BSM particle properties?*

To illustrate these issues, we consider the dark Higgs model as an example. The dark Higgs boson, ϕ , is long-lived and can be produced either from B -meson decays or Higgs boson decays at the FCC-ee. Since the LLP in this model decays to SM particles via its mixing with the SM Higgs boson, there is a wide variety of decay modes depending on the mass of the mediator. The excellent particle identification capabilities of the FCC-ee detectors can provide sensitivity to decay modes involving mesons, and this can in turn help in the determination of various branching fractions of ϕ , in case of discovery. In the present work, we select benchmarks that span various possibilities and explore the questions discussed above. We divide the benchmarks into two cases – without and with a large trilinear scalar coupling. While $B \rightarrow K\phi$ is the dominant production mode in the first case, in the case of large trilinear coupling, $h \rightarrow \phi\phi$ is the dominant production mode. We study the benchmarks from the first case at the $\sqrt{s} = 91.2$ GeV run of FCC-ee, and the second case at the HZ production peak of $\sqrt{s} = 240$ GeV. For each benchmark, we perform analyses based on the detector element where the LLP decays and the final state it decays into. We also discuss briefly the mass and lifetime range that might be explored in the production of ϕ from the process $Z \rightarrow Z^*\phi$ at the FCC-ee.

We note that the primary background for light long-lived particles consists of SM long-lived hadrons. A comprehensive list of these hadrons, detailing their decay lengths and modes, shows that many of them significantly affect the analysis of some of our benchmark points due to the high production rates of the SM backgrounds. For example, the presence of K_S , K_L , and Λ^0 are major challenges in the search for LLPs below a mass of 1 GeV decaying to pions or kaons within the VTX or the DCH detectors. The muon spectrometer provides a much cleaner environment and, hence,

a better prospect for these LLP benchmarks. The d_T cut in our analysis is motivated by extrapolating the tails of the d_T distributions of hadrons having decay lengths in the intermediate range of $0.123 - 0.49$ mm, to identify the d_T threshold that eliminates the SM backgrounds. We quote the expected number of signal events at FCC-ee after the analysis cuts for each benchmark for their dominant decay modes. For the case where the LLP comes from the Higgs boson decay, we do not use any specific cut on the decay products of the associated Z boson. Instead, our analysis strategy demands the observation of both the LLP decay vertices to reduce the SM backgrounds. A similar analysis can be performed for other production modes of the Higgs boson, like the vector boson fusion process at higher energies of e^+e^- machines.

Finally, we extensively study possible dedicated LLP detector options for the FCC-ee. We consider nine different types of detector configurations with varying dimensions and positions around the FCC-ee collider complex. For LLPs coming from B -meson decays, the sensitivity is limited due to the dependence of the branching fraction on the mixing angle, unlike LLPs coming from the Higgs boson decay. We observe that the detector configurations A1, B4 and G2 perform the best among the dedicated detectors we considered. The detector configuration G2 is the DELIGHT B configuration that we proposed for FCC-hh in Ref. [82], just rotated in the azimuthal direction. We have observed in Refs. [82, 88] that the DELIGHT B detector configuration performs well for LLPs produced at the FCC-hh. Therefore, this can serve as a shared detector concept for both FCC-ee and FCC-hh.

We now discuss a summary of our benchmark study. In the case of negligible trilinear coupling, our study finds that FCC-ee can probe benchmarks BPA3 and BPA7, beyond the projected sensitivity of any existing proposed experiments. This is achieved with the pion/kaon MS only analysis and the $c\bar{c}$ analysis in the VTX+DCH detectors, respectively, for BPA3 and BPA7. For benchmarks BPA2, BPA4, and BPA6, where FASER2, LHCb, and SHiP experiments have some sensitivity, FCC-ee is expected to provide additional prospects. While for BPA2, we expect around 200 signal events in the MS with zero backgrounds with our analysis, for BPA4 and BPA6, we expect to observe $\mathcal{O}(10000)$ ($\mathcal{O}(1000)$) signal events after the VTX+DCH (MS only) analysis. This would help in the identification of the model and estimation of the model parameters even when we observe a signal in the previous experiments, like SHiP. Benchmarks BPA1 and BPA5 have large decay lengths and, therefore, are best observed in our proposed dedicated detectors around the FCC-ee interaction point, followed by the muon spectrometer of the IDEA detector.

In the case of large trilinear coupling, we expect to observe at least ~ 100 and ~ 10 signal events, respectively, for benchmarks BPB1 and BPB2 in the pion/kaon decay modes within the VTX and DCH detectors. For the rest of the benchmarks except BPB6, the VTX+DCH analysis yields around 10-1000 signal events, depending on the benchmark, when the backgrounds are suppressed to zero. Our proposed dedicated detectors A1 and B4 for FCC-ee perform the best for BPB6. We also

provide the efficiencies for each of our analyses with varying mass and decay length of the LLP for any non-minimal extension of this model, where the relation between mass and $\sin^2 \theta \times c\tau$ gets modified as compared to the minimal model. These efficiencies are also useful for translating the results for arbitrary branching fractions for the various decay modes of ϕ , given there is a theory uncertainty on this for ϕ having masses between $\sim 1 - 4$ GeV. In conclusion, our study highlights the importance of future lepton colliders in enhancing the search for light long-lived particles.

Acknowledgement

BB acknowledges the MATRICS Grant (MTR/2022/000264) of the Science and Engineering Research Board (SERB), Government of India. The work of BB is also supported by the Core Research Grant CRG/2022/001922 of the Science and Engineering Research Board (SERB), Government of India. BB and CB are grateful to the Center for High Energy Physics, Indian Institute of Science, for the cluster facility. HKD would like to thank the Nikhef Theory Group for its kind hospitality while part of this work was being completed. The work of NG was supported by the Japan Society for the Promotion of Science(JSPS) as a part of the JSPS Postdoctoral Program (Standard), grant number: JP24KF0189, and by the World Premier International Research Center Initiative (WPI), MEXT, Japan (Kavli IPMU). NG would also like to thank CHEP, IISC for financial support where part of the work was done. SM is supported by a Grant-in-Aid for Scientific Research from the Ministry of Education, Culture, Sports, Science, and Technology (MEXT), Japan: 23K20232 (20H01895), 24H00244 (20H00153), and 24H02244 by the JSPS Core-to-Core Program: JPJSCCA20200002 and by the World Premier International Research Center Initiative (WPI), MEXT, Japan (Kavli IPMU).

A Efficiency Maps of Model-independent Analyses

In this appendix we present example efficiency maps for the scenarios considered in this paper.

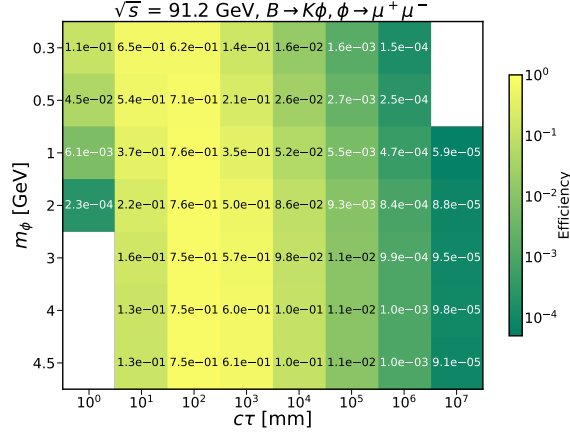


Figure 22: Efficiency map of the di-muon decay mode of the LLP ϕ , in the $c\tau$ - m_ϕ plane. The LLPs are produced via the $Z \rightarrow b\bar{b}$ process where one B meson decays via $B \rightarrow K\phi$, and the other B decays to SM particles. The final state muons were required to originate from a vertex which satisfies the cut: $150 \text{ mm} < d_T < 5500 \text{ mm}$.

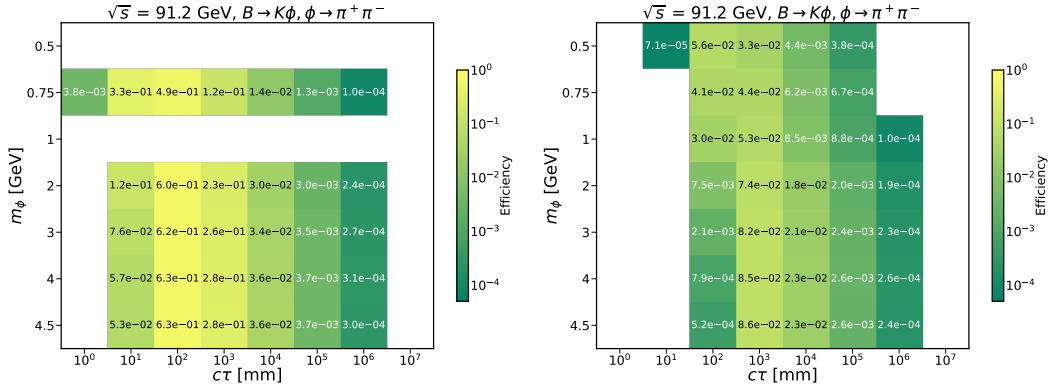


Figure 23: Efficiency map for the di-pion decay mode of the LLP ϕ , in the m_ϕ - $c\tau$ plane. The LLPs are produced via the $Z \rightarrow b\bar{b}$ process where one B meson decays via $B \rightarrow K\phi$, and the other B decays to SM particles. The final state pions were detected with a cut on the decay vertex where they originate: $d_T > 150 \text{ mm}$ within VTX and DCH (*left*), and in the Muon System (MS) (*right*). The $m_\phi = 0.5 \text{ GeV}$ and 1.0 GeV regions are masked because of the huge background in the VTX and DCH. They can be probed only through the MS analysis.

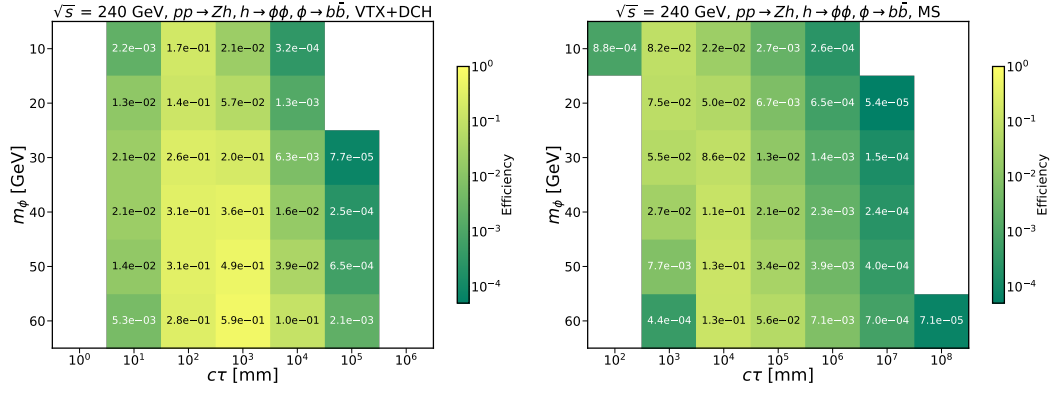
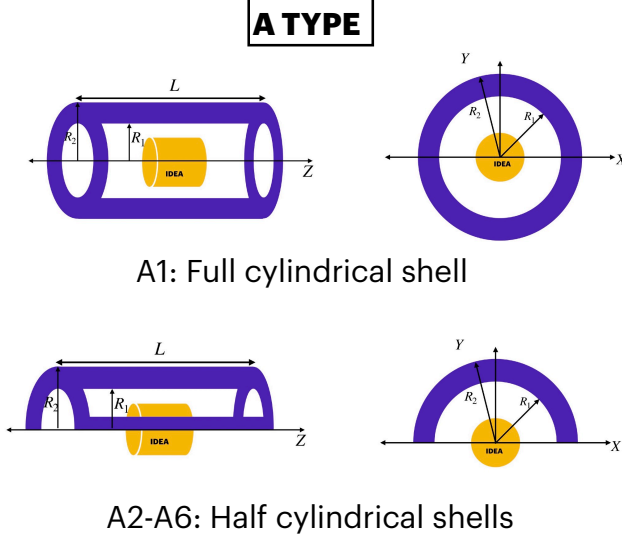


Figure 24: Efficiency map of the $b\bar{b}$ decay mode of LLP ϕ , in the m_ϕ - $c\tau$ plane. The LLPs are produced via the $h \rightarrow \phi\phi$ process, where ϕ decays to $b\bar{b}$. The final state charged particles were detected within VTX and DCH (*left*), and in the Muon System (MS) (*right*).

B Configurations of dedicated detectors

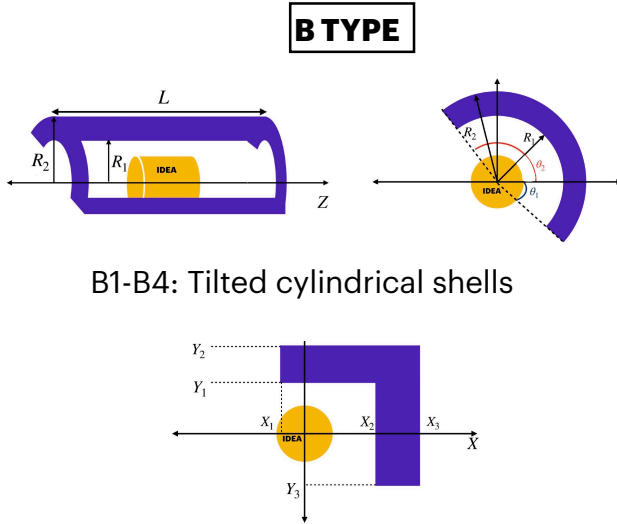
In this section, we present the illustrations of the different dedicated detectors proposed in this study, in Section 5. The detectors are categorized into various types. The figures show the model of each type of detector, and the tables list the various parameters of the dedicated detectors.



Detector	R_1 (m)	R_2 (m)	L (m)
A1	6	11	20
A2	6	11	10
A3	7	10	10
A4	9	10	10
A5	9	10	6
A6	7	10	6

Table 23: “A” series detectors – parameters

Figure 25: “A” series detectors – illustration



Detector	R_1 (m)	R_2 (m)	L (m)	θ_1 (°)	θ_2 (°)
B1	9	10	6		
B2	7	10	12		
B3	6	11	12	-45	135
B4	6	11	20		

B5: $X_1 = -3$ m, $X_2 = 7$ m, $X_3 = 12$ m,
 $Y_1 = 6$ m, $Y_2 = 11$ m, $Y_3 = -6$ m,
 $L = 20$ m

L - length of the detector along Z axis

Figure 26: “B” series detectors – illustration

Table 24: “B” series detectors – parameters

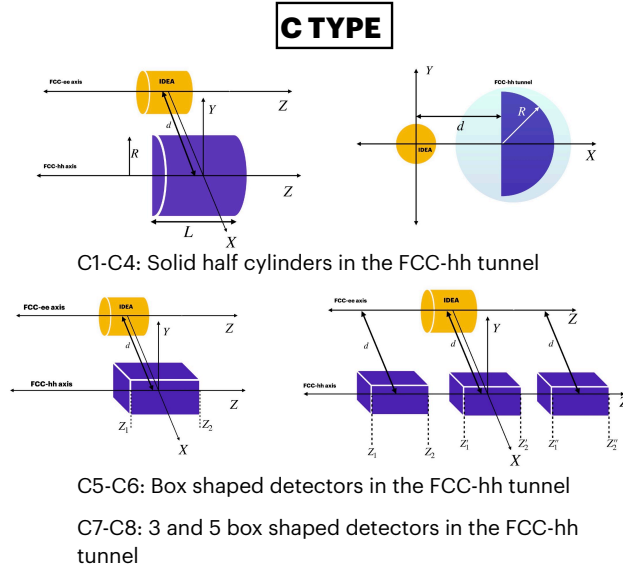


Figure 27: “C” series detectors – illustration

Detector	d (m)	R (m)	L (m)
C1	10	10	10
C2	10	10	20
C3	12	5	20
C4	12	5	10

C5 (C6): $X_1 = 10$ m, $X_2 = 20(15)$ m,
 $Y_1 = -5$ m, $Y_2 = 10(5)$ m,
 $Z_1 = -10(-5)$ m,
 $Z_2 = 10(5)$ m, $d = 10$ m

Table 25: “C” series detectors – parameters

Detector	d (m)	X_1 (m)	X_2 (m)	Y_1 (m)	Y_2 (m)	Z_1 (m)	Z_2 (m)	Z'_1 (m)	Z'_2 (m)	Z''_1 (m)	Z''_2 (m)	Z'''_1 (m)	Z'''_2 (m)	Z''''_1 (m)	Z''''_2 (m)
C7	10	10	15	-5	5	-15	-10	-5	5	10	15	—	—	—	—
C8	10	10	15	-5	5	-25	-20	-15	-10	-5	5	10	15	20	25

Table 26: “C” series detectors – parameters (contd.)

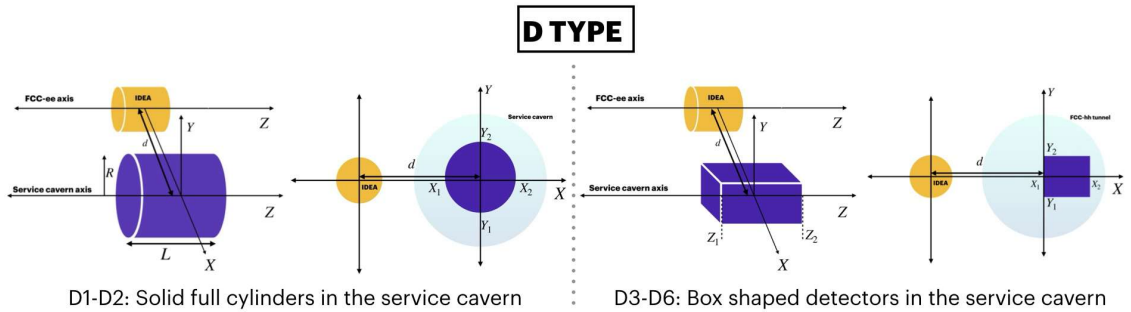


Figure 28: “D” series detectors – illustration

Detector	d (m)	R (m)	L (m)
D1	80	10	20
D2	80	5	10

Detector	d (m)	X_1 (m)	X_2 (m)	Y_1 (m)	Y_2 (m)	Z_1 (m)	Z_2 (m)
D3	80	80	85	-5	5	-5	5
D4		80	85	-5	5	-10	10
D5		80	85	-5	5	-15	15
D6		80	90	-5	10	-15	15

Table 27: “D” series detectors – parameters

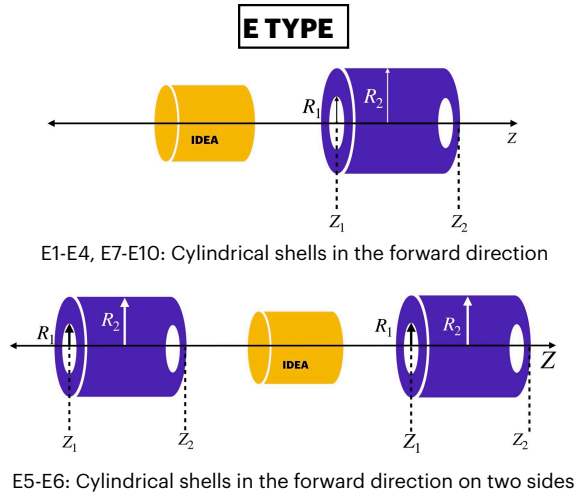


Figure 29: “E” series detectors – illustration

Detector	R_1 (m)	R_2 (m)	Z_1 (m)	Z_2 (m)
E1	2	5	10	15
E2	5	10	10	25
E3	5	10	15	20
E4	5	10	20	30
E5	5	10	± 10	± 25
E6	5	10	± 15	± 25
E7	0.1	5	10	15
E8	1	6	15	25
E9	2	10	10	20
E10	5	10	10	20

Table 28: “E” series detectors – parameters

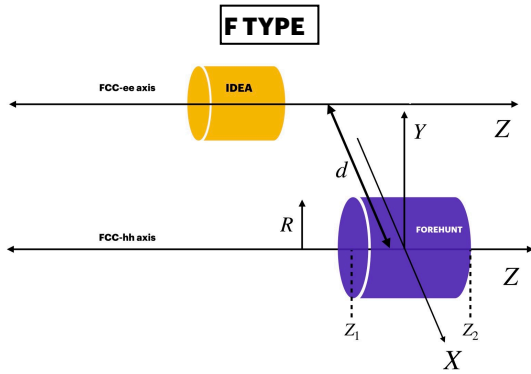
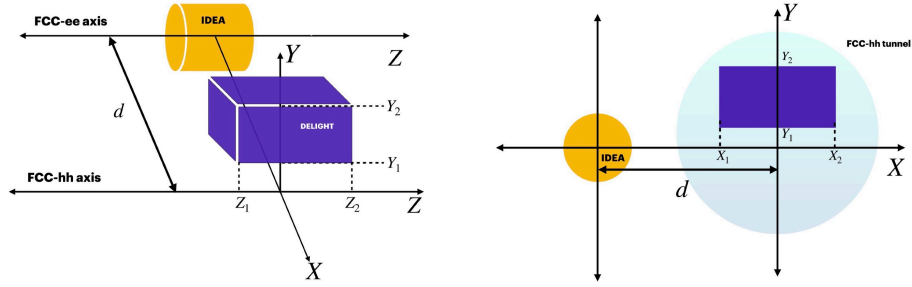


Figure 30: “F” series detectors – illustration

Detector	d (m)	R (m)	Z_1 (m)	Z_2 (m)
F1	10	1	50	60
F2		2	50	70
F3		5	50	75
F4		2	75	100
F5		5	75	100
F6		5	100	120

Table 29: “F” series detectors – parameters

G TYPE



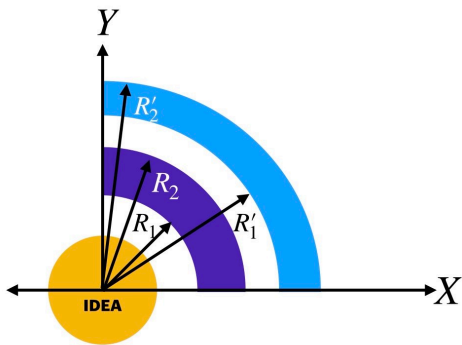
G1-G9: DELIGHT- Box shaped detectors placed transverse to the FCC-hh.

Figure 31: “G” series detectors – illustration

Detector	d (m)	X_1 (m)	X_2 (m)	Y_1 (m)	Y_2 (m)	Z_1 (m)	Z_2 (m)
G1	10	-50	50	25	50	-50	50
G2		-50	50	25	125	-50	50
G3		-25	25	25	225	-25	25
G4		-25	25	25	50	-25	25
G5		-12.5	12.5	25	50	-12.5	12.5
G6		-25	25	25	75	-25	25
G7		0	25	0	30	-50	50
G8		-25	25	25	125	-25	25
G9		25	75	-25	25	-25	25

Table 30: “G” series detectors – parameters

H TYPE

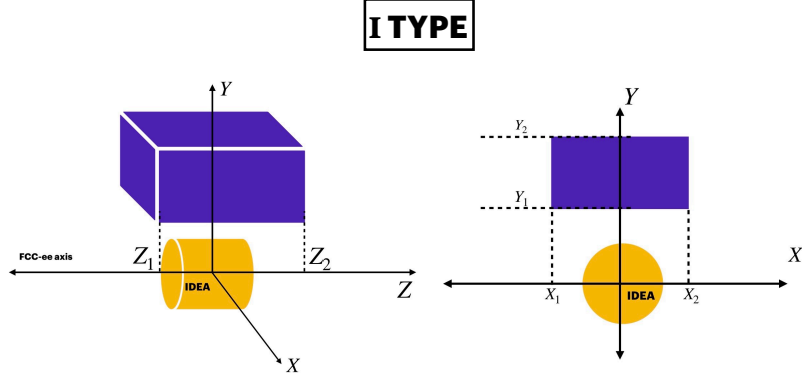


Detector	R_1 (m)	R_2 (m)	R_1' (m)	R_2' (m)	L (m)
H1	9	10	12	13	6
H2	9	14	18	23	6

H1-H2: Two cylindrical 90 degree arcs of length L , near to and far from the IDEA detector

Figure 32: “H” series detectors – illustration

Table 31: “H” series detectors – parameters



I1 - I6: Box shaped detectors over IDEA detector

Figure 33: “I” series detectors – illustration

Detector	X_1 (m)	X_2 (m)	Y_1 (m)	Y_2 (m)	Z_1 (m)	Z_2 (m)
I1	−50	50	100	110	−50	50
I2	−50	50	100	150	−50	50
I3	−25	25	50	70	−25	25
I4	−25	25	30	70	−25	25
I5	−3.5	3.5	30	70	−7	7
I6	−7	7	30	70	−3.5	3.5

Table 32: “I” series detectors – parameters

C Efficiency maps of dedicated detectors in the case of $B \rightarrow K\phi$

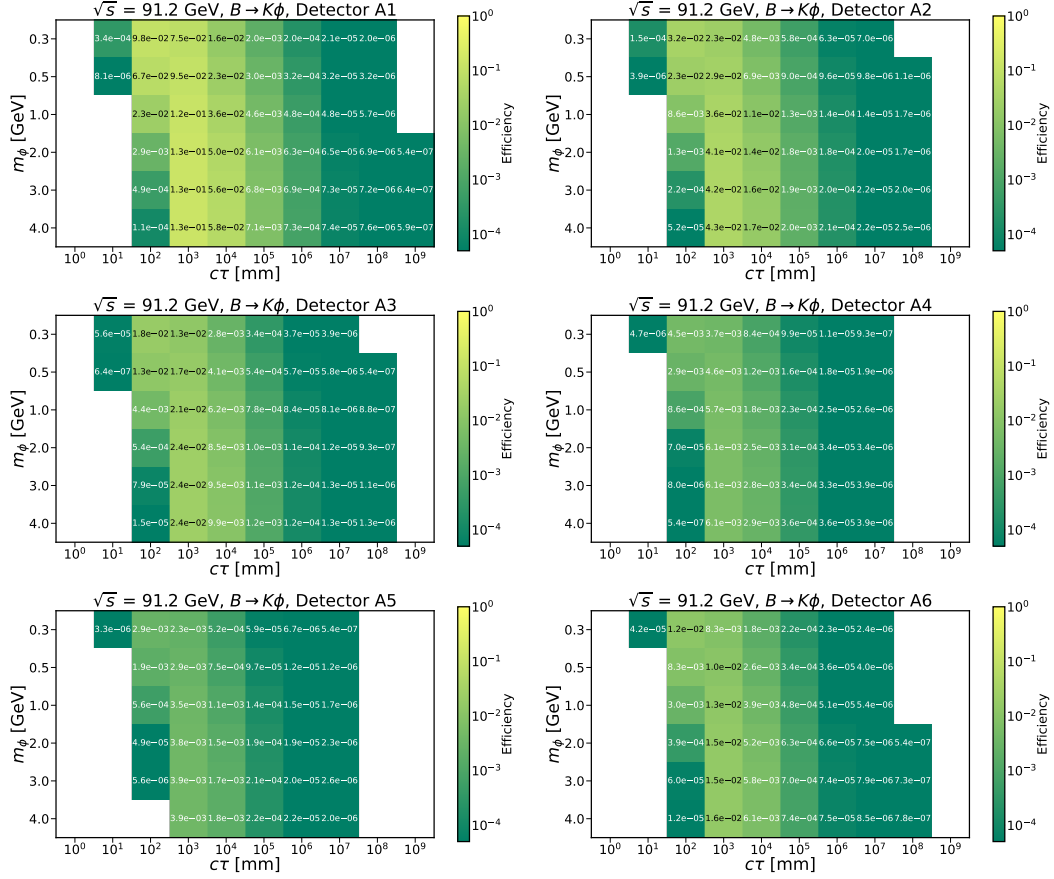


Figure 34: Efficiency map of the A-type dedicated detectors in the $m_\phi - c\tau$ plane, for the LLPs produced via the process $B \rightarrow K\phi$.

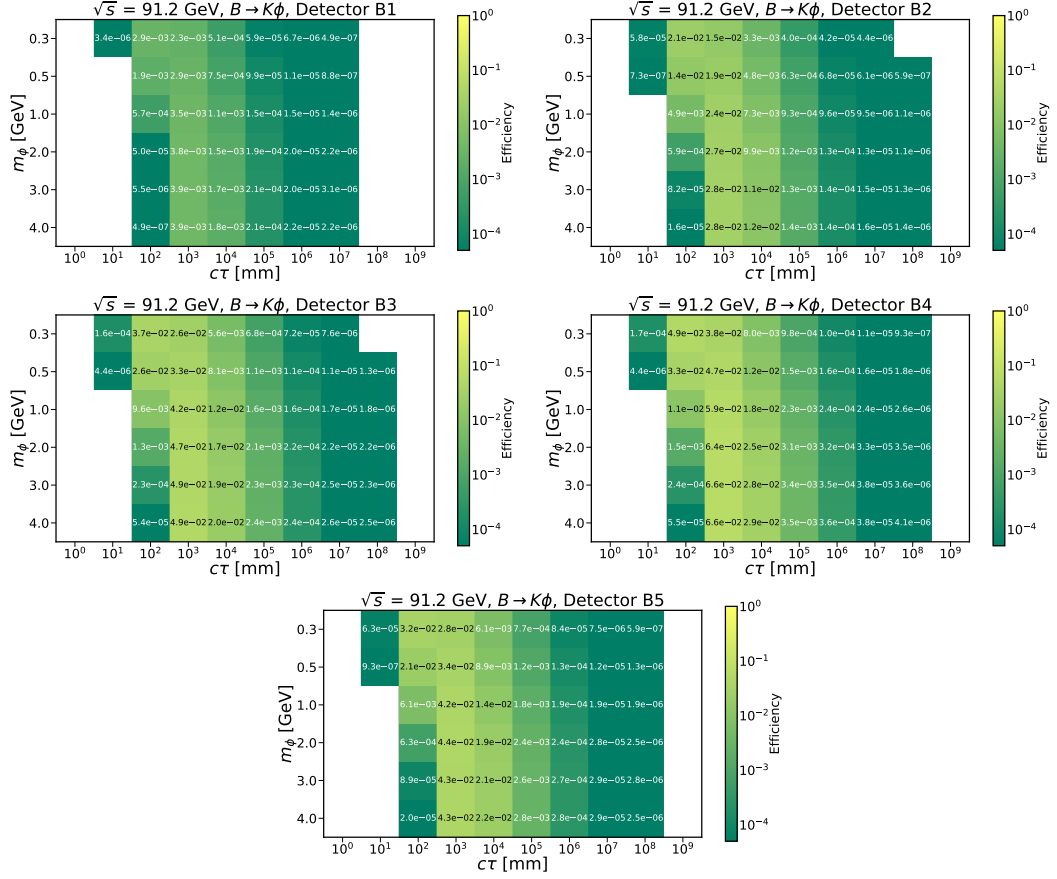


Figure 35: Efficiency map of the B-type dedicated detectors in the $m_\phi - c\tau$ plane, for the LLPs produced via the process $B \rightarrow K\phi$.

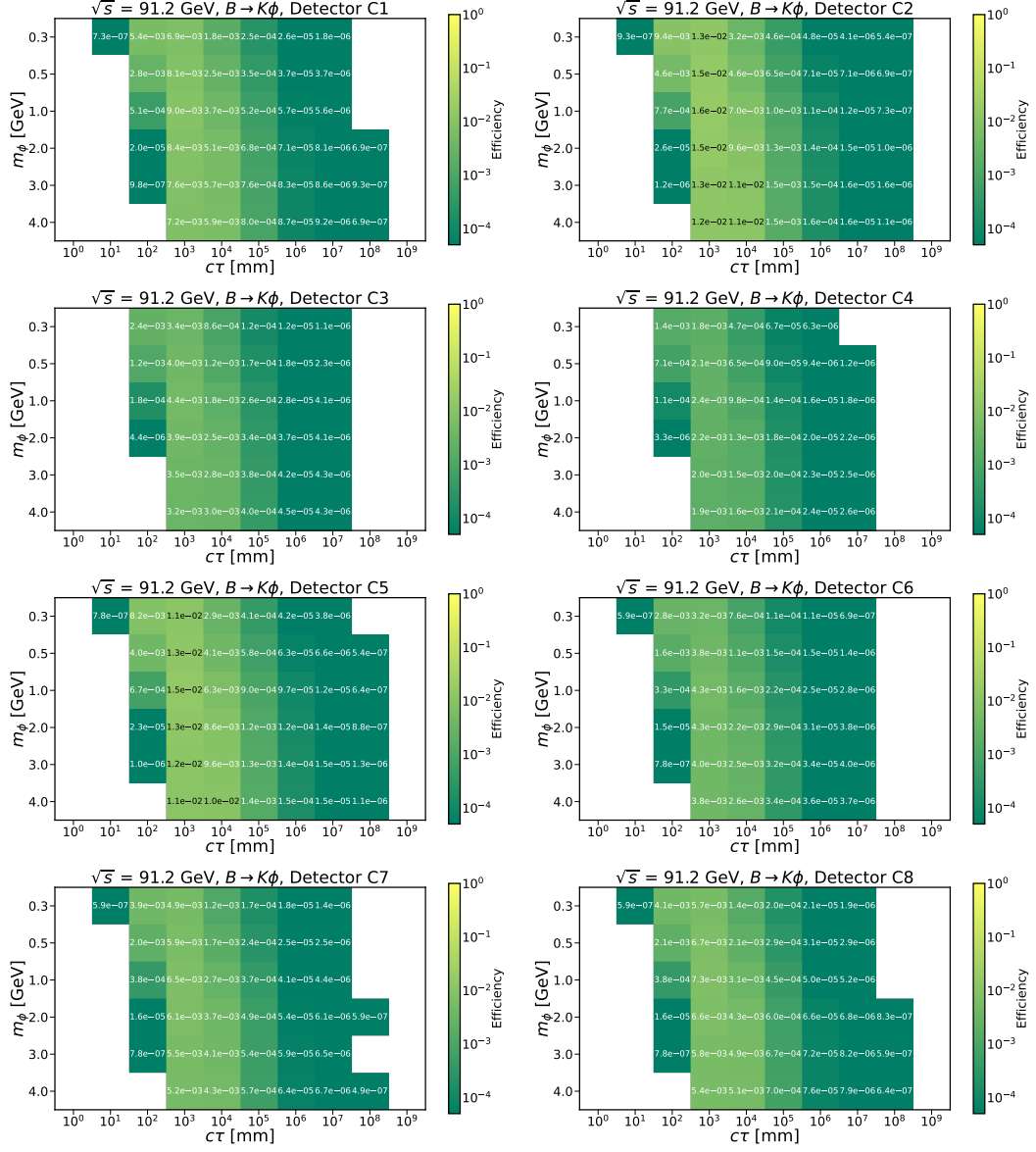


Figure 36: Efficiency map of the C-type dedicated detectors in the $m_\phi - c\tau$ plane, for the LLPs produced via the process $B \rightarrow K\phi$.

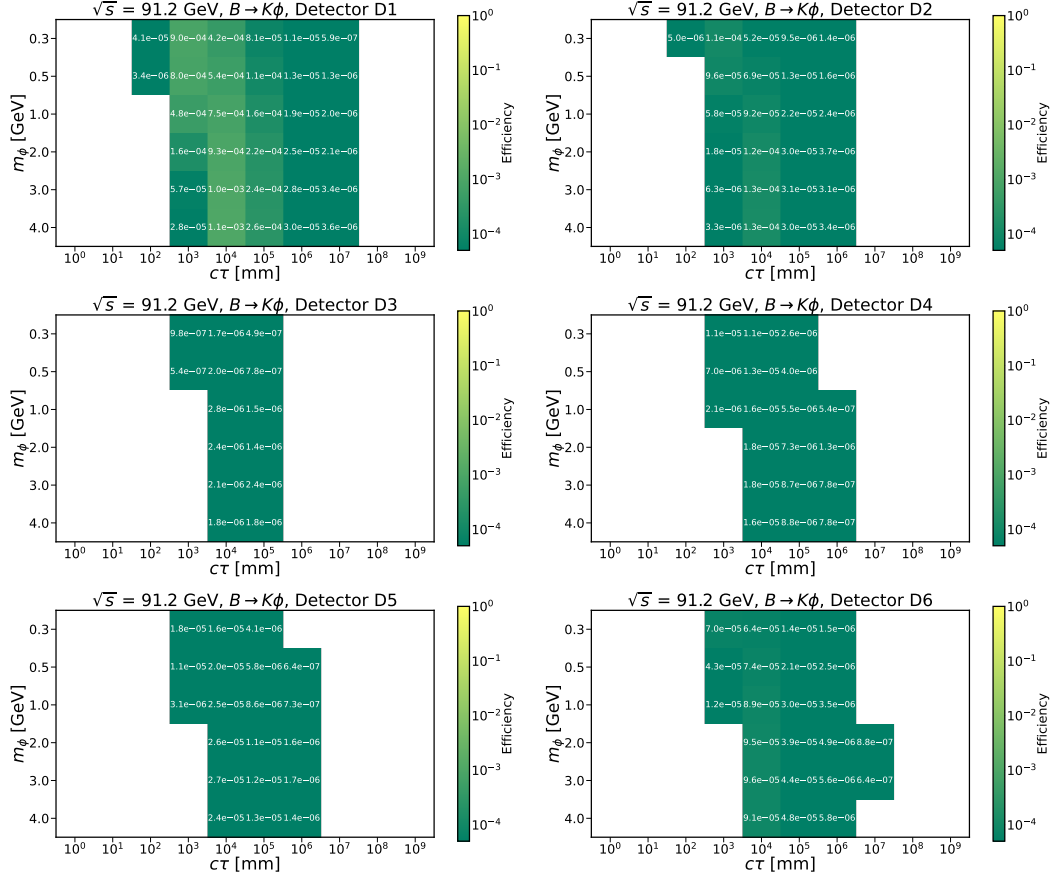


Figure 37: Efficiency map of the D-type dedicated detectors in the $m_\phi - c\tau$ plane, for the LLPs produced via the process $B \rightarrow K\phi$.

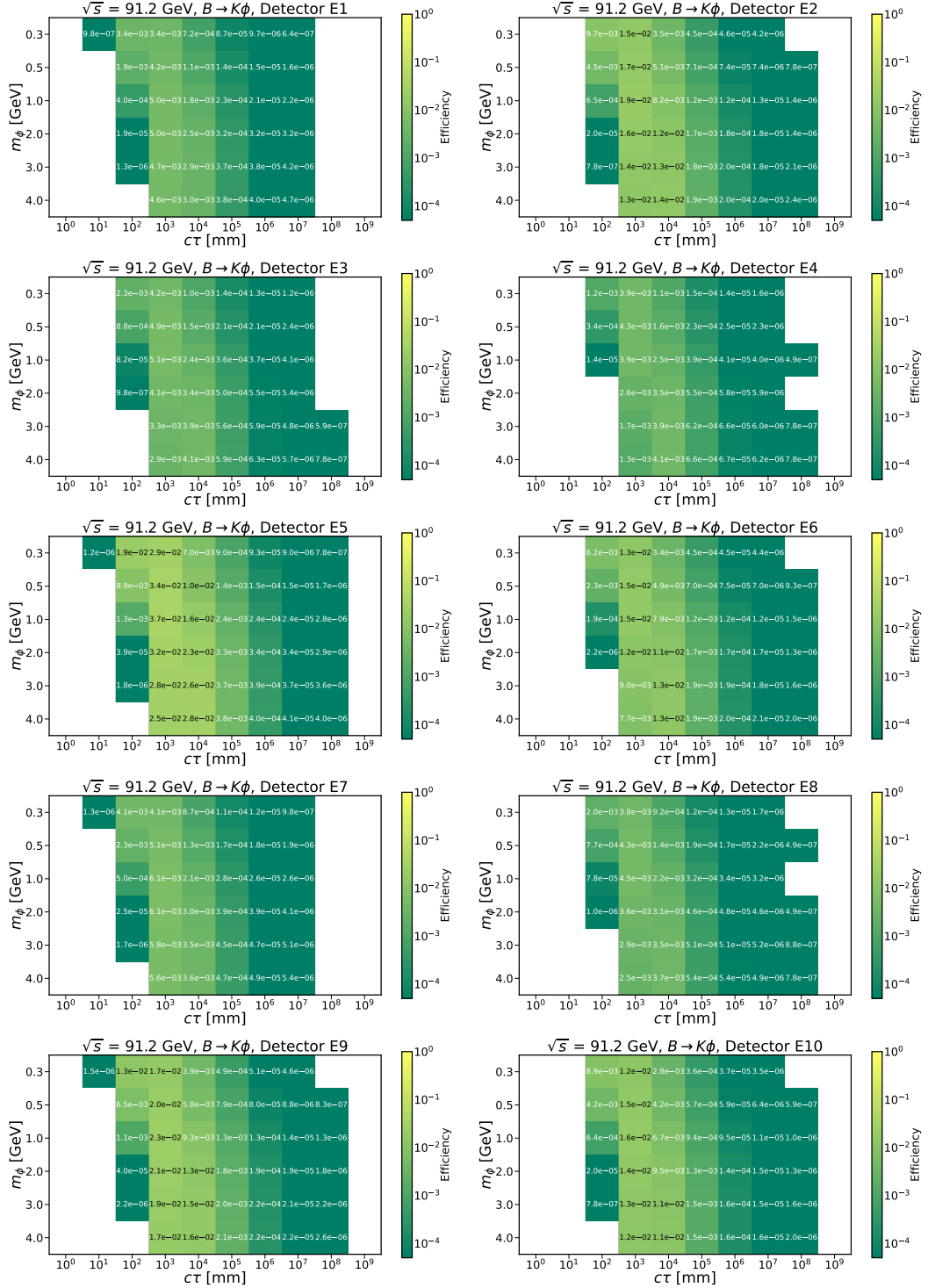


Figure 38: Efficiency map of the E-type dedicated detectors in the $m_\phi - c\tau$ plane, for the LLPs produced via the process $B \rightarrow K\phi$.

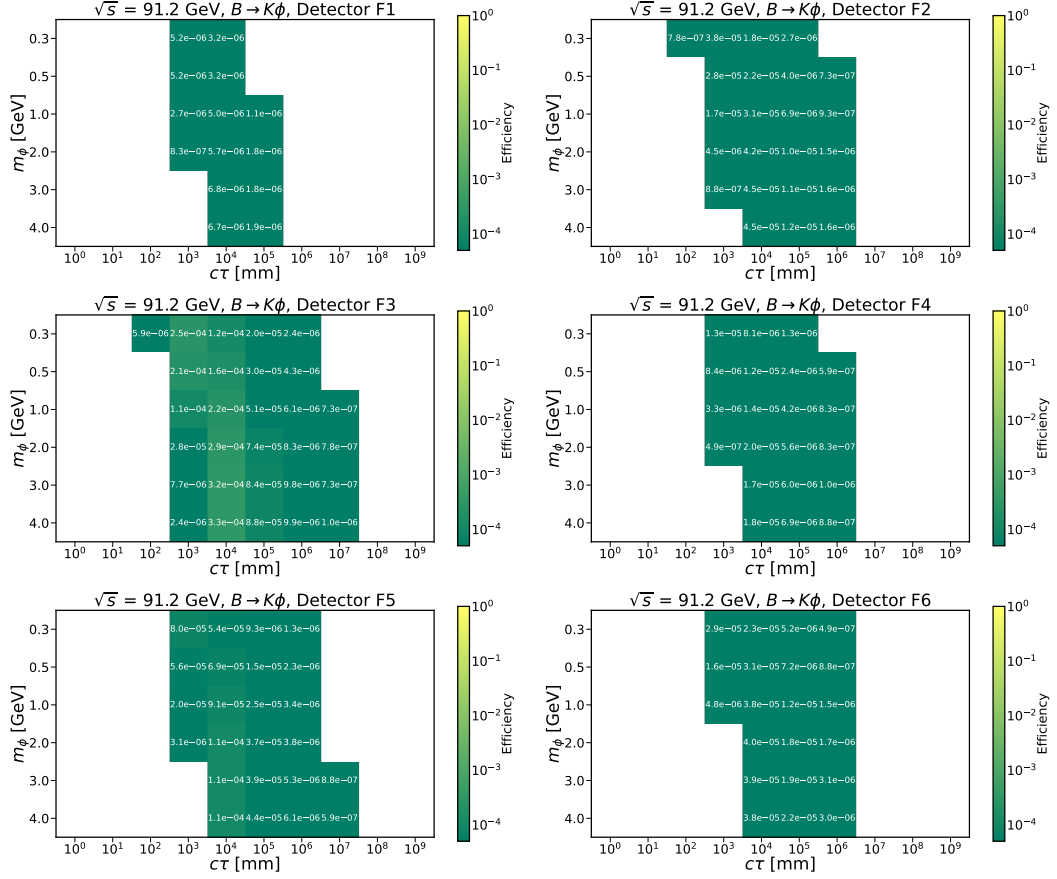


Figure 39: Efficiency map of the F-type dedicated detectors in the $m_\phi - c\tau$ plane, for the LLPs produced via the process $B \rightarrow K\phi$.

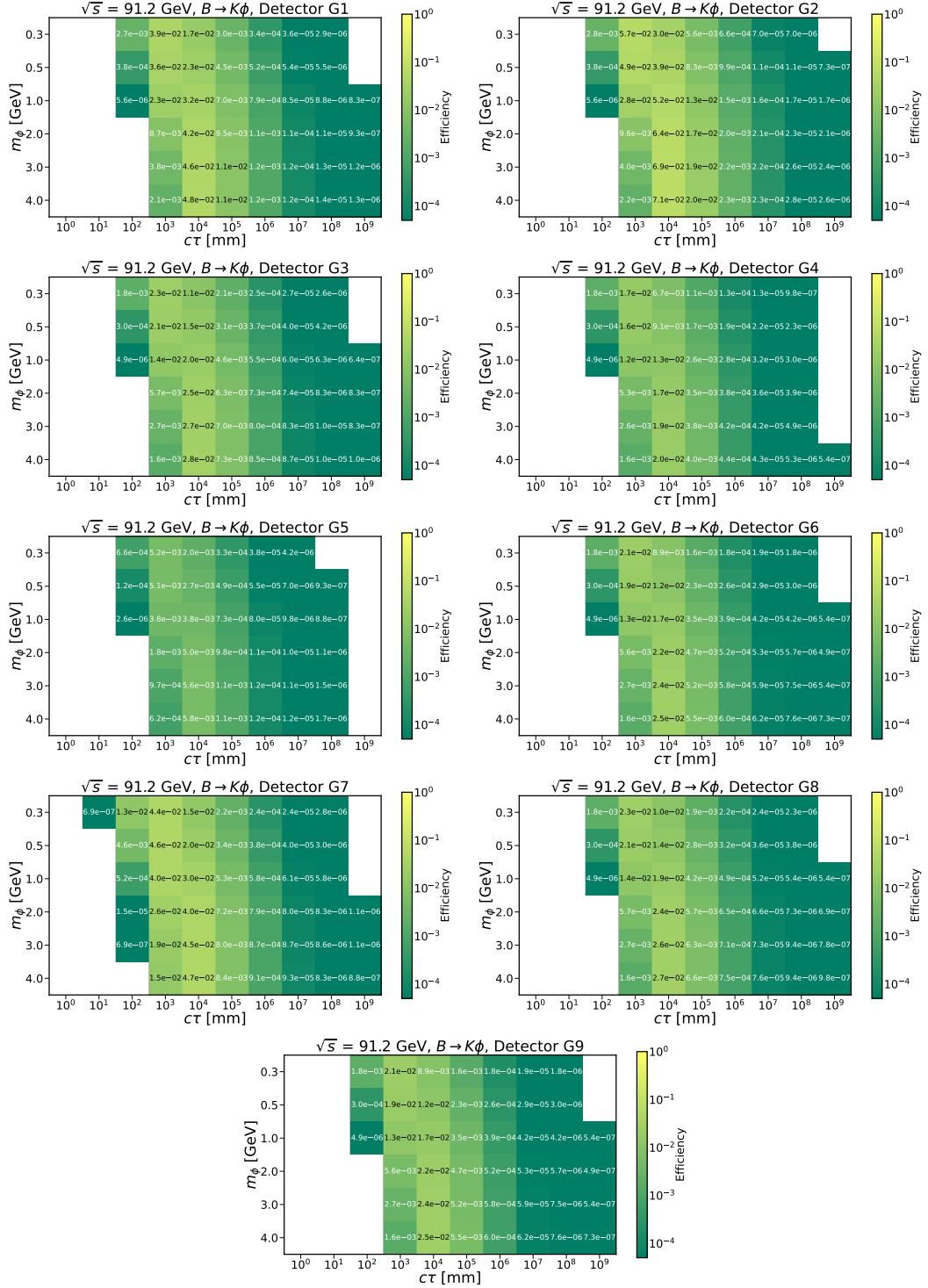


Figure 40: Efficiency map of the G-type dedicated detectors in the $m_\phi - c\tau$ plane, for the LLPs produced via the process $B \rightarrow K\phi$.

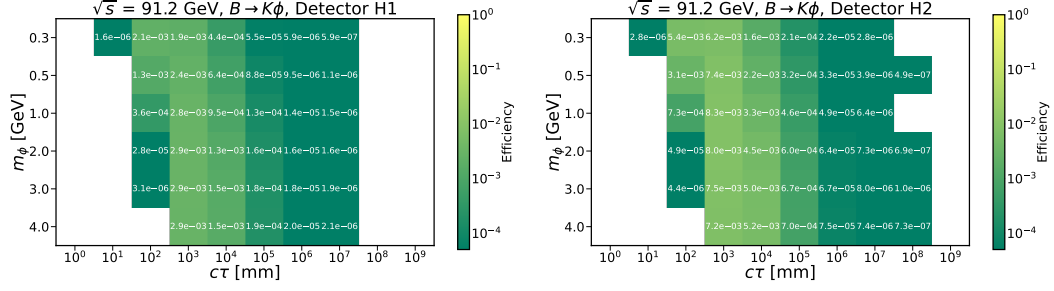


Figure 41: Efficiency map of the H-type dedicated detectors in the $m_\phi - c\tau$ plane, for the LLPs produced via the process $B \rightarrow K\phi$.

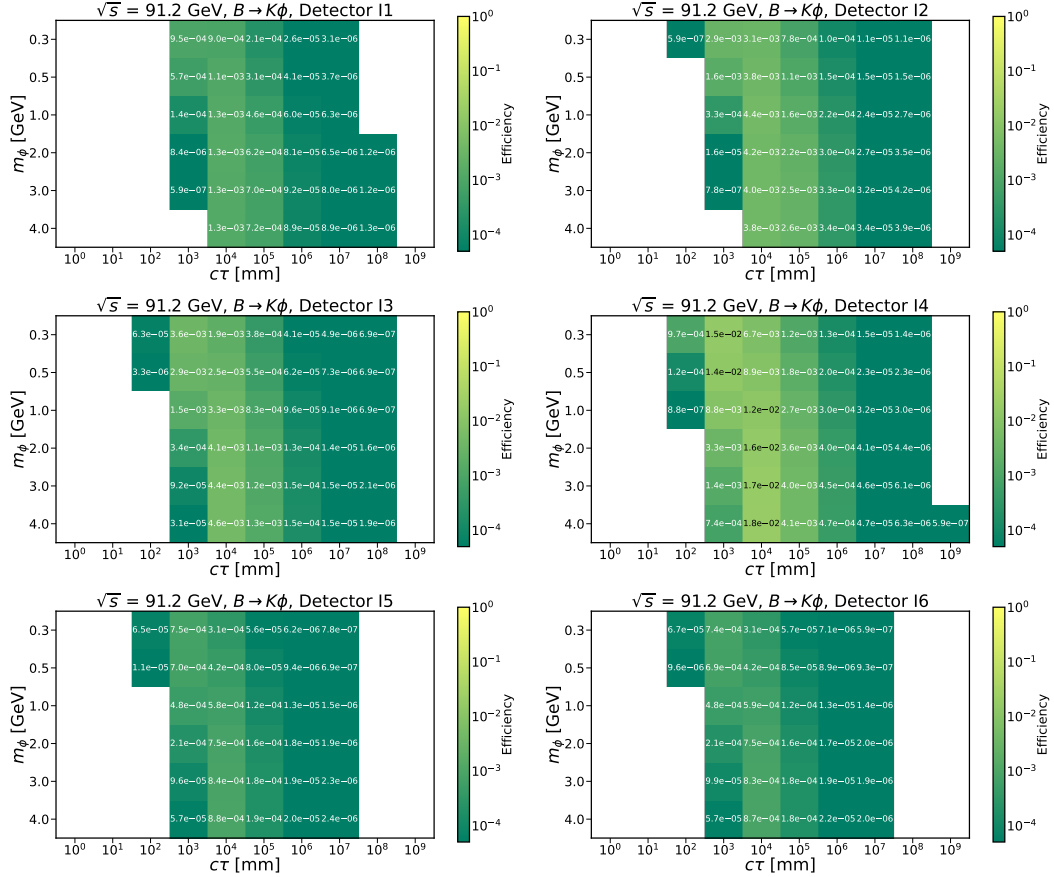


Figure 42: Efficiency map of the I-type dedicated detectors in the $m_\phi - c\tau$ plane, for the LLPs produced via the process $B \rightarrow K\phi$.

D Efficiency maps of dedicated detectors in the case of $h \rightarrow \phi\phi$

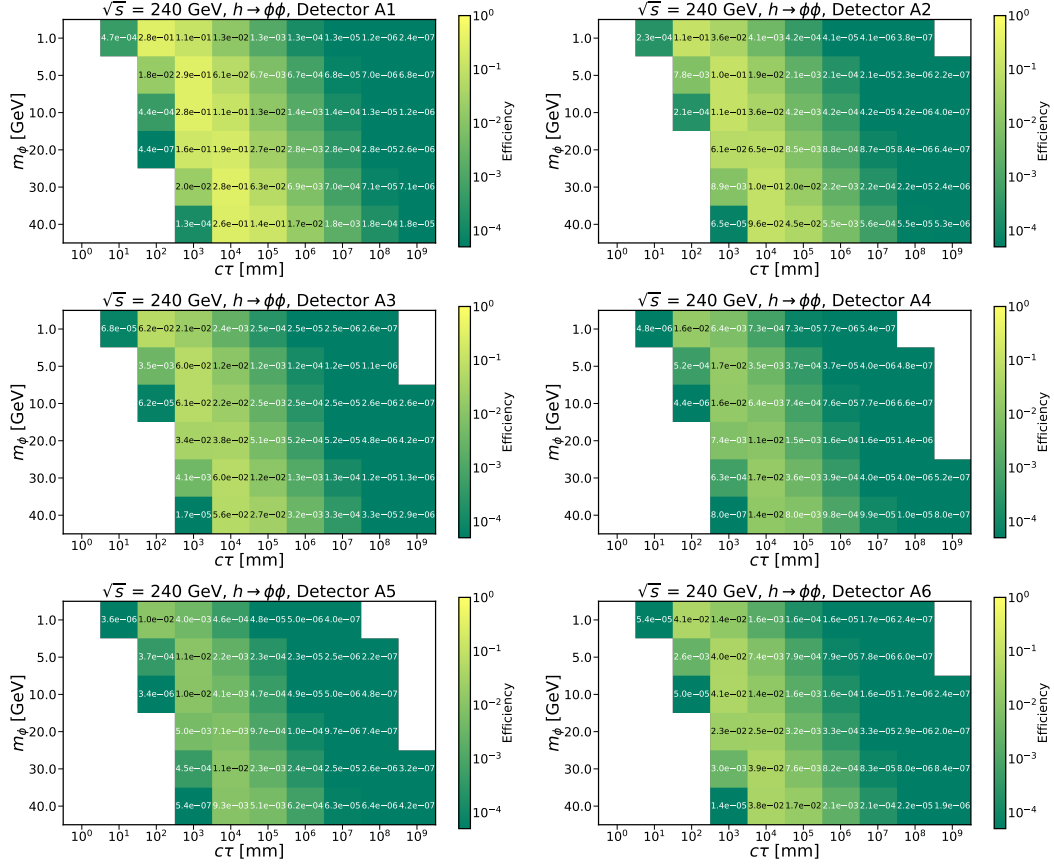


Figure 43: Efficiency map of the A-type dedicated detectors in the $m_\phi - c\tau$ plane, for the LLPs produced via the process $h \rightarrow \phi\phi$.

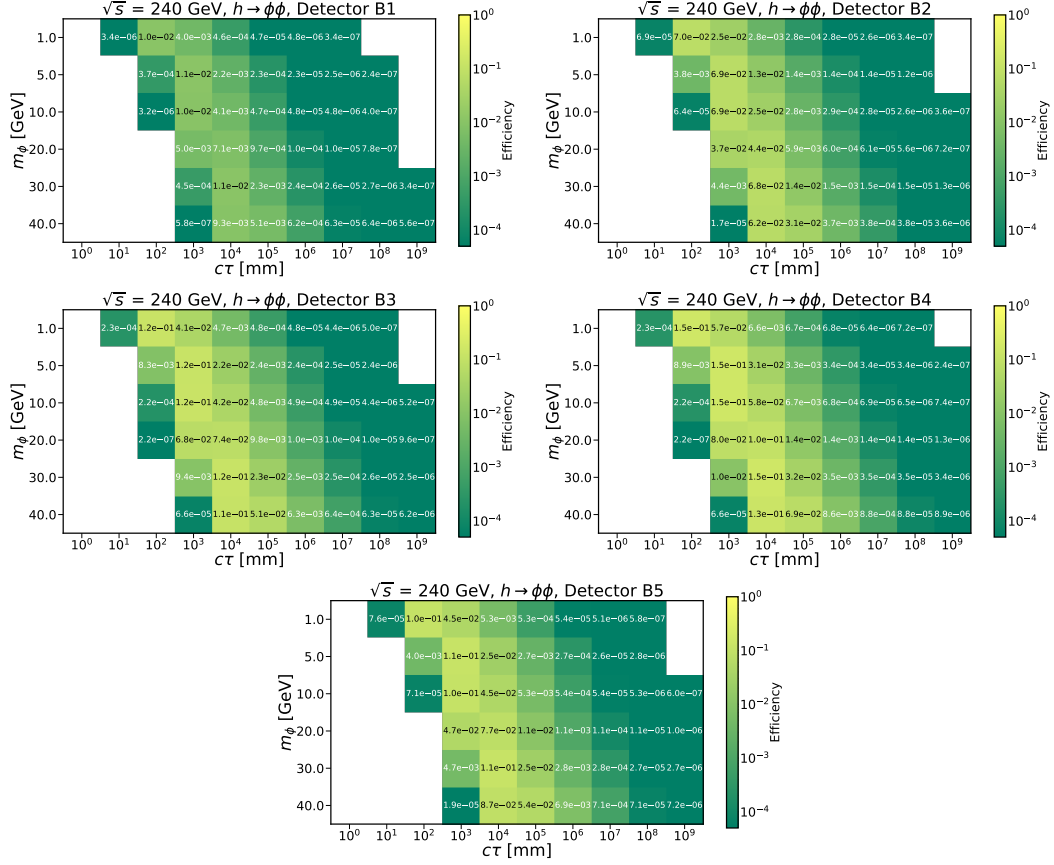


Figure 44: Efficiency map of the B-type dedicated detectors in the $m_\phi - c\tau$ plane, for the LLPs produced via the process $h \rightarrow \phi\phi$.

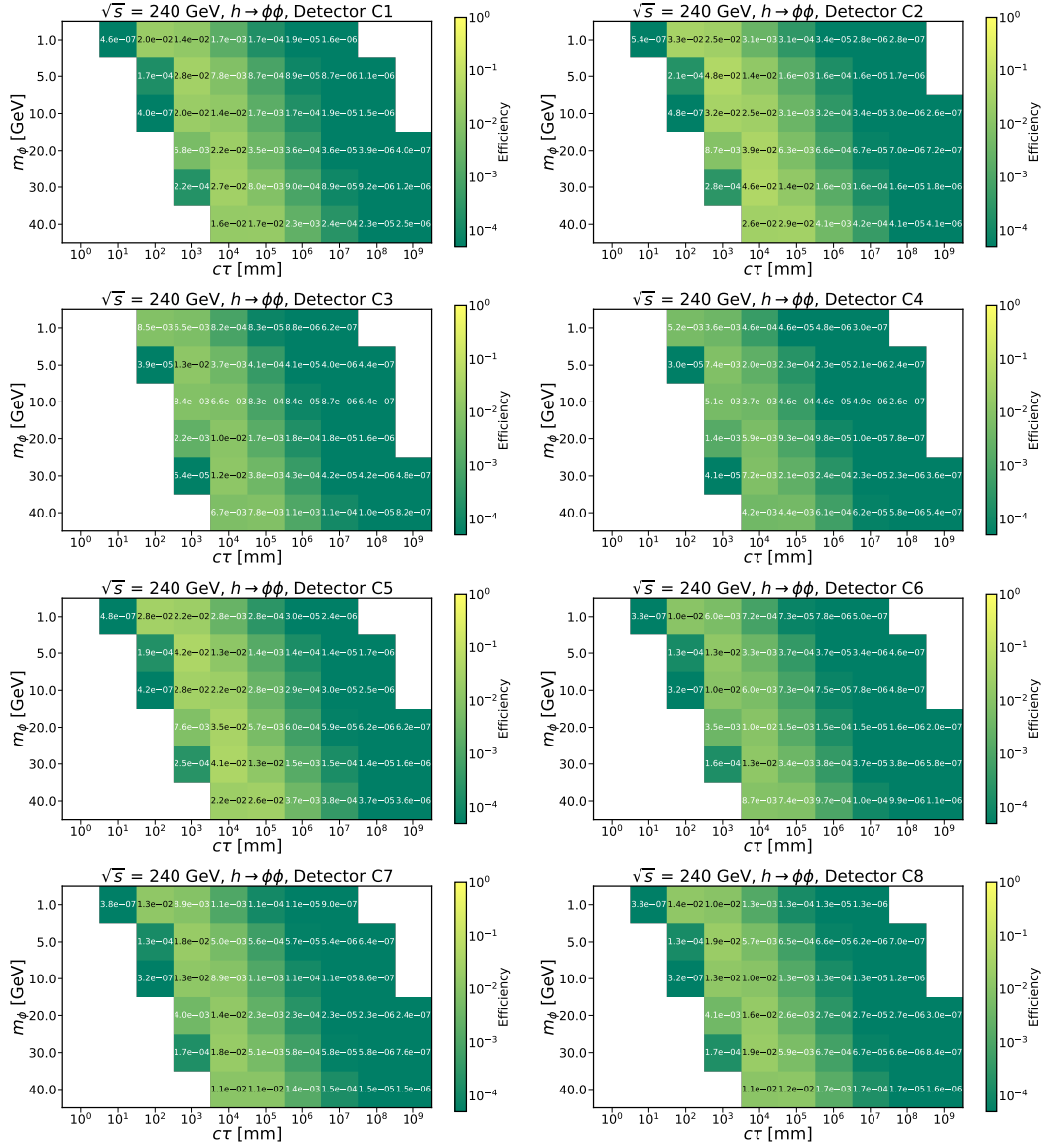


Figure 45: Efficiency map of the C-type dedicated detectors in the $m_\phi - c\tau$ plane, for the LLPs produced via the process $h \rightarrow \phi\phi$.

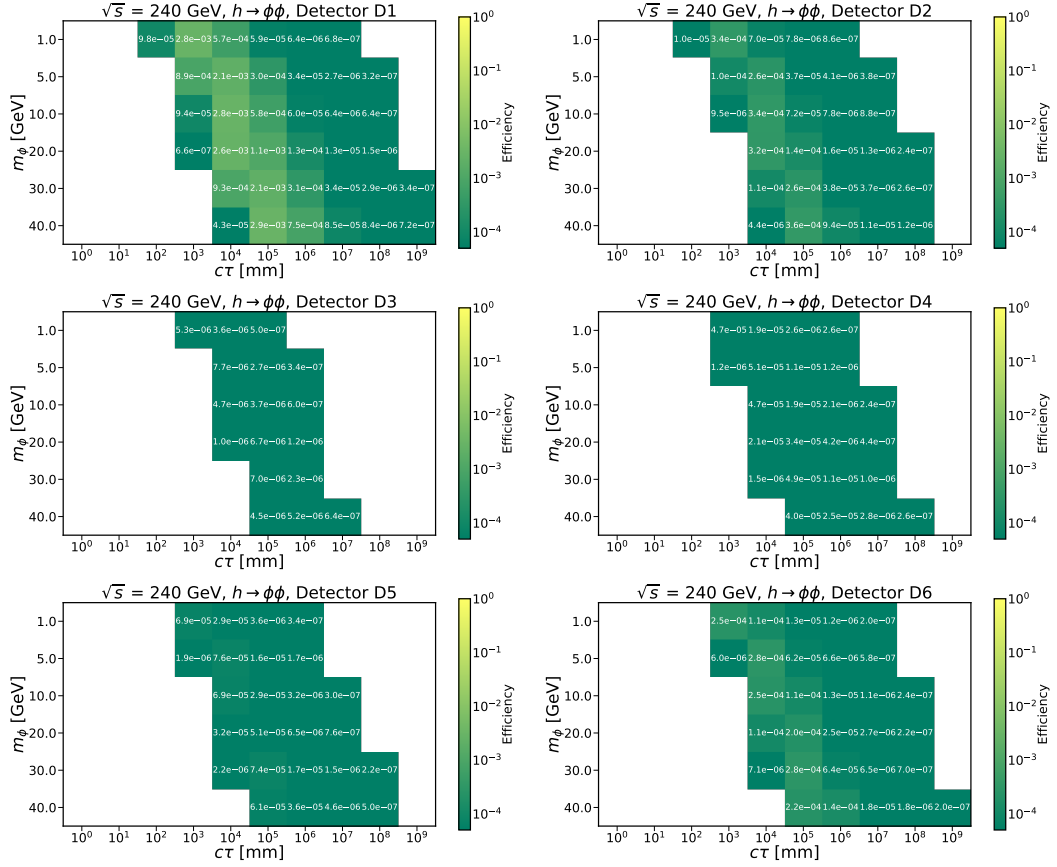


Figure 46: Efficiency map of the D-type dedicated detectors in the $m_\phi - c\tau$ plane, for the LLPs produced via the process $h \rightarrow \phi\phi$.

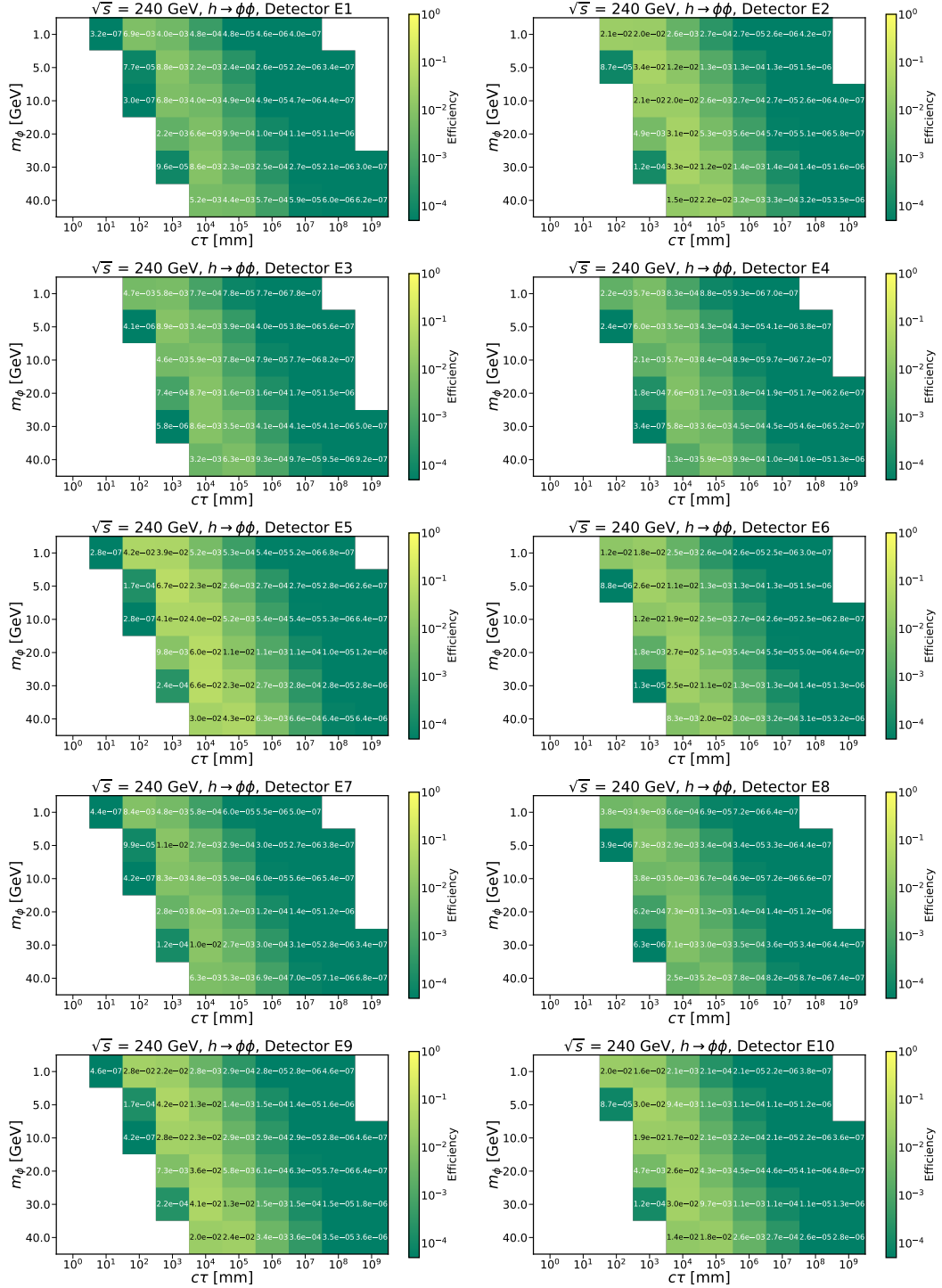


Figure 47: Efficiency map of the E-type dedicated detectors in the $m_\phi - c\tau$ plane, for the LLPs produced via the process $h \rightarrow \phi\phi$.

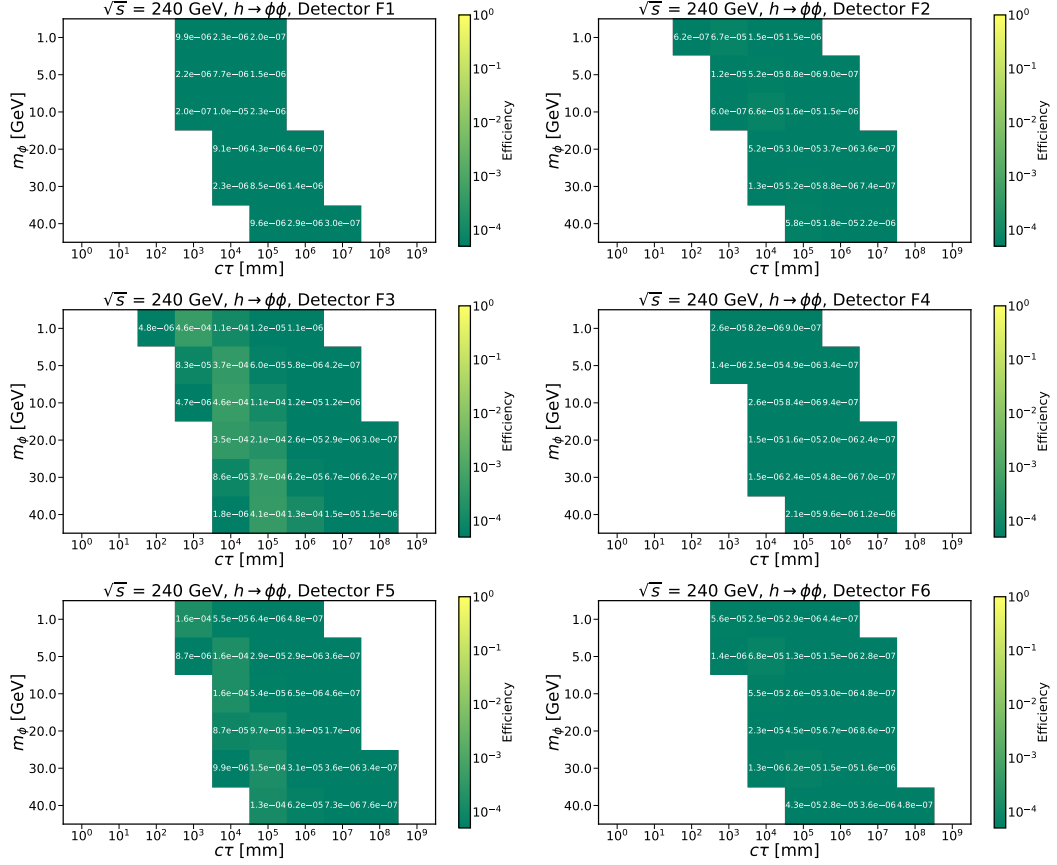


Figure 48: Efficiency map of the F-type dedicated detectors in the $m_\phi - c\tau$ plane, for the LLPs produced via the process $h \rightarrow \phi\phi$.

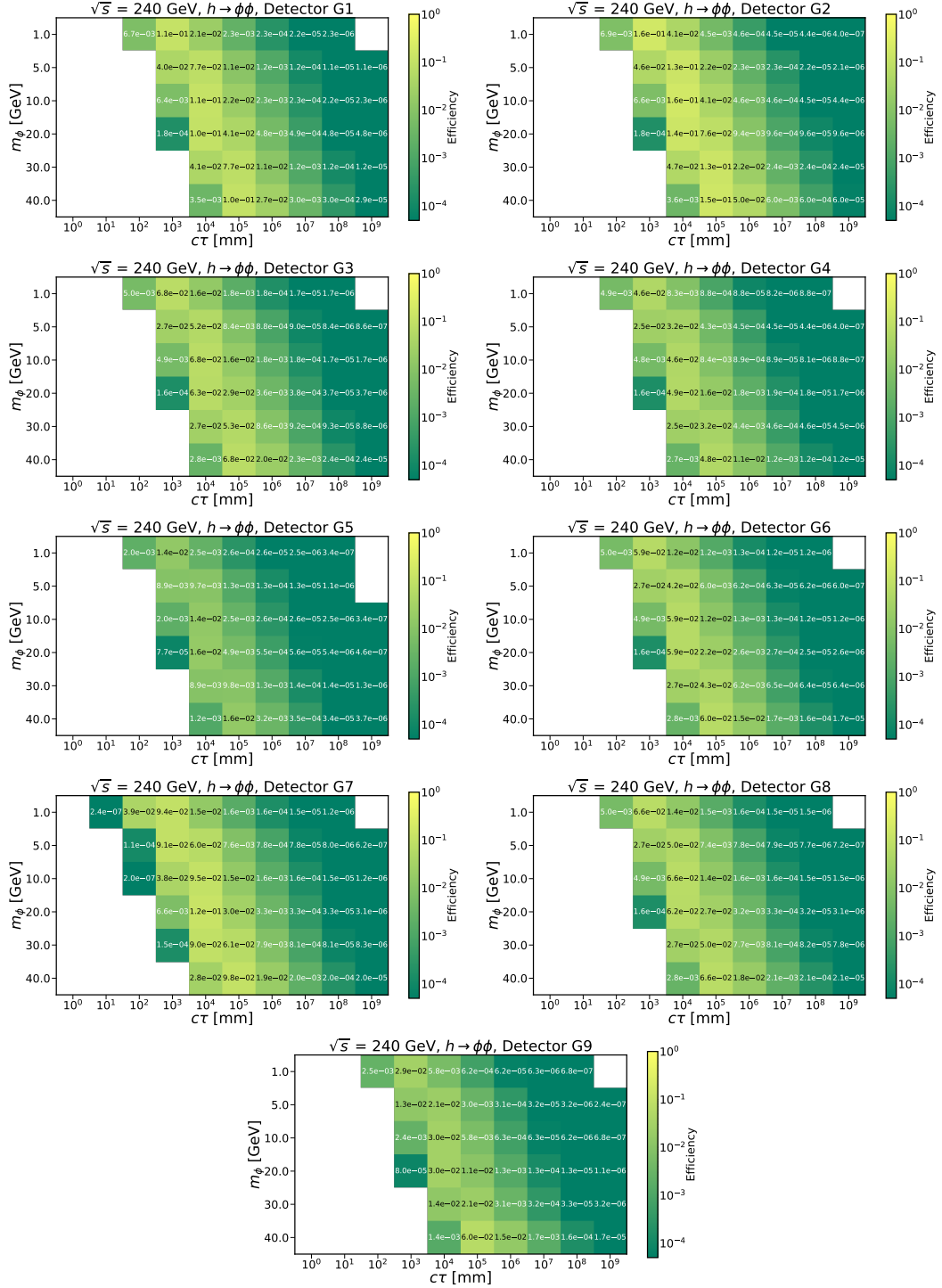


Figure 49: Efficiency map of the G-type dedicated detectors in the $m_\phi - c\tau$ plane, for the LLPs produced via the process $h \rightarrow \phi\phi$.

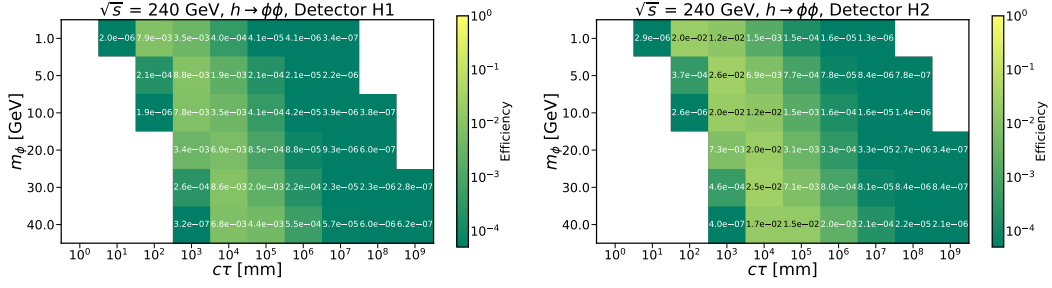


Figure 50: Efficiency map of the H-type dedicated detectors in the $m_\phi - c\tau$ plane, for the LLPs produced via the process $h \rightarrow \phi\phi$.

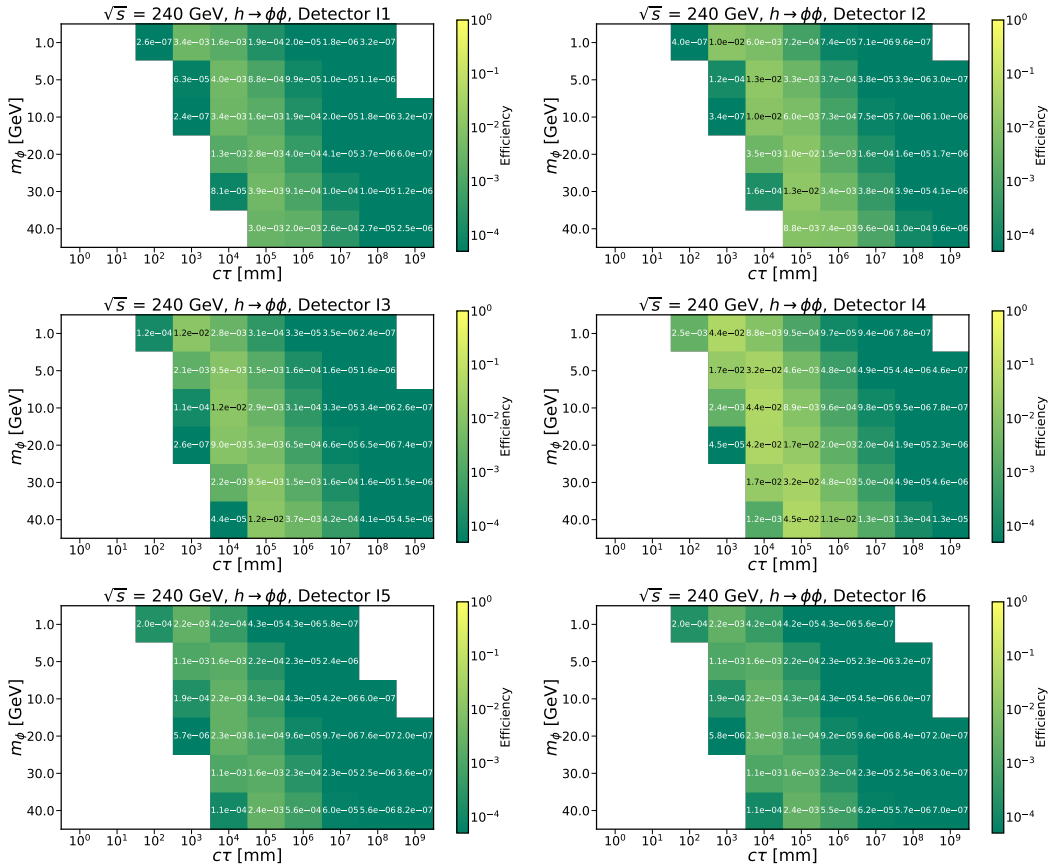


Figure 51: Efficiency map of the I-type dedicated detectors in the $m_\phi - c\tau$ plane, for the LLPs produced via the process $h \rightarrow \phi\phi$.

References

- [1] S. Dimopoulos, M. Dine, S. Raby, and S. D. Thomas, “Experimental signatures of low-energy gauge mediated supersymmetry breaking,” *Phys. Rev. Lett.* **76** (1996) 3494–3497, [arXiv:hep-ph/9601367](#).
- [2] G. R. Farrar, “Detecting gluino - containing hadrons,” *Phys. Rev. Lett.* **76** (1996) 4111–4114, [arXiv:hep-ph/9603271](#).
- [3] G. F. Giudice and R. Rattazzi, “Theories with gauge mediated supersymmetry breaking,” *Phys. Rept.* **322** (1999) 419–499, [arXiv:hep-ph/9801271](#).
- [4] H. Baer, K.-m. Cheung, and J. F. Gunion, “A Heavy gluino as the lightest supersymmetric particle,” *Phys. Rev. D* **59** (1999) 075002, [arXiv:hep-ph/9806361](#).
- [5] D. Choudhury, H. K. Dreiner, P. Richardson, and S. Sarkar, “A Supersymmetric solution to the KARMEN time anomaly,” *Phys. Rev. D* **61** (2000) 095009, [arXiv:hep-ph/9911365](#).
- [6] A. Mafi and S. Raby, “An Analysis of a heavy gluino LSP at CDF: The Heavy gluino window,” *Phys. Rev. D* **62** (2000) 035003, [arXiv:hep-ph/9912436](#).
- [7] A. C. Kraan, “Interactions of heavy stable hadronizing particles,” *Eur. Phys. J. C* **37** (2004) 91–104, [arXiv:hep-ex/0404001](#).
- [8] R. Mackeprang and A. Rizzi, “Interactions of Coloured Heavy Stable Particles in Matter,” *Eur. Phys. J. C* **50** (2007) 353–362, [arXiv:hep-ph/0612161](#).
- [9] N. Arkani-Hamed and S. Dimopoulos, “Supersymmetric unification without low energy supersymmetry and signatures for fine-tuning at the LHC,” *JHEP* **06** (2005) 073, [arXiv:hep-th/0405159](#).
- [10] G. F. Giudice and A. Romanino, “Split supersymmetry,” *Nucl. Phys. B* **699** (2004) 65–89, [arXiv:hep-ph/0406088](#). [Erratum: Nucl.Phys.B 706, 487–487 (2005)].
- [11] J. L. Hewett, B. Lillie, M. Masip, and T. G. Rizzo, “Signatures of long-lived gluinos in split supersymmetry,” *JHEP* **09** (2004) 070, [arXiv:hep-ph/0408248](#).
- [12] A. Arvanitaki, S. Dimopoulos, A. Pierce, S. Rajendran, and J. G. Wacker, “Stopping gluinos,” *Phys. Rev. D* **76** (2007) 055007, [arXiv:hep-ph/0506242](#).
- [13] P. Meade, M. Reece, and D. Shih, “Long-Lived Neutralino NLSPs,” *JHEP* **10** (2010) 067, [arXiv:1006.4575](#) [[hep-ph](#)].
- [14] H. K. Dreiner, S. Heinemeyer, O. Kittel, U. Langenfeld, A. M. Weber, and G. Weiglein, “Mass Bounds on a Very Light Neutralino,” *Eur. Phys. J. C* **62** (2009) 547–572, [arXiv:0901.3485](#) [[hep-ph](#)].
- [15] J. A. Conley, H. K. Dreiner, and P. Wienemann, “Measuring a Light Neutralino Mass at the ILC: Testing the MSSM Neutralino Cold Dark Matter Model,” *Phys. Rev. D* **83** (2011) 055018, [arXiv:1012.1035](#) [[hep-ph](#)].
- [16] J. Fan, M. Reece, and J. T. Ruderman, “A Stealth Supersymmetry Sampler,” *JHEP* **07** (2012) 196, [arXiv:1201.4875](#) [[hep-ph](#)].

- [17] G. Bhattacharyya and T. S. Ray, “Naturally split supersymmetry,” *JHEP* **05** (2012) 022, [arXiv:1201.1131 \[hep-ph\]](#).
- [18] B. Bhattacharjee, B. Feldstein, M. Ibe, S. Matsumoto, and T. T. Yanagida, “Pure gravity mediation of supersymmetry breaking at the Large Hadron Collider,” *Phys. Rev. D* **87** no. 1, (2013) 015028, [arXiv:1207.5453 \[hep-ph\]](#).
- [19] A. Arvanitaki, N. Craig, S. Dimopoulos, and G. Villadoro, “Mini-Split,” *JHEP* **02** (2013) 126, [arXiv:1210.0555 \[hep-ph\]](#).
- [20] S. Banerjee, G. Bélanger, B. Mukhopadhyaya, and P. D. Serpico, “Signatures of sneutrino dark matter in an extension of the CMSSM,” *JHEP* **07** (2016) 095, [arXiv:1603.08834 \[hep-ph\]](#).
- [21] N. Nagata, H. Otono, and S. Shirai, “Cornering Compressed Gluino at the LHC,” *JHEP* **03** (2017) 025, [arXiv:1701.07664 \[hep-ph\]](#).
- [22] S. Banerjee, G. Bélanger, A. Ghosh, and B. Mukhopadhyaya, “Long-lived stau, sneutrino dark matter and right-slepton spectrum,” *JHEP* **09** (2018) 143, [arXiv:1806.04488 \[hep-ph\]](#).
- [23] H. Ito, O. Jinnouchi, T. Moroi, N. Nagata, and H. Otono, “Searching for Metastable Particles with Sub-Millimeter Displaced Vertices at Hadron Colliders,” *JHEP* **06** (2018) 112, [arXiv:1803.00234 \[hep-ph\]](#).
- [24] H. K. Dreiner, J. Y. Günther, and Z. S. Wang, “ R -parity violation and light neutralinos at ANUBIS and MAPP,” *Phys. Rev. D* **103** no. 7, (2021) 075013, [arXiv:2008.07539 \[hep-ph\]](#).
- [25] H. K. Dreiner, H. E. Haber, and S. P. Martin, *From Spinors to Supersymmetry*. Cambridge University Press, Cambridge, UK, 7, 2023.
- [26] S. D. Thomas and J. D. Wells, “Phenomenology of Massive Vectorlike Doublet Leptons,” *Phys. Rev. Lett.* **81** (1998) 34–37, [arXiv:hep-ph/9804359](#).
- [27] M. Cirelli, N. Fornengo, and A. Strumia, “Minimal dark matter,” *Nucl. Phys. B* **753** (2006) 178–194, [arXiv:hep-ph/0512090](#).
- [28] P. Fileviez Perez, H. H. Patel, M. J. Ramsey-Musolf, and K. Wang, “Triplet Scalars and Dark Matter at the LHC,” *Phys. Rev. D* **79** (2009) 055024, [arXiv:0811.3957 \[hep-ph\]](#).
- [29] D. Tucker-Smith and N. Weiner, “Inelastic dark matter,” *Phys. Rev. D* **64** (2001) 043502, [arXiv:hep-ph/0101138](#).
- [30] Y. Bai and T. M. P. Tait, “Inelastic Dark Matter at the LHC,” *Phys. Lett. B* **710** (2012) 335–338, [arXiv:1109.4144 \[hep-ph\]](#).
- [31] N. Weiner and I. Yavin, “How Dark Are Majorana WIMPs? Signals from MiDM and Rayleigh Dark Matter,” *Phys. Rev. D* **86** (2012) 075021, [arXiv:1206.2910 \[hep-ph\]](#).
- [32] E. Izaguirre, G. Krnjaic, and B. Shuve, “Discovering Inelastic Thermal-Relic Dark

- Matter at Colliders,” *Phys. Rev. D* **93** no. 6, (2016) 063523, [arXiv:1508.03050 \[hep-ph\]](#).
- [33] K. Griest and D. Seckel, “Three exceptions in the calculation of relic abundances,” *Phys. Rev. D* **43** (1991) 3191–3203.
 - [34] M. J. Baker *et al.*, “The Coannihilation Codex,” *JHEP* **12** (2015) 120, [arXiv:1510.03434 \[hep-ph\]](#).
 - [35] V. V. Khoze, A. D. Plascencia, and K. Sakurai, “Simplified models of dark matter with a long-lived co-annihilation partner,” *JHEP* **06** (2017) 041, [arXiv:1702.00750 \[hep-ph\]](#).
 - [36] M. Garny, J. Heisig, B. Lülfi, and S. Vogl, “Coannihilation without chemical equilibrium,” *Phys. Rev. D* **96** no. 10, (2017) 103521, [arXiv:1705.09292 \[hep-ph\]](#).
 - [37] Y. Hochberg, E. Kuflik, and H. Murayama, “SIMP Spectroscopy,” *JHEP* **05** (2016) 090, [arXiv:1512.07917 \[hep-ph\]](#).
 - [38] L. J. Hall, K. Jedamzik, J. March-Russell, and S. M. West, “Freeze-In Production of FIMP Dark Matter,” *JHEP* **03** (2010) 080, [arXiv:0911.1120 \[hep-ph\]](#).
 - [39] R. T. Co, F. D’Eramo, L. J. Hall, and D. Pappadopulo, “Freeze-In Dark Matter with Displaced Signatures at Colliders,” *JCAP* **12** (2015) 024, [arXiv:1506.07532 \[hep-ph\]](#).
 - [40] A. G. Hessler, A. Ibarra, E. Molinaro, and S. Vogl, “Probing the scotogenic FIMP at the LHC,” *JHEP* **01** (2017) 100, [arXiv:1611.09540 \[hep-ph\]](#).
 - [41] A. Ghosh, T. Mondal, and B. Mukhopadhyaya, “Heavy stable charged tracks as signatures of non-thermal dark matter at the LHC : a study in some non-supersymmetric scenarios,” *JHEP* **12** (2017) 136, [arXiv:1706.06815 \[hep-ph\]](#).
 - [42] G. Bélanger *et al.*, “LHC-friendly minimal freeze-in models,” *JHEP* **02** (2019) 186, [arXiv:1811.05478 \[hep-ph\]](#).
 - [43] A. Goudelis, K. A. Mohan, and D. Sengupta, “Clockworking FIMPs,” *JHEP* **10** (2018) 014, [arXiv:1807.06642 \[hep-ph\]](#).
 - [44] M. Garny and J. Heisig, “Interplay of super-WIMP and freeze-in production of dark matter,” *Phys. Rev. D* **98** no. 9, (2018) 095031, [arXiv:1809.10135 \[hep-ph\]](#).
 - [45] P. Minkowski, “ $\mu \rightarrow e\gamma$ at a Rate of One Out of 10^9 Muon Decays?,” *Phys. Lett. B* **67** (1977) 421–428.
 - [46] T. Yanagida, “Horizontal gauge symmetry and masses of neutrinos,” *Conf. Proc. C* **7902131** (1979) 95–99.
 - [47] M. Gell-Mann, P. Ramond, and R. Slansky, “Complex Spinors and Unified Theories,” *Conf. Proc. C* **790927** (1979) 315–321, [arXiv:1306.4669 \[hep-th\]](#).

- [48] R. N. Mohapatra and G. Senjanovic, “Neutrino Mass and Spontaneous Parity Nonconservation,” *Phys. Rev. Lett.* **44** (1980) 912.
- [49] R. N. Mohapatra and J. W. F. Valle, “Neutrino Mass and Baryon Number Nonconservation in Superstring Models,” *Phys. Rev. D* **34** (1986) 1642.
- [50] W.-Y. Keung and G. Senjanovic, “Majorana Neutrinos and the Production of the Right-handed Charged Gauge Boson,” *Phys. Rev. Lett.* **50** (1983) 1427.
- [51] A. Ferrari, J. Collot, M.-L. Andrieux, B. Belhorma, P. de Saintignon, J.-Y. Hostachy, P. Martin, and M. Wielers, “Sensitivity study for new gauge bosons and right-handed Majorana neutrinos in pp collisions at $s = 14\text{-TeV}$,” *Phys. Rev. D* **62** (2000) 013001.
- [52] J. C. Helo, M. Hirsch, and S. Kovalenko, “Heavy neutrino searches at the LHC with displaced vertices,” *Phys. Rev. D* **89** (2014) 073005, [arXiv:1312.2900 \[hep-ph\]](#). [Erratum: *Phys.Rev.D* 93, 099902 (2016)].
- [53] A. Maiezza, M. Nemevšek, and F. Nesti, “Lepton Number Violation in Higgs Decay at LHC,” *Phys. Rev. Lett.* **115** (2015) 081802, [arXiv:1503.06834 \[hep-ph\]](#).
- [54] E. Izaguirre and B. Shuve, “Multilepton and Lepton Jet Probes of Sub-Weak-Scale Right-Handed Neutrinos,” *Phys. Rev. D* **91** no. 9, (2015) 093010, [arXiv:1504.02470 \[hep-ph\]](#).
- [55] B. Batell, M. Pospelov, and B. Shuve, “Shedding Light on Neutrino Masses with Dark Forces,” *JHEP* **08** (2016) 052, [arXiv:1604.06099 \[hep-ph\]](#).
- [56] M. Nemevšek, F. Nesti, and J. C. Vasquez, “Majorana Higgses at colliders,” *JHEP* **04** (2017) 114, [arXiv:1612.06840 \[hep-ph\]](#).
- [57] E. Accomando, L. Delle Rose, S. Moretti, E. Olaiya, and C. H. Shepherd-Themistocleous, “Extra Higgs boson and Z' as portals to signatures of heavy neutrinos at the LHC,” *JHEP* **02** (2018) 109, [arXiv:1708.03650 \[hep-ph\]](#).
- [58] J. C. Helo, M. Hirsch, and Z. S. Wang, “Heavy neutral fermions at the high-luminosity LHC,” *JHEP* **07** (2018) 056, [arXiv:1803.02212 \[hep-ph\]](#).
- [59] S. Chakraborty, M. Mitra, and S. Shil, “Fat Jet Signature of a Heavy Neutrino at Lepton Collider,” *Phys. Rev. D* **100** no. 1, (2019) 015012, [arXiv:1810.08970 \[hep-ph\]](#).
- [60] G. Cottin, J. C. Helo, M. Hirsch, A. Titov, and Z. S. Wang, “Heavy neutral leptons in effective field theory and the high-luminosity LHC,” *JHEP* **09** (2021) 039, [arXiv:2105.13851 \[hep-ph\]](#).
- [61] A. M. Abdullahi *et al.*, “The present and future status of heavy neutral leptons,” *J. Phys. G* **50** no. 2, (2023) 020501, [arXiv:2203.08039 \[hep-ph\]](#).
- [62] B. Batell, T. Ghosh, T. Han, and K. Xie, “Heavy neutral leptons at the Electron-Ion Collider,” *JHEP* **03** (2023) 020, [arXiv:2210.09287 \[hep-ph\]](#).

- [63] J. C. Pati and A. Salam, “Lepton Number as the Fourth Color,” *Phys. Rev. D* **10** (1974) 275–289. [Erratum: *Phys.Rev.D* 11, 703–703 (1975)].
- [64] R. N. Mohapatra and J. C. Pati, “A Natural Left-Right Symmetry,” *Phys. Rev. D* **11** (1975) 2558.
- [65] G. Senjanovic and R. N. Mohapatra, “Exact left-right symmetry and spontaneous violation of parity,” *Phys. Rev. D* **12** (Sep, 1975) 1502–1505.
<https://link.aps.org/doi/10.1103/PhysRevD.12.1502>.
- [66] B. Holdom, “Two U(1)’s and Epsilon Charge Shifts,” *Phys. Lett. B* **166** (1986) 196–198.
- [67] P. Langacker, “The Physics of Heavy Z' Gauge Bosons,” *Rev. Mod. Phys.* **81** (2009) 1199–1228, [arXiv:0801.1345 \[hep-ph\]](#).
- [68] C. Boehm, P. Fayet, and J. Silk, “Light and heavy dark matter particles,” *Phys. Rev. D* **69** (2004) 101302, [arXiv:hep-ph/0311143](#).
- [69] M. Pospelov, A. Ritz, and M. B. Voloshin, “Secluded WIMP Dark Matter,” *Phys. Lett. B* **662** (2008) 53–61, [arXiv:0711.4866 \[hep-ph\]](#).
- [70] N. Arkani-Hamed, D. P. Finkbeiner, T. R. Slatyer, and N. Weiner, “A Theory of Dark Matter,” *Phys. Rev. D* **79** (2009) 015014, [arXiv:0810.0713 \[hep-ph\]](#).
- [71] M. R. Buckley and P. J. Fox, “Dark Matter Self-Interactions and Light Force Carriers,” *Phys. Rev. D* **81** (2010) 083522, [arXiv:0911.3898 \[hep-ph\]](#).
- [72] V. Silveira and A. Zee, “SCALAR PHANTOMS,” *Phys. Lett. B* **161** (1985) 136–140.
- [73] D. Curtin *et al.*, “Exotic decays of the 125 GeV Higgs boson,” *Phys. Rev. D* **90** no. 7, (2014) 075004, [arXiv:1312.4992 \[hep-ph\]](#).
- [74] N. Craig, A. Katz, M. Strassler, and R. Sundrum, “Naturalness in the Dark at the LHC,” *JHEP* **07** (2015) 105, [arXiv:1501.05310 \[hep-ph\]](#).
- [75] J. de Vries, H. K. Dreiner, and D. Schmeier, “R-Parity Violation and Light Neutralinos at SHiP and the LHC,” *Phys. Rev. D* **94** no. 3, (2016) 035006, [arXiv:1511.07436 \[hep-ph\]](#).
- [76] S. Banerjee, G. Bélanger, B. Bhattacharjee, F. Boudjema, R. M. Godbole, and S. Mukherjee, “Novel signature for long-lived particles at the LHC,” *Phys. Rev. D* **98** no. 11, (2018) 115026, [arXiv:1706.07407 \[hep-ph\]](#).
- [77] D. Dercks, H. K. Dreiner, M. Hirsch, and Z. S. Wang, “Long-Lived Fermions at AL3X,” *Phys. Rev. D* **99** no. 5, (2019) 055020, [arXiv:1811.01995 \[hep-ph\]](#).
- [78] B. Bhattacharjee, S. Mukherjee, and R. Sengupta, “Study of energy deposition patterns in hadron calorimeter for prompt and displaced jets using convolutional neural network,” *JHEP* **11** (2019) 156, [arXiv:1904.04811 \[hep-ph\]](#).
- [79] S. Banerjee, B. Bhattacharjee, A. Goudelis, B. Herrmann, D. Sengupta, and

- R. Sengupta, “Determining the lifetime of long-lived particles at the HL-LHC,” *Eur. Phys. J. C* **81** no. 2, (2021) 172, [arXiv:1912.06669 \[hep-ph\]](#).
- [80] J. De Vries, H. K. Dreiner, J. Y. Günther, Z. S. Wang, and G. Zhou, “Long-lived Sterile Neutrinos at the LHC in Effective Field Theory,” *JHEP* **03** (2021) 148, [arXiv:2010.07305 \[hep-ph\]](#).
- [81] B. Bhattacharjee, S. Mukherjee, R. Sengupta, and P. Solanki, “Triggering long-lived particles in HL-LHC and the challenges in the rst stage of the trigger system,” *JHEP* **08** (2020) 141, [arXiv:2003.03943 \[hep-ph\]](#).
- [82] B. Bhattacharjee, S. Matsumoto, and R. Sengupta, “Long-lived light mediators from Higgs boson decay at HL-LHC and FCC-hh, and a proposal of dedicated long-lived particle detectors for FCC-hh,” *Phys. Rev. D* **106** no. 9, (2022) 095018, [arXiv:2111.02437 \[hep-ph\]](#).
- [83] B. Bhattacharjee, T. Ghosh, R. Sengupta, and P. Solanki, “Dedicated triggers for displaced jets using timing information from electromagnetic calorimeter at HL-LHC,” *JHEP* **08** (2022) 254, [arXiv:2112.04518 \[hep-ph\]](#).
- [84] A. Adhikary, R. K. Barman, B. Bhattacharjee, A. De, R. M. Godbole, and S. Kulkarni, “Long-lived NLSP in the NMSSM,” *Phys. Rev. D* **108** no. 3, (2023) 035020, [arXiv:2207.00600 \[hep-ph\]](#).
- [85] M. Ovchinnikov, V. Kryshchal, and K. Bondarenko, “Sensitivity of the FACET experiment to Heavy Neutral Leptons and Dark Scalars,” *JHEP* **02** (2023) 056, [arXiv:2209.14870 \[hep-ph\]](#).
- [86] P. Bandyopadhyay, E. J. Chun, and C. Sen, “Boosted displaced decay of right-handed neutrinos at CMS, ATLAS and MATHUSLA,” *JHEP* **02** (2023) 103, [arXiv:2205.12511 \[hep-ph\]](#).
- [87] P. Bandyopadhyay, M. Frank, S. Parashar, and C. Sen, “Interplay of inert doublet and vector-like lepton triplet with displaced vertices at the LHC/FCC and MATHUSLA,” *JHEP* **03** (2024) 109, [arXiv:2310.08883 \[hep-ph\]](#).
- [88] B. Bhattacharjee, H. K. Dreiner, N. Ghosh, S. Matsumoto, R. Sengupta, and P. Solanki, “Light long-lived particles at the FCC-hh with the proposal for a dedicated forward detector FOREHUNT and a transverse detector DELIGHT,” *Phys. Rev. D* **110** no. 1, (2024) 015036, [arXiv:2306.11803 \[hep-ph\]](#).
- [89] B. Bhattacharjee, P. Konar, V. S. Ngairangbam, and P. Solanki, “LLPNet: Graph Autoencoder for Triggering Light Long-Lived Particles at HL-LHC,” [arXiv:2308.13611 \[hep-ph\]](#).
- [90] B. Bhattacharjee and P. Solanki, “Search for electroweakinos in R-parity violating SUSY with long-lived particles at HL-LHC,” *JHEP* **12** (2023) 148, [arXiv:2308.05804 \[hep-ph\]](#).
- [91] T. Bandyopadhyay, “Dark Photons from displaced vertices,” [arXiv:2311.16997 \[hep-ph\]](#).

- [92] J. Y. Günther, J. de Vries, H. K. Dreiner, Z. S. Wang, and G. Zhou, “Long-lived neutral fermions at the DUNE near detector,” *JHEP* **01** (2024) 108, [arXiv:2310.12392 \[hep-ph\]](#).
- [93] J. de Vries, H. K. Dreiner, J. Groot, J. Y. Günther, and Z. S. Wang, “Probing light sterile neutrinos in left-right symmetric models with displaced vertices and neutrinoless double beta decay,” [arXiv:2406.15091 \[hep-ph\]](#).
- [94] Z. S. Wang, “Constraining long-lived particles from Higgs boson decays at the LHC with displaced vertices and jets,” *Phys. Rev. D* **110** no. 5, (2024) 055033, [arXiv:2406.16281 \[hep-ph\]](#).
- [95] **ATLAS** Collaboration, G. Aad *et al.*, “Search for long-lived, weakly interacting particles that decay to displaced hadronic jets in proton-proton collisions at $\sqrt{s} = 8$ TeV with the ATLAS detector,” *Phys. Rev. D* **92** no. 1, (2015) 012010, [arXiv:1504.03634 \[hep-ex\]](#).
- [96] **ATLAS** Collaboration, M. Aaboud *et al.*, “Search for long-lived particles in final states with displaced dimuon vertices in pp collisions at $\sqrt{s} = 13$ TeV with the ATLAS detector,” *Phys. Rev. D* **99** no. 1, (2019) 012001, [arXiv:1808.03057 \[hep-ex\]](#).
- [97] **ATLAS** Collaboration, M. Aaboud *et al.*, “Search for the Production of a Long-Lived Neutral Particle Decaying within the ATLAS Hadronic Calorimeter in Association with a Z Boson from pp Collisions at $\sqrt{s} = 13$ TeV,” *Phys. Rev. Lett.* **122** no. 15, (2019) 151801, [arXiv:1811.02542 \[hep-ex\]](#).
- [98] **ATLAS** Collaboration, M. Aaboud *et al.*, “Search for long-lived particles produced in pp collisions at $\sqrt{s} = 13$ TeV that decay into displaced hadronic jets in the ATLAS muon spectrometer,” *Phys. Rev. D* **99** no. 5, (2019) 052005, [arXiv:1811.07370 \[hep-ex\]](#).
- [99] **ATLAS** Collaboration, G. Aad *et al.*, “Search for displaced vertices of oppositely charged leptons from decays of long-lived particles in pp collisions at $\sqrt{s} = 13$ TeV with the ATLAS detector,” *Phys. Lett. B* **801** (2020) 135114, [arXiv:1907.10037 \[hep-ex\]](#).
- [100] **ATLAS** Collaboration, G. Aad *et al.*, “Search for light long-lived neutral particles produced in pp collisions at $\sqrt{s} = 13$ TeV and decaying into collimated leptons or light hadrons with the ATLAS detector,” *Eur. Phys. J. C* **80** no. 5, (2020) 450, [arXiv:1909.01246 \[hep-ex\]](#).
- [101] **ATLAS** Collaboration, G. Aad *et al.*, “Search for long-lived neutral particles produced in pp collisions at $\sqrt{s} = 13$ TeV decaying into displaced hadronic jets in the ATLAS inner detector and muon spectrometer,” *Phys. Rev. D* **101** no. 5, (2020) 052013, [arXiv:1911.12575 \[hep-ex\]](#).
- [102] **ATLAS Collaboration** Collaboration, “Search prospects for dark-photons decaying to displaced collimated jets of muons at HL-LHC,” tech. rep., CERN, Geneva, Jan, 2019. <https://cds.cern.ch/record/2654518>.

- [103] **ATLAS Collaboration**, G. Aad *et al.*, “Search for long-lived, massive particles in events with a displaced vertex and a muon with large impact parameter in pp collisions at $\sqrt{s} = 13$ TeV with the ATLAS detector,” *Phys. Rev. D* **102** no. 3, (2020) 032006, [arXiv:2003.11956 \[hep-ex\]](#).
- [104] **ATLAS Collaboration**, “Search for events with a pair of displaced vertices from long-lived neutral particles decaying into hadronic jets in the ATLAS muon spectrometer in pp collisions at $\sqrt{s} = 13$ TeV,” tech. rep., CERN, Geneva, Jul, 2021. <http://cds.cern.ch/record/2777238>.
- [105] **ATLAS Collaboration**, G. Aad *et al.*, “Search for exotic decays of the Higgs boson into long-lived particles in pp collisions at $\sqrt{s} = 13$ TeV using displaced vertices in the ATLAS inner detector,” [arXiv:2107.06092 \[hep-ex\]](#).
- [106] **CMS Collaboration**, V. Khachatryan *et al.*, “Search for long-lived particles that decay into final states containing two electrons or two muons in proton-proton collisions at $\sqrt{s} = 8$ TeV,” *Phys. Rev. D* **91** no. 5, (2015) 052012, [arXiv:1411.6977 \[hep-ex\]](#).
- [107] **CMS Collaboration**, A. M. Sirunyan *et al.*, “Search for decays of stopped exotic long-lived particles produced in proton-proton collisions at $\sqrt{s} = 13$ TeV,” *JHEP* **05** (2018) 127, [arXiv:1801.00359 \[hep-ex\]](#).
- [108] **CMS Collaboration**, A. M. Sirunyan *et al.*, “Search for new particles decaying to a jet and an emerging jet,” *JHEP* **02** (2019) 179, [arXiv:1810.10069 \[hep-ex\]](#).
- [109] **CMS Collaboration**, “Search sensitivity for dark photons decaying to displaced muons with CMS at the high-luminosity LHC,” tech. rep., CERN, Geneva, 2018. <http://cds.cern.ch/record/2644533>.
- [110] **CMS Collaboration**, A. M. Sirunyan *et al.*, “Search for long-lived particles using delayed photons in proton-proton collisions at $\sqrt{s} = 13$ TeV,” *Phys. Rev. D* **100** no. 11, (2019) 112003, [arXiv:1909.06166 \[hep-ex\]](#).
- [111] **CMS Collaboration**, A. M. Sirunyan *et al.*, “Search for disappearing tracks in proton-proton collisions at $\sqrt{s} = 13$ TeV,” *Phys. Lett. B* **806** (2020) 135502, [arXiv:2004.05153 \[hep-ex\]](#).
- [112] **CMS Collaboration**, “Search for long-lived particles decaying into displaced jets,” tech. rep., CERN, Geneva, 2020. <https://cds.cern.ch/record/2717071>.
- [113] **CMS Collaboration**, A. Tumasyan *et al.*, “Search for long-lived particles decaying in the CMS endcap muon detectors in proton-proton collisions at $\sqrt{s} = 13$ TeV,” [arXiv:2107.04838 \[hep-ex\]](#).
- [114] **CMS Collaboration**, A. Tumasyan *et al.*, “Search for long-lived particles decaying to leptons with large impact parameter in proton-proton collisions at $\sqrt{s} = 13$ TeV,” *Eur. Phys. J. C* **82** no. 2, (2022) 153, [arXiv:2110.04809 \[hep-ex\]](#).

- [115] **CMS** Collaboration, A. Tumasyan *et al.*, “Search for long-lived particles produced in association with a Z boson in proton-proton collisions at $\sqrt{s} = 13$ TeV,” *JHEP* **03** (2022) 160, [arXiv:2110.13218 \[hep-ex\]](#).
- [116] **LHCb** Collaboration, R. Aaij *et al.*, “Search for Higgs-like bosons decaying into long-lived exotic particles,” *Eur. Phys. J. C* **76** no. 12, (2016) 664, [arXiv:1609.03124 \[hep-ex\]](#).
- [117] **LHCb** Collaboration, R. Aaij *et al.*, “Search for massive long-lived particles decaying semileptonically in the LHCb detector,” *Eur. Phys. J. C* **77** no. 4, (2017) 224, [arXiv:1612.00945 \[hep-ex\]](#).
- [118] **LHCb** Collaboration, R. Aaij *et al.*, “Search for long-lived scalar particles in $B^+ \rightarrow K^+ \chi(\mu^+ \mu^-)$ decays,” *Phys. Rev. D* **95** no. 7, (2017) 071101, [arXiv:1612.07818 \[hep-ex\]](#).
- [119] **LHCb** Collaboration, R. Aaij *et al.*, “Updated search for long-lived particles decaying to jet pairs,” *Eur. Phys. J. C* **77** no. 12, (2017) 812, [arXiv:1705.07332 \[hep-ex\]](#).
- [120] **LHCb** Collaboration, R. Aaij *et al.*, “Search for $A' \rightarrow \mu^+ \mu^-$ Decays,” *Phys. Rev. Lett.* **124** no. 4, (2020) 041801, [arXiv:1910.06926 \[hep-ex\]](#).
- [121] **LHCb** Collaboration, R. Aaij *et al.*, “Search for long-lived particles decaying to $e^\pm \mu^\mp \nu$,” *Eur. Phys. J. C* **81** no. 3, (2021) 261, [arXiv:2012.02696 \[hep-ex\]](#).
- [122] **E949** Collaboration, A. V. Artamonov *et al.*, “New measurement of the $K^+ \rightarrow \pi^+ \nu \bar{\nu}$ branching ratio,” *Phys. Rev. Lett.* **101** (2008) 191802, [arXiv:0808.2459 \[hep-ex\]](#).
- [123] **BNL-E949** Collaboration, A. V. Artamonov *et al.*, “Study of the decay $K^+ \rightarrow \pi^+ \nu \bar{\nu}$ in the momentum region $140 < P_\pi < 199$ MeV/c,” *Phys. Rev. D* **79** (2009) 092004, [arXiv:0903.0030 \[hep-ex\]](#).
- [124] **NA62** Collaboration, E. Cortina Gil *et al.*, “Search for π^0 decays to invisible particles,” *JHEP* **02** (2021) 201, [arXiv:2010.07644 \[hep-ex\]](#).
- [125] **NA62** Collaboration, E. Cortina Gil *et al.*, “Search for a feebly interacting particle X in the decay $K^+ \rightarrow \pi^+ X$,” *JHEP* **03** (2021) 058, [arXiv:2011.11329 \[hep-ex\]](#).
- [126] **NA62** Collaboration, E. Cortina Gil *et al.*, “Measurement of the very rare $K^+ \rightarrow \pi^+ \nu \bar{\nu}$ decay,” *JHEP* **06** (2021) 093, [arXiv:2103.15389 \[hep-ex\]](#).
- [127] D. Gorbunov, I. Krasnov, and S. Suvarov, “Constraints on light scalars from PS191 results,” *Phys. Lett. B* **820** (2021) 136524, [arXiv:2105.11102 \[hep-ph\]](#).
- [128] **CHARM** Collaboration, F. Bergsma *et al.*, “Search for Axion Like Particle Production in 400-GeV Proton - Copper Interactions,” *Phys. Lett. B* **157** (1985) 458–462.
- [129] D. Egana-Ugrinovic, S. Homiller, and P. Meade, “Light Scalars and the Koto Anomaly,” *Phys. Rev. Lett.* **124** no. 19, (2020) 191801, [arXiv:1911.10203 \[hep-ph\]](#).

- [130] J. L. Feng *et al.*, “The Forward Physics Facility at the High-Luminosity LHC,” *J. Phys. G* **50** no. 3, (2023) 030501, [arXiv:2203.05090 \[hep-ex\]](#).
- [131] S. Cerci *et al.*, “FACET: A new long-lived particle detector in the very forward region of the CMS experiment,” *JHEP* **06** (2022) 110, [arXiv:2201.00019 \[hep-ex\]](#).
- [132] **MoEDAL-MAPP** Collaboration, B. Acharya *et al.*, “MoEDAL-MAPP, an LHC Dedicated Detector Search Facility,” in *Snowmass 2021*. 9, 2022. [arXiv:2209.03988 \[hep-ph\]](#).
- [133] D. Curtin *et al.*, “Long-Lived Particles at the Energy Frontier: The MATHUSLA Physics Case,” *Rept. Prog. Phys.* **82** no. 11, (2019) 116201, [arXiv:1806.07396 \[hep-ph\]](#).
- [134] **MATHUSLA** Collaboration, H. Lubatti *et al.*, “Explore the lifetime frontier with MATHUSLA,” *JINST* **15** no. 06, (2020) C06026, [arXiv:1901.04040 \[hep-ex\]](#).
- [135] D. Curtin and J. S. Grewal, “Long Lived Particle Decays in MATHUSLA,” [arXiv:2308.05860 \[hep-ph\]](#).
- [136] G. Aielli *et al.*, “Expression of interest for the CODEX-b detector,” *Eur. Phys. J. C* **80** no. 12, (2020) 1177, [arXiv:1911.00481 \[hep-ex\]](#).
- [137] M. Bauer, O. Brandt, L. Lee, and C. Ohm, “ANUBIS: Proposal to search for long-lived neutral particles in CERN service shafts,” [arXiv:1909.13022 \[physics.ins-det\]](#).
- [138] **FASER** Collaboration, H. Abreu *et al.*, “Search for dark photons with the FASER detector at the LHC,” *Phys. Lett. B* **848** (2024) 138378, [arXiv:2308.05587 \[hep-ex\]](#).
- [139] Z. S. Wang and K. Wang, “Physics with far detectors at future lepton colliders,” *Phys. Rev. D* **101** no. 7, (2020) 075046, [arXiv:1911.06576 \[hep-ph\]](#).
- [140] M. Chrzaskaszcz, M. Drewes, and J. Hajer, “HECATE: A long-lived particle detector concept for the FCC-ee or CEPC,” *Eur. Phys. J. C* **81** no. 6, (2021) 546, [arXiv:2011.01005 \[hep-ph\]](#).
- [141] R. Schäfer, F. Tillinger, and S. Westhoff, “Near or far detectors? A case study for long-lived particle searches at electron-positron colliders,” *Phys. Rev. D* **107** no. 7, (2023) 076022, [arXiv:2202.11714 \[hep-ph\]](#).
- [142] A. Boyarsky, O. Mikulenko, M. Ovchinnikov, and L. Shchutska, “Exploring the potential of FCC-hh to search for particles from B mesons,” *JHEP* **01** (2023) 042, [arXiv:2204.01622 \[hep-ph\]](#).
- [143] R. Mammen Abraham, J. Adhikary, J. L. Feng, M. Fieg, F. Kling, J. Li, J. Pei, T. R. Rabemananjara, J. Rojo, and S. Trojanowski, “FPF@FCC: Neutrino, QCD, and BSM Physics Opportunities with Far-Forward Experiments at a 100 TeV Proton Collider,” [arXiv:2409.02163 \[hep-ph\]](#).

- [144] Y. Lu, Y.-n. Mao, K. Wang, and Z. S. Wang, “LAYCAST: LAYered CAvern Surface Tracker at future electron-positron colliders,” [arXiv:2406.05770 \[hep-ph\]](#).
- [145] **ILC** Collaboration, “The International Linear Collider Technical Design Report - Volume 2: Physics,” [arXiv:1306.6352 \[hep-ph\]](#).
- [146] H. Abramowicz *et al.*, “The International Linear Collider Technical Design Report - Volume 4: Detectors,” [arXiv:1306.6329 \[physics.ins-det\]](#).
- [147] **CEPC Study Group** Collaboration, “CEPC Conceptual Design Report: Volume 1 - Accelerator,” [arXiv:1809.00285 \[physics.acc-ph\]](#).
- [148] **CEPC Study Group** Collaboration, M. Dong *et al.*, “CEPC Conceptual Design Report: Volume 2 - Physics & Detector,” [arXiv:1811.10545 \[hep-ex\]](#).
- [149] **CEPC Study Group** Collaboration, W. Abdallah *et al.*, “CEPC Technical Design Report: Accelerator,” *Radiat. Detect. Technol. Methods* **8** no. 1, (2024) 1–1105, [arXiv:2312.14363 \[physics.acc-ph\]](#).
- [150] **CLIC** Collaboration, J. de Blas *et al.*, “The CLIC Potential for New Physics,” [arXiv:1812.02093 \[hep-ph\]](#).
- [151] **CLICdp**, **CLIC** Collaboration, T. K. Charles *et al.*, “The Compact Linear Collider (CLIC) - 2018 Summary Report,” [arXiv:1812.06018 \[physics.acc-ph\]](#).
- [152] **CLIC**, **CLICdp** Collaboration, “The Compact Linear e^+e^- Collider (CLIC): Physics Potential,” [arXiv:1812.07986 \[hep-ex\]](#).
- [153] **FCC** Collaboration, A. Abada *et al.*, “FCC Physics Opportunities: Future Circular Collider Conceptual Design Report Volume 1,” *Eur. Phys. J. C* **79** no. 6, (2019) 474.
- [154] **FCC** Collaboration, A. Abada *et al.*, “FCC-ee: The Lepton Collider: Future Circular Collider Conceptual Design Report Volume 2,” *Eur. Phys. J. ST* **228** no. 2, (2019) 261–623.
- [155] **FCC** Collaboration, A. Abada *et al.*, “FCC-hh: The Hadron Collider: Future Circular Collider Conceptual Design Report Volume 3,” *Eur. Phys. J. ST* **228** no. 4, (2019) 755–1107.
- [156] S. Matsumoto, Y.-L. S. Tsai, and P.-Y. Tseng, “Light Fermionic WIMP Dark Matter with Light Scalar Mediator,” *JHEP* **07** (2019) 050, [arXiv:1811.03292 \[hep-ph\]](#).
- [157] M. W. Winkler, “Decay and detection of a light scalar boson mixing with the Higgs boson,” *Phys. Rev. D* **99** no. 1, (2019) 015018, [arXiv:1809.01876 \[hep-ph\]](#).
- [158] J. L. Feng, I. Galon, F. Kling, and S. Trojanowski, “Dark Higgs bosons at the ForwArd Search ExpeRiment,” *Phys. Rev. D* **97** no. 5, (2018) 055034, [arXiv:1710.09387 \[hep-ph\]](#).
- [159] M. J. Dolan, F. Kahlhoefer, C. McCabe, and K. Schmidt-Hoberg, “A taste of dark

- matter: Flavour constraints on pseudoscalar mediators,” *JHEP* **03** (2015) 171, [arXiv:1412.5174 \[hep-ph\]](#). [Erratum: *JHEP* 07, 103 (2015)].
- [160] **FASER** Collaboration, A. Ariga *et al.*, “FASER’s physics reach for long-lived particles,” *Phys. Rev. D* **99** no. 9, (2019) 095011, [arXiv:1811.12522 \[hep-ph\]](#).
 - [161] T. Ferber, A. Grohsjean, and F. Kahlhoefer, “Dark Higgs bosons at colliders,” *Prog. Part. Nucl. Phys.* **136** (2024) 104105, [arXiv:2305.16169 \[hep-ph\]](#).
 - [162] A. Djouadi, J. Kalinowski, and M. Spira, “HDECAY: A Program for Higgs boson decays in the standard model and its supersymmetric extension,” *Comput. Phys. Commun.* **108** (1998) 56–74, [arXiv:hep-ph/9704448](#).
 - [163] **HDECAY** Collaboration, A. Djouadi, J. Kalinowski, M. Muehlleitner, and M. Spira, “HDECAY: Twenty₊₊ years after,” *Comput. Phys. Commun.* **238** (2019) 214–231, [arXiv:1801.09506 \[hep-ph\]](#).
 - [164] R. S. Chivukula and A. V. Manohar, “LIMITS ON A LIGHT HIGGS BOSON,” *Phys. Lett. B* **207** (1988) 86. [Erratum: *Phys.Lett.B* 217, 568 (1989)].
 - [165] **ATLAS** Collaboration, “Combination of searches for invisible Higgs boson decays with the ATLAS experiment,” tech. rep., CERN, Geneva, 2020. <https://cds.cern.ch/record/2743055>. All figures including auxiliary figures are available at <https://atlas.web.cern.ch/Atlas/GROUPS/PHYSICS/CONFNOTES/ATLAS-CONF-2020-052>.
 - [166] B. Batell, N. Blinov, C. Hearty, and R. McGehee, “Exploring Dark Sector Portals with High Intensity Experiments,” in *Snowmass 2021*. 7, 2022. [arXiv:2207.06905 \[hep-ph\]](#).
 - [167] G. Marocco and S. Sarkar, “Blast from the past: Constraints on the dark sector from the BEBC WA66 beam dump experiment,” *SciPost Phys.* **10** no. 2, (2021) 043, [arXiv:2011.08153 \[hep-ph\]](#).
 - [168] R. Barouki, G. Marocco, and S. Sarkar, “Blast from the past II: Constraints on heavy neutral leptons from the BEBC WA66 beam dump experiment,” *SciPost Phys.* **13** (2022) 118, [arXiv:2208.00416 \[hep-ph\]](#).
 - [169] S. Alekhin *et al.*, “A facility to Search for Hidden Particles at the CERN SPS: the SHiP physics case,” *Rept. Prog. Phys.* **79** no. 12, (2016) 124201, [arXiv:1504.04855 \[hep-ph\]](#).
 - [170] **SHiP** Collaboration, M. Anelli *et al.*, “A facility to Search for Hidden Particles (SHiP) at the CERN SPS,” [arXiv:1504.04956 \[physics.ins-det\]](#).
 - [171] **LSND** Collaboration, C. Athanassopoulos *et al.*, “Evidence for muon-neutrino \rightarrow electron-neutrino oscillations from pion decay in flight neutrinos,” *Phys. Rev. C* **58** (1998) 2489–2511, [arXiv:nuc1-ex/9706006](#).
 - [172] **LSND** Collaboration, A. Aguilar *et al.*, “Evidence for neutrino oscillations from

- the observation of $\bar{\nu}_e$ appearance in a $\bar{\nu}_\mu$ beam,” *Phys. Rev. D* **64** (2001) 112007, [arXiv:hep-ex/0104049](#).
- [173] S. Foroughi-Abari and A. Ritz, “LSND Constraints on the Higgs Portal,” *Phys. Rev. D* **102** no. 3, (2020) 035015, [arXiv:2004.14515 \[hep-ph\]](#).
 - [174] **MicroBooNE** Collaboration, P. Abratenko *et al.*, “Search for a Higgs Portal Scalar Decaying to Electron-Positron Pairs in the MicroBooNE Detector,” *Phys. Rev. Lett.* **127** no. 15, (2021) 151803, [arXiv:2106.00568 \[hep-ex\]](#).
 - [175] J. M. Berryman, A. de Gouvea, P. J. Fox, B. J. Kayser, K. J. Kelly, and J. L. Raaf, “Searches for Decays of New Particles in the DUNE Multi-Purpose Near Detector,” *JHEP* **02** (2020) 174, [arXiv:1912.07622 \[hep-ph\]](#).
 - [176] **L3** Collaboration, M. Acciarri *et al.*, “Search for neutral Higgs boson production through the process $e^+e^- \rightarrow Z^*H_0$,” *Phys. Lett. B* **385** (1996) 454–470.
 - [177] **LHCb** Collaboration, R. Aaij *et al.*, “Search for hidden-sector bosons in $B^0 \rightarrow K^{*0}\mu^+\mu^-$ decays,” *Phys. Rev. Lett.* **115** no. 16, (2015) 161802, [arXiv:1508.04094 \[hep-ex\]](#).
 - [178] J. A. Evans, A. Gandrakota, S. Knapen, and H. Routray, “Searching for exotic B -meson decays enabled by the CMS L1 track trigger,” *Phys. Rev. D* **103** no. 1, (2021) 015026, [arXiv:2008.06918 \[hep-ph\]](#).
 - [179] **BaBar** Collaboration, J. P. Lees *et al.*, “Search for Long-Lived Particles in e^+e^- Collisions,” *Phys. Rev. Lett.* **114** no. 17, (2015) 171801, [arXiv:1502.02580 \[hep-ex\]](#).
 - [180] **Belle-II** Collaboration, I. Adachi *et al.*, “Search for a long-lived spin-0 mediator in $b \rightarrow s$ transitions at the Belle II experiment,” *Phys. Rev. D* **108** no. 11, (2023) L111104, [arXiv:2306.02830 \[hep-ex\]](#).
 - [181] A. Kachanovich, U. Nierste, and I. Nišandžić, “Higgs portal to dark matter and $B \rightarrow K^{(*)}$ decays,” *Eur. Phys. J. C* **80** no. 7, (2020) 669, [arXiv:2003.01788 \[hep-ph\]](#).
 - [182] V. V. Gligorov, S. Knapen, M. Papucci, and D. J. Robinson, “Searching for Long-lived Particles: A Compact Detector for Exotics at LHCb,” *Phys. Rev. D* **97** no. 1, (2018) 015023, [arXiv:1708.09395 \[hep-ph\]](#).
 - [183] D. Craik, P. Ilten, D. Johnson, and M. Williams, “LHCb future dark-sector sensitivity projections for Snowmass 2021,” in *Snowmass 2021*, 3, 2022. [arXiv:2203.07048 \[hep-ph\]](#).
 - [184] **ATLAS** Collaboration, “Long-lived particle summary plots for Hidden Sector and Dark Photon models,”.
 - [185] **CMS** Collaboration, “CMS Exotica Summary plots for 13 TeV data.”. [Higgs decays to long-lived particles](#).
 - [186] **CMS** Collaboration, A. Tumasyan *et al.*, “Search for long-lived particles decaying into muon pairs in proton-proton collisions at $\sqrt{s} = 13$ TeV collected with a

- dedicated high-rate data stream,” *JHEP* **04** (2022) 062, [arXiv:2112.13769 \[hep-ex\]](#).
- [187] **CMS** Collaboration, A. Hayrapetyan *et al.*, “Search for long-lived particles decaying to final states with a pair of muons in proton-proton collisions at $\sqrt{s} = 13.6$ TeV,” [arXiv:2402.14491 \[hep-ex\]](#).
 - [188] **CMS** Collaboration, A. M. Sirunyan *et al.*, “Search for long-lived particles using displaced jets in proton-proton collisions at $\sqrt{s} = 13$ TeV,” *Phys. Rev. D* **104** no. 1, (2021) 012015, [arXiv:2012.01581 \[hep-ex\]](#).
 - [189] **CMS** Collaboration, A. Hayrapetyan *et al.*, “Search for long-lived particles decaying in the CMS muon detectors in proton-proton collisions at $\sqrt{s} = 13$ TeV,” [arXiv:2402.01898 \[hep-ex\]](#).
 - [190] “Fcc-ee physics performance.” <https://hep-fcc.github.io/FCCeePhysicsPerformance/#lumi>.
 - [191] G. Bernardi *et al.*, “The Future Circular Collider: a Summary for the US 2021 Snowmass Process,” [arXiv:2203.06520 \[hep-ex\]](#).
 - [192] G. Bencivenni *et al.*, “The μ -RWELL detector,” *JINST* **12** no. 06, (2017) C06027.
 - [193] M. Dam, “FCC-ee Detector Designs,” *FCC-ee Study Group, Physics at FCC, CERN* (2019) . <https://indico.cern.ch/event/789349/contributions/3298691/attachments/1805339/2946724/FCCCDR4March-MD.pdf>.
 - [194] F. Bedeschi, “Overview of the IDEA detector,” *3rd FCC Physics and Experiments Workshop* (2020) . https://indico.cern.ch/event/838435/contributions/3658345/attachments/1968063/3273039/Bedeschi_IDEA.pdf.
 - [195] E. Fontanesi *et al.*, “Delphes Fast simulation status for the IDEA detector,” in *11th FCC-ee workshop*. 2019. https://indico.cern.ch/event/766859/contributions/3253194/attachments/1776387/2889068/Delphes_Fast_simulation_status_for_the_IDEA_detector_EF.pdf.
 - [196] N. Akchurin *et al.*, “Particle identification in the longitudinally unsegmented RD52 calorimeter,” *Nucl. Instrum. Meth. A* **735** (2014) 120–129.
 - [197] G. Bencivenni, R. D. Oliveira, G. Felici, M. Gatta, M. Giovannetti, G. Morello, and M. P. Lener, “The μ -rwell for high rate application,” *Journal of Instrumentation* **15** no. 09, (Sep, 2020) C09034. <https://dx.doi.org/10.1088/1748-0221/15/09/C09034>.
 - [198] **DELPHES 3** Collaboration, J. de Favereau, C. Delaere, P. Demin, A. Giammanco, V. Lemaître, A. Mertens, and M. Selvaggi, “DELPHES 3, A modular framework for fast simulation of a generic collider experiment,” *JHEP* **02** (2014) 057, [arXiv:1307.6346 \[hep-ex\]](#).
 - [199] T. Sjöstrand, S. Ask, J. R. Christiansen, R. Corke, N. Desai, P. Ilten, S. Mrenna, S. Prestel, C. O. Rasmussen, and P. Z. Skands, “An introduction to PYTHIA 8.2,” *Comput. Phys. Commun.* **191** (2015) 159–177, [arXiv:1410.3012 \[hep-ph\]](#).

- [200] C. Bierlich *et al.*, “A comprehensive guide to the physics and usage of PYTHIA 8.3,” *SciPost Phys. Codeb.* **2022** (2022) 8, [arXiv:2203.11601 \[hep-ph\]](#).
- [201] J. Alwall, R. Frederix, S. Frixione, V. Hirschi, F. Maltoni, O. Mattelaer, H. S. Shao, T. Stelzer, P. Torrielli, and M. Zaro, “The automated computation of tree-level and next-to-leading order differential cross sections, and their matching to parton shower simulations,” *JHEP* **07** (2014) 079, [arXiv:1405.0301 \[hep-ph\]](#).
- [202] G. Ripellino, M. V. Voorde, A. Gallén, and R. Gonzalez Suarez, “Searching for long-lived dark scalars at the FCC-ee,” [arXiv:2412.10141 \[hep-ex\]](#).